Aalborg University

Department of energy technology

Student master thesis project

# DFIG Fault Ride Through Control

*Authors:*
Cătălin Gavriluţă
Sergiu Spătaru

*Supervisors:*
Flemming Abrahamsen
Zhe Chen

May 30, 2011

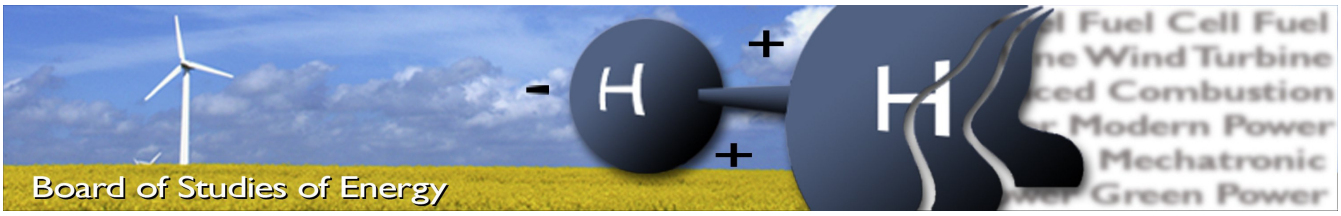


| | |
|---|---|
| **Title:** | DFIG Fault Ride Through Control |
| **Semester:** | 10th Semester |
| **Semester theme:** | Master thesis |
| **Project period:** | 01.02.11 to 31.05.11 |
| **ECTS:** | 30 |
| **Supervisor:** | Zhe Chen |
| | Flemming Abrahamsen |
| **Project group:** | WPS 1054 |

Cătălin GAVRILUŢĂ

Sergiu SPĂTARU

**SYNOPSIS:**

The DFIG based WT industry has been seriously challenged lately by more and more exigent grid codes. In order to fulfill the increasingly stringent requirements without reducing the economic advantage of the DFIG systems, new FRT control strategies are being researched.

Two methods for improving the FRT capability of DFIG based WT employing vector oriented control in synchronous reference frame are proposed and implemented. Further on, the new control strategies are tested on systems presenting DC-Chopper and rotor or stator crowbar as protection devices. Simulation results for a 2MW system riding through medium and low symmetrical voltage drops are presented and analyzed in conjunction with the latest Danish grid code fault ride through requirements.

The two methods show complementary results. The first one provides satisfactory results in terms of reactive current support, while the second one improves the transient response of the system, minimizing the inflicted electrical and mechanical stress.

A 7.5kW laboratory scaled setup was built in order to provide an experimental framework for implementing some of the proposed control strategies.

| | |
|---|---|
| Copies: | 3 |
| Pages, total: | 92 |
| Appendix: | 43 |
| Supplements: | 1 attached CD |

**By signing this document, each member of the group confirms that all participated in the project work and thereby all members are collectively liable for the content of the report.**

## Preface

This report represents the documentation of the master thesis entitled "DFIG Fault Ride Through Control". The project was prepared between the 1st of February 2011 and the 31st of May 2011, at Aalborg University, Institute of Energy Technology, by the WPS semester group 1054.

The project was conducted in collaboration with *kk-electronic*, one of the leading Danish companies providing control systems for windmills and alternative energy sources.

Simulations scenarios using Matlab-Simulink and experiments on a laboratory scaled system have been performed.

The literature references are shown in square brackets by numbers. The list of the references is presented in the chapter Bibliography. The Appendix is presented at the end of the report.

Figures and tables are numbered in the following format: Figure Chapter.Number and Table Chapter.Number.

The group would like to thank the supervisors, Zhe Chen and Flemming Abrahamsen, for the constructive feedback and help during the entire period of the project.

All the Simulink models and Matlab scripts used in this project can be found on the enclosed CD.

31st of May 2011

# Contents

# Chapter 1

# Introduction

The importance of wind power in the energy production map has evolved in the last twenty years from an optimistic idea to a fast emerging reality. Two hundred GW of harvesting capacity installed world wide [4] and turbines that increased in power by a factor of 100 over the last two decades [2] are valid proof that wind power is on an ascending trend that no other source of renewable energy has seen before.

According to a survey [2] conducted by the European Wind Energy Association (EWEA), among wind turbines over 1 MW rating, out of 52 distinct models of 20 different manufacturers, only three were fixed speed, 12 had two speed systems and 37 employed variable speed. The same survey points out the system based on doubly fed induction generator (DFIG) as being the most popular variable speed system. The main advantage of the DFIG is that only about 20-30% of the generator rated power has to pass through the power electronics equipment, which decreases the overall price of the unit [1].

Until recently, the economical advantages of DFIG based wind turbines (WT) were undoubted, but the DFIG technology has been challenged in the past years by more stringent grid codes (Figure 1.1). The "fault ride-through" (FRT) requirement in particular led to modifications of the initial system and to an increased capital cost. According to EWEA, from the top leading manufacturers of large scale wind turbines, Gamesa, Acciona and Nordex were still producing DFIG based WT in 2007, while GE Energy decided to change their 2.5 MW series, which entered mass production in the summer of 2008, from a DFIG to a permanent magnet with full scale converter system.

Whether the future of the DFIG is sealed by the new network requirements is yet to be decided. Until then a lot of effort is going on exploring new control algorithms, protection devices and strategies that will enable the DFIG to ride through the most serious faults.

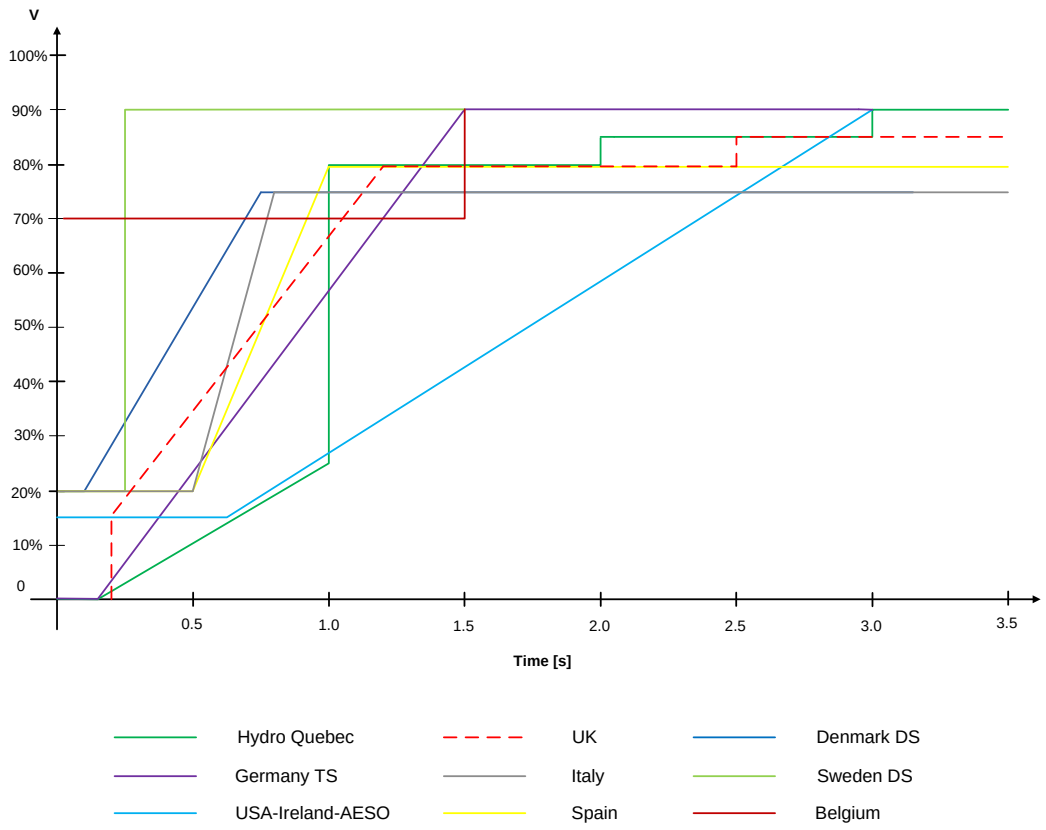


Figure 1.1: Low voltage ride through requirements for different countries [10].

## 1.1 Problem description

As previously mentioned, the presence of wind power in the energy market is starting to become more popular - with pioneer countries like Denmark, where the level of wind power penetration exceeded 20% in 2007. On a bigger picture, according to Figure 1.2, more than 10% of the European energy was provided by wind in 2010 with previsions of this value reaching 20% by 2020. Under these circumstances wind harvesting facilities have to start to employ the same functionality as the conventional power plants in terms of reliability and stability [8].

In order to ensure the smooth integration of renewable sources of energy into the electrical grid, the transmission system operators (TSOs) have to enforce new standards and regulations so that the stability of the overall system is ensured. These regulations, also known as grid codes, impose requirements regarding reliability, quality, stability and others, for any type of power source that has to be integrated into the network.

In countries like Denmark, Germany and Spain where wind energy is starting to account for a respectable percent of the overall energy production, the grid codes for wind production units have become more stringent over the past years. The requirements regarding fault ride through capability and grid support during fault

are becoming more exigent and seriously confront the DFIG systems.

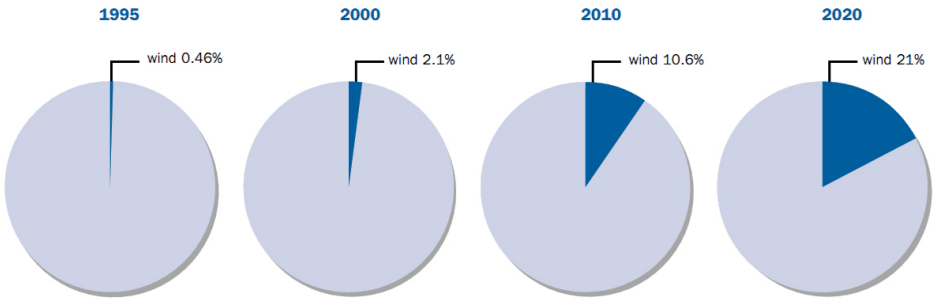


| | 1995 | 2000 | 2010 | 2020 |
|---|---|---|---|---|
| Total Generation Capacity (GW) | 538.8 | 580.7 | 706 | 855.4 |
| Total Wind Generation Capacity (GW) | 2.5 | 12.3 | 75 | 180 |
| Share of Wind (%) | 0.46% | 2.1% | 10.6% | 21% |

Figure 1.2: Contribution of Wind Power (GW) to EU Electricity Generation Capacity 1995 2020 (%) [3]

The Danish grid codes issued by Energinet.dk in September 2010 and applicable from December 2010 require a wind turbine to be able to sustain voltage drops down to 20% in the point of connection over a period of minimum 0.5 sec (line-to-line voltages for the 50 Hz component) without disconnecting as it can be seen in Figure 1.3(a). Three distinct areas can be noticed in the voltage drop characteristic, each of them representing different requirements that must be complied within the event of symmetrical as well as asymmetrical faults; this means that these requirements must be followed in the case of faults in one, two or all three phases of the electrical network.

- Area A: The wind power plant (WPP) must stay connected to the network and uphold normal production.
- Area B: The wind power plant must stay connected to the network. In addition to this, the wind power plant must provide maximum voltage support by supplying a controlled amount of reactive power so as to ensure that the wind power plant helps in stabilizing the voltage, see Figure 1.3(b).
- Area C: Disconnecting the wind power plant is allowed. During operation in area B, the supply of reactive power has first priority, while the supply of active power comes in second. The control strategy must follow Figure 1.3(b). so that the reactive power follows the control characteristic with a tolerance of 20% after 100 ms.

The cause of all problems regarding DFIG and fault ride through operation is related to the fact that, as it can be seen in Figure 1.4, the basic topology of a DFIG based WT has the stator directly connected to the grid, and the power electronics that equip the rotor are rated at only 30% of the turbine rating. Having the stator

directly connected to the grid results in the fact that if the network experiences a voltage drop, the stator voltage will change suddenly, and if this change is not immediately compensated by the rotor voltage, a disturbance current is driven through both stator and rotor windings [6, 25].

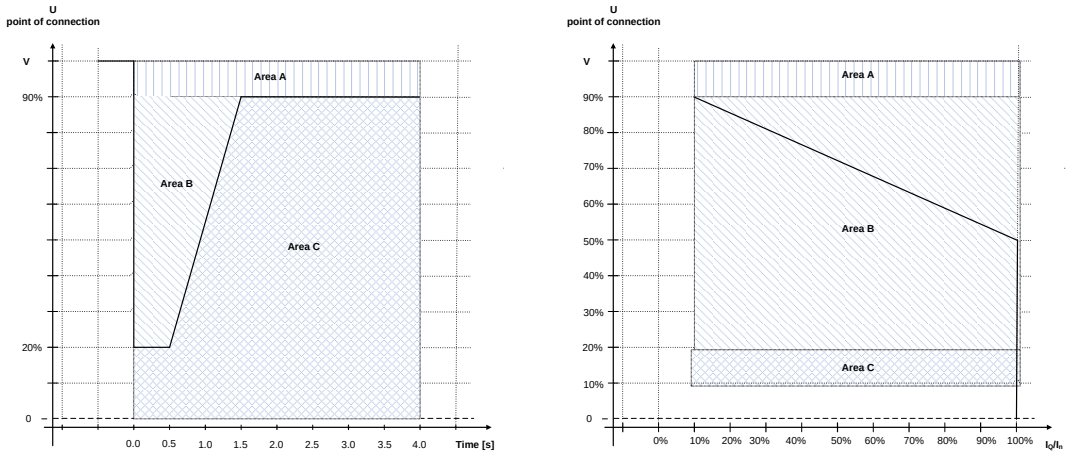


(a) Requirements concerning voltage drop toleration.

(b) Requirements concerning reactive current injection.

Figure 1.3: Danish grid codes. FRT regulations for wind power plants with a power output greater than 1.5 MW, as of September 2010.

Transients of torque, active power and reactive power will follow accordingly, the torque oscillation translating into a considerable mechanical stress for the wind turbine. Moreover the stator current disturbance is transmitted to the rotor, causing uncontrollable currents that can produce damage to the rotor converter due to the over-currents and to the DC-Link capacitor due to over-voltages.

Old control strategies for DFIG based WT proposed disconnecting the stator from the grid in case of a severe fault, and protect the power electronics by activating a protection device called crowbar, see Figure 1.4(a). By employing this strategy the problems caused by the fault currents are avoided. However this methodology can not be used anymore since, as previously stated, the new grid codes require the turbine to remain connected during faults.

Under these circumstances the basic safety operation requirements for a DFIG during a stator short circuit fault, along with the new grid code requirements, can be summarized in a list of the most important requirements a modern DFIG based wind turbine should fulfill during a grid fault:

- Requirement 1 - protection of the rotor side converter from over-currents
- Requirement 2 - protection of the DC-Link capacitor from over-voltages
- Requirement 3 - minimizing the stress on the mechanical system
- Requirement 4 - ride through capability for all types of grid faults (symmetrical and unsymmetrical)

- Requirement 5 - grid voltage support through reactive current generation capability during fault

## 1.2 Previous work - a critical review

The requirements imposed by the latest grid codes generated a new movement in the DFIG research area. New algorithms and topologies, as the ones presented in Figure 1.4 have been proposed and analyzed in the past years.

As initial background for the current report, research has been carried out by the authors during the autumn semester of the 2010-2011 academic year. The carried activities together with the main conclusions will be briefly summarized here.

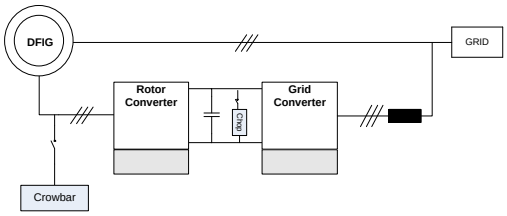


(a) DFIG system with rotor crowbar and DC-Link chopper.

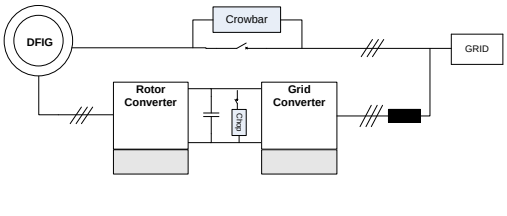


(b) DFIG system with stator crowbar and DC-Link chopper.

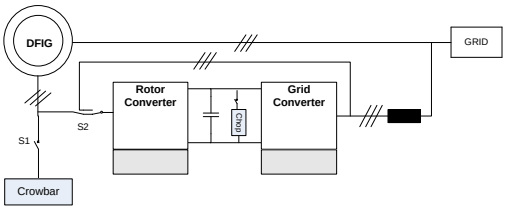


(c) DFIG system with rotor crowbar, DC-Link chopper and extra connection of the rotor side converter to the grid.

Figure 1.4: Different topologies of DFIG based systems able to ride through faults.

The initial goal of the project was to provide theoretical and practical understanding of DFIG based wind turbines control under normal and fault ride through operation. An in-depth literature survey has been carried and different aspects regarding DFIG operation and control were analyzed. From all the strategies presented in the literature the focus was set on the ones that offered a good trade-off between complexity and performance.

For normal operation, the control of the rotor side converter was implemented in a rotating reference frame aligned with the stator flux, while the control of the grid side converter was designed in the grid voltage rotating frame. For fault operation, different control strategies were employed for both the rotor crowbar and the DC-Link chopper. A variation of the classic topology, presenting the crowbar mounted on the stator (Figure 1.4(b)) was implemented and compared with the original one. Some basic flux damping methods were also evaluated.

Simulation models accounting for all the operating modes of a DFIG based WT were created and different test cases were employed in order to test the performance of the afore mentioned strategies and techniques.

- **Case 1.1**: Rotor mounted crowbar, activated once at the beginning of the fault for 100ms. Hysteresis activated DC-Link chopper.
- **Case 1.2**: Rotor mounted crowbar, activated once at the beginning of the fault for 100ms. Hysteresis activated DC-Link chopper. Basic torque damping strategy.
- **Case 2.1**: Rotor mounted crowbar, activated twice for 100ms, once at the beginning of the fault and once at the fault clearing moment. Hysteresis activated DC-Link chopper.
- **Case 2.2**: Same as Case 2.1; activation time increased to 200ms.
- **Case 3**: Rotor mounted crowbar, activated by hysteresis. Hysteresis activated DC-Link chopper.
- **Case 4**: Stator mounted crowbar activated twice for 20ms, once at the beginning of the fault and once at the fault clearing moment. Hysteresis activated DC-Link chopper. Basic torque damping strategy.

Case 1.1 and 1.2 tested the capabilities of the timer activated crowbar strategy. It was concluded that only the rotor current spike appearing at the beginning of the fault can be eliminated using this strategy. The torque damping possibilities are poor and the reactive current injection yields unsatisfactory results. The only requirement that is properly accomplished is the protection of the DC-Link.

Case 2.1 and 2.2 approached a strategy that activates the crowbar twice. Once at the beginning of the fault and once at the fault clearing moment. It was observed that by using this strategy both overcurrents were damped, but the generation of reactive current deteriorated considerably. The activation time of 200ms, even though it yielded better results, can be unacceptable for certain grid codes, including the Danish one. This particular one requires the reactive current reference to be followed after 100ms from the fault detection with a tolerance of 20%.

Another strategy that yielded good results in limiting the rotor current was by controlling the crowbar through a continuous hysteresis on-off control (Case 3). Every time the rotor current exceeded the upper threshold, the crowbar was activated and deactivated moments later, when the current reaches the lower limit. The value used for the crowbar resistance was an issue of trial and error in all the cases since literature only provides empirical methods for determining this parameter.

The last considered case, and the one that yielded the most encouraging results places the crowbar on the stator of the machine rather than on the rotor. The crowbar was controlled through a timer strategy that triggers it at the beginning and at the end of the fault for 20ms. In order to try to improve the system

response even further, a basic torque damping strategy has been considered. This strategy best performed in terms of rotor current limitation, torque damping and reactive current injection. The main advantage of this method is that the rotor side converter remains connected and it can start providing reactive current together with the line side converter at the moment of fault detection.

The performance of the employed strategies deteriorated seriously when the system was exposed to unbalanced voltage drops. Providing fault ride through capability for unsymmetrical faults considerably increases the complexity of the control structure.

The main conclusion at the end of the project was that none of the suggested topologies and control algorithms can fully satisfy the requirements mentioned in the previous section, as it can be seen in Table 1.1.

Table 1.1: Table (Performance comparison between different FRT strategies and topologies)

| | Case 1.1 | Case 1.2 | Case 2.1 | Case 2.2 | Case 3 | Case 4 |
|---|---|---|---|---|---|---|
| Requirement 1 | Partial | Partial | YES | YES | YES | YES |
| Requirement 2 | YES | YES | YES | YES | YES | YES |
| Requirement 3 | NO | NO | NO | NO | NO | YES |
| Requirement 4 | NO | NO | NO | NO | NO | NO |
| Requirement 5 | Partial | Partial | Partial | Partial | Partial | YES |

## 1.3 Project outline and limitations

The previous section briefly covered the prior work regarding DFIG fault ride through operation and control. Several topologies and strategies were investigated through simulation. After discussions with company and university representatives the need of extensive investigation of the capabilities of the DFIG with rotor mounted crowbar and DC-Link chopper topology was identified.

Previous simulation results showed that the classical implementation of this topology can not ride through low voltage drops. In this context, questions like "What are the maximum capabilities of this system?" and "How the control strategy can be redesigned or improved in order to achieve LVRT wholly or partially?" needed to be answered. Emphasis was set on improving the rotor side converter control in order to uphold as much as possible during fault conditions. Maintaining the rotor side converter in control being a key point in order to satisfy the reactive power injection requirement imposed by the grid codes.

Another aspect that was later added to the initial scope of the project was to test how the improved control strategies for the rotor side converter would benefit to a DFIG system with a stator crowbar. This type of system, even though not economically sufficient at the current moment, demonstrated promising results, as seen in the previous section, so further investigation was considered appropriate.

The DFIG based WT is a complex system, that poses challenges even under normal

operation. Even more, implementing FRT capability, as required by the grid codes, to such a system is a task that involves a lot of work and investigation. In order to scale the size of the project to one realizable in the allocated time, several simplifications and limitations were applied to the generic theme.

The grid requirements impose that a WT should ride through all types of faults (symmetrical, unsymmetrical, with phase shift, reoccurring, etc.). As a simplification, only simple, symmetrical faults were considered for the current project both in simulation and experimental work.

Since access to a full-scale system was not possible, a reduced-scale laboratory setup was assembled in order to partially validate the implemented concepts. Since the main point of interest for the project was the control of the rotor side converter, an extra simplification was applied to the experimental setup. The grid side converter was connected to a separate grid that does not experience the voltage sag during fault operation. The extent and the quality of the obtained experimental results was also influenced by factors such as available laboratory equipment and safety regulations.

The results obtained through this project are documented by the present report, and organized as follows: Chapter 2 provides theoretical background about the DFIG based WT running in normal operation. The basic behavior as well as the used control structure for the rotor and grid side converter are presented here.

Chapter 3 presents an in-depth look at the behavior of the DFIG system under fault conditions. The modifications and the challenges that have to be overcome both at a structural level and at a control level are covered here.

Chapter 4 gives a detailed overview of the developed simulation models. The chapter is divided in two subchapters, the first describes the components used in the modelling of the plant system while the second presents the used control structure.

In order to test the accuracy of the developed simulation models, different testing scenarios were performed on a full scale system (2 MW). The results are further detailed in Chapter 5 of the current report.

A lot of effort has been oriented towards assembling a laboratory scale system in order to validate the results obtained through simulations. The description of the setup can be found in Chapter 6 and the performed laboratory experiments are detailed in Chapter 7.

The last chapter is dedicated to conclusions on the obtained results and overcome challenges as well as possible directions for future work in the area.

# Chapter 2

# DFIG under normal operation

## 2.1 System Description

The typical DFIG configuration is presented in Figure 2.1, in this configuration, the stator is directly connected to the grid, while the rotor is connected to a back-to-back converter.

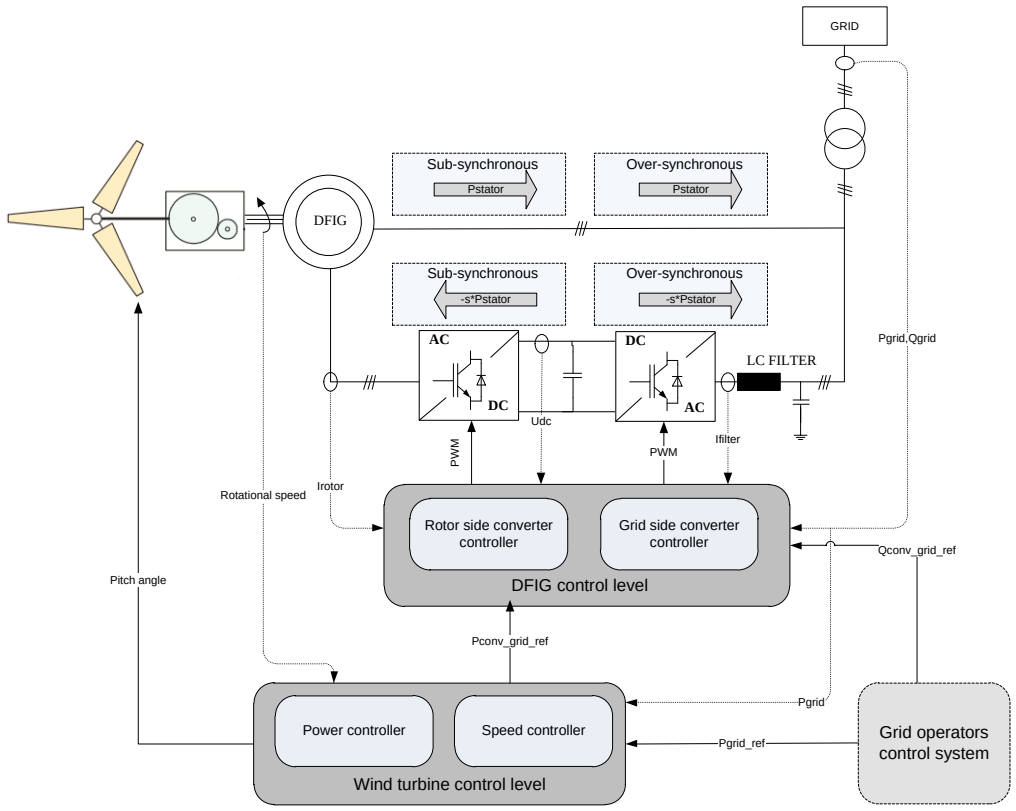


Figure 2.1: Principle of power flow in DFIG

The back-to-back power converter consists of two voltage source inverters con-

nected to a common DC-Link. With the use of these two converters the rotor currents can be controlled, by directly controlling the rotor voltages through a PWM strategy. Through proper regulation of the rotor currents, the desired active and reactive power, flowing through the DFIG stator, can be achieved [12, 22].

The size of the back-to-back converter depends on the operational speed range. Usually, for an operational speed range about ±30% of the synchronous speed, the converter has to handle the corresponding power, and this resulting in a rating for the converter of approximately 30% of the generator rated power [22], a major advantage for the DFIG based wind turbines.

Another advantage of the DFIG based wind turbine is that it is able to operate at both *sub-synchronous* and *over-synchronous* speed. This implies that the power will flow in both directions through the converter, reason why a back-to-back (bidirectional) converter is used. This conclusion can also be reached by analyzing the relation between the stator, rotor and grid power, as presented in (2.1) [12], where the stator power, $P_{stator}$, can be defined as a function of the grid power, $P_{grid}$, while the rotor power, $P_{rotor}$, also referred to as slip power, can be expressed using the slip and $P_{stator}$.

$$P_{stator} = \frac{P_{grid}}{1 - s} \tag{2.1}$$

$$P_{rotor} \approx -sP_{stator} \tag{2.2}$$

Where slip $s$ is defined as (2.3), with $n_{syn}$ and $n_{gen}$ as the synchronous and the generator speed, respectively.

$$s = \frac{n_{syn} - n_{gen}}{n_{syn}} \tag{2.3}$$

Furthermore, for the doubly-fed induction generators, the relationship between the rotor peak voltage $V_r$ and the stator peak voltage $V_s$, can be approximated as in (2.4), depending on the rotational slip $s$ and the machine stator-to-rotor turns ratio $n$.

$$V_r \approx \pm s\frac{V_s}{n} \tag{2.4}$$

This relation, in conjunction with the equations for the fundamental voltage peak magnitudes that can be obtained through PWM modulation of the back-to-back converter(2.5), can be used to determine the speed range of the generator [21], as given by relation(2.7).

$$V_s = m_1\frac{U_{dc}}{2} \tag{2.5}$$

$$V_r = m_2\frac{U_{dc}}{2} \tag{2.6}$$

$$s \approx \pm n\frac{m_2}{m_1} \tag{2.7}$$

Where $m_1, m_2$ are the PWM modulation depths of the stator-side and rotor-side converters respectively, with a theoretical range of $0 < m_a \leq \frac{2}{\sqrt{3}}$ when *sinusoidal PWM modulation* with *zero sequence signal injection* is employed [24], $U_{dc}$ the dc-link voltage magnitude, and $V_s, V_r$ the stator and rotor phase peak voltages.

### Control system overview

The major control goals of a variable speed wind turbine, thus a DFIG based wind turbine are:

- maximum power extraction and active power control at the *Point of Common Coupling*
- reactive power control at the *Point of Common Coupling*

Because the electrical and mechanical wind turbine subsystems have different time scales, two cross-coupled control levels can be distinguished [12], as presented in Figure 2.1:

- the *DFIG control level*.
- the *Wind turbine control level*.

The *DFIG control level* contains the electrical control (converters and machine) of the DFIG and has a fast dynamic response, its aim is to control the active and reactive power, flowing from the DFIG into the grid.

The wind turbine control level, which has slower dynamics, controls the pitch angle and provides the active power reference for the DFIG control level.

A brief description of the two control levels is provided next.

### DFIG control level

At this level, the control of active and reactive power is performed independently. This is achieved by decoupling the voltage and currents related to the active and reactive power, respectively. The decoupling can be made with the use of a special reference frame.

Two sub-control levels, one for each converter in the back-to-back configuration, can be found at this control level:

- *Rotor side converter controller*.
- *Grid side converter controller*.

The purpose of the *rotor side converter* is to control the active and the reactive power in the stator winding of the DFIG [21], whilst the *grid side converter* control

aims to keep the DC-Link voltage level constant and to assure zero reactive power at the output of the converter [22].

Both the grid side and the converter side controllers will be treated thoroughly in the following sections.

#### Wind turbine control level

The control strategies for the turbine are based on the power vs. wind curve, as presented in detail in [12], having the main control goals of power optimization and power limitation. For this, two cross-coupled controllers are used, one *speed controller* and one *power controller*.

The main task of the *speed controller* is to achieve optimum power by adapting the generator speed to the reference speed $\omega_{gen}^{ref}$. For wind speeds above rated value, the speed controller needs to prevent the speed of the generator from becoming too large.

The *power controller* has the purpose to limit the generator power at rated power for wind speeds at and above rated value. This is achieved by increasing or decreasing the pitching angle $\beta$ based on the measured actual generated power.

Since the time constants of the wind turbine controllers are much slower compared to the dynamics of the DFIG controllers and electrical system, they can be considered constant for the time ranges relevant for FRT, thus the wind turbine control level will not be detailed any further.

## 2.2 System Modelling

### 2.2.1 Doubly-fed induction generator modelling

In order to analyze and control the doubly-fed induction generator a dynamic model of the machine is required. The analysis is started from the general dynamic model of an induction machine represented in an arbitrary reference frame, rotating with angular speed $\omega$. Such a model is described in [15], and represented by the equivalent circuit in Figure 2.2. The main simplification assumptions used in deriving this widely employed model are: symmetrical windings, sinusoidally distributed, no saturation effects and no iron losses.

The stator and rotor voltage equations $\overrightarrow{V_s}$ and $\overrightarrow{V_r}$, represented in an arbitrary reference frame, rotating with angular speed $\omega$, and referred to the stator side, can be expressed as in equation (2.8) [15].

$$\begin{aligned} \overrightarrow{v_s} &= R_s \overrightarrow{i_s} + j\omega \overrightarrow{\psi_s} + \frac{d\overrightarrow{\psi_s}}{dt} \\ \overrightarrow{v_r} &= R_r \overrightarrow{i_r} + j(\omega - \omega_r)\overrightarrow{\psi_r} + \frac{d\overrightarrow{\psi_r}}{dt} \end{aligned} \tag{2.8}$$

With the stator and and rotor flux vectors $\overrightarrow{\psi_s}$ and $\overrightarrow{\psi_r}$ expressed as in equation (2.9).

$$\begin{aligned} \overrightarrow{\psi_s} &= L_s \overrightarrow{i_s} + L_m \overrightarrow{i_r} \\ \overrightarrow{\psi_r} &= L_r \overrightarrow{i_r} + L_m \overrightarrow{i_s} \end{aligned} \tag{2.9}$$

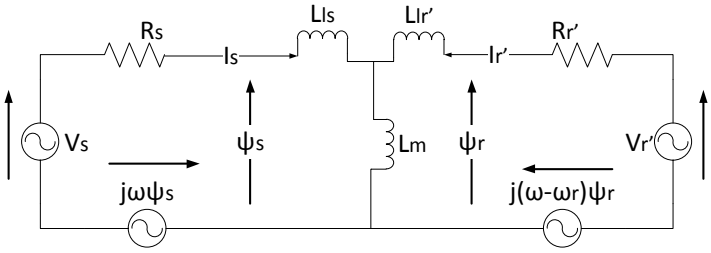


Figure 2.2: Equivalent circuit of a DFIG in an arbitrary reference frame rotating at a speed of $\omega$, referred to the stator side.

The general dynamic DFIG model can be represented in different reference frames, such as stationary, rotor or synchronous reference frames, by selecting the angular speed of the frame $\omega = 0$, $\omega = \omega_{rotor}$ or $\omega = \omega_{synchronous}$, depending on the application [29].

### 2.2.2 Grid filter modelling

The electrical model of a *damped LCL filter* is presented in Figure 2.3, where $V_{ia}, V_{ib}, V_{ia}$ are the fundamental voltages generated by the grid side inverter and $V_{ga}, V_{gb}, V_{ga}$ are the grid phase voltages. A passive resistor damping of the filter capacitor has been chosen, for simplified control design and in order to avoid resonance problems. Also it is assumed that the grid and trafo impedances are included in the model.

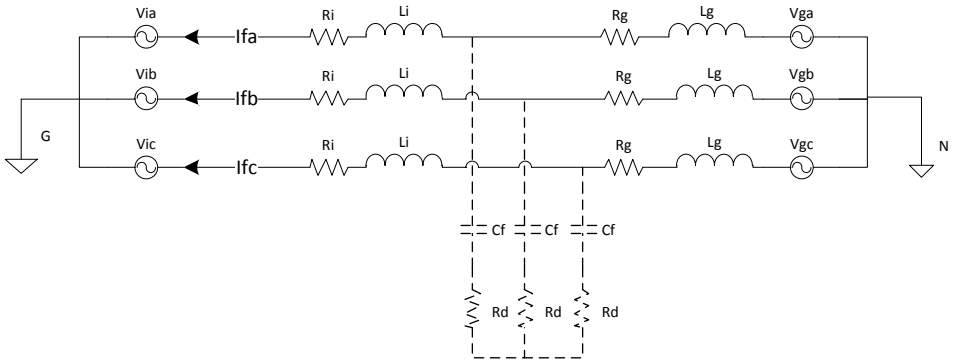


Figure 2.3: Equivalent circuit of a damped LCL filter in the stationary reference frame.

In order to derive the a *simplified grid filter model* for control design, the total filter impedance is calculated as (2.10):

$$\begin{aligned} R_f &= R_i + R_g \\ L_f &= L_i + L_g \end{aligned} \tag{2.10}$$

and by neglecting the damped capacitors, the simplified model equations can be written in an arbitrary reference frame, rotating with angular speed $\omega$ as (2.11):

$$\overrightarrow{v_g} = R_s \overrightarrow{i_f} + L_f \frac{d\overrightarrow{i_f}}{dt} + j\omega L_f \overrightarrow{i_f} + \overrightarrow{v_i} \tag{2.11}$$

These simplified equations will only be used for synthesizing the control of the grid side filter, as the full electrical model will be used for detailed modelling of the plant.

## 2.3 System Control

*Vector oriented control in synchronous reference frame* strategy was chosen for implementing the control strategies for the rotor and grid side converter, due to some of the advantages that this method posses [26]:

- wide range of bibliographic material available
- good dynamic response in normal and fault operation
- fixed switching frequency
- robust to parameter variation
- robust to measurement noise

Other DFIG control strategies currently employed are:

- Vector oriented control in rotor/stationary reference frame [18]
- Direct torque control [26]
- Direct power control [26]

Some disadvantages of the *vector oriented control in synchronous reference frame* strategy, in comparisons with the other methods are [26]:

- slower response time compared to the direct methods
- higher complexity
- need to estimate the flux angle

### 2.3.1 Rotor side converter control

The rotor side converter has two main purposes, one is to control and synchronize the stator voltages to the grid, in the startup phase. The second is to independently control the active and reactive power during normal and fault operation. This can be done either at the generator stator, or at the point of common coupling, in which case the grid side converter power is considered implicitly [12, 19]. In the current project, the stator active and reactive power have been chosen as the control variables, in order to have a better differentiation between the rotor side and the grid side converter controllers.

For the purpose of DFIG control, the *stator/grid flux synchronous reference frame* [13, 21] is most often employed. But there are other possibilities to align the synchronous reference frame: to the stator voltage [19], the air-gap flux [29], or the rotor flux [19] vectors. In these reference frames, the control variables appear as dc values, and classical *PI* control can be employed.

There is also the possibility to employ the rotor reference frame [18], where the control variables appear as ac values, and *adaptive Proportional-Resonant* controllers have to be employed, which are equivalent to the *PI* controllers in the synchronous reference frame.

As previously mentioned, *vector oriented control* was chosen to design the rotor side converter controllers, in *stator/grid flux synchronous reference frame*, as presented in Figure 2.4. The advantage of using this reference frame is the possibility to decouple the stator active and reactive power controllers, by regulating the impressed rotor currents [21, 13, 19].

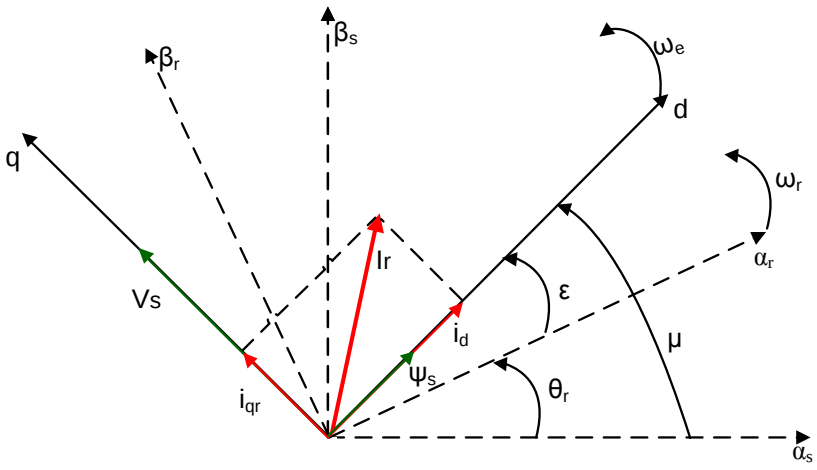


Figure 2.4: Stator/grid flux reference frame

As noticed in Figure 2.4, the *stator/grid flux synchronous reference frame* is obtained by aligning the direct axis of a rotating reference frame with the stator

flux vector $\overrightarrow{\psi_s}$. This posses two important requirements that have to be met first: accurate determination of the rotor angle $\theta_r$, usually by means of an encoder, and estimation of the stator flux angle $\mu$, by use of a *phase-locked loop*(PLL) technique, or other methods of stator flux angle estimation.

A commonly used method for estimating the stator flux angle $\mu$ is presented in [21, 13, 22]. By neglecting the stator resistance, the following approximation between the stator voltage $\overrightarrow{v_s}$ and the stator flux $\overrightarrow{\psi_s}$, in the stationary reference frame ($\omega = 0$) denoted by $s$, can be made:

$$\overrightarrow{v_s^s} \approx \frac{d\overrightarrow{\psi_s^s}}{dt} \tag{2.12}$$

From (2.12), it can be observed the stator voltage vector is $\pi/2$ in advance of the stator flux vector, thus greatly simplifying the calculation of the stator flux angle:

$$\mu = \theta_s - \frac{\pi}{2} \tag{2.13}$$

where $\theta_s$ is the stator voltage phase angle.

This method of estimating the stator flux is widely employed in the literature related DFIG control, and is also known as *grid flux orientation* [22].

Other methods for estimating the stator flux are more dependent on machine parameters and measurements [13], and are thus less robust.

Once the stator/grid flux reference frame angles are obtained, the control strategy can be implemented as in Figure 2.5. Two cascaded control loops can be observed in this strategy, a slower (outer) power control loop and a fast (inner) rotor current control loop.

The power control loop controls the active and reactive power, while the very fast current control loop regulates the machine's rotor currents to the reference values that are specified by the slower power controller [13, 21, 12]. Such a cascaded control structure is advantageous as the electrical and mechanical dynamics are in different time scales, the electrical dynamics being much faster than the mechanical dynamics. Since the electrical dynamics are the fastest, the rotor current control loop is the inner loop [12].

As mentioned at the beginning of the chapter, one role of the rotor side converter controller is to *synchronize* the DFIG stator voltage to the grid voltage, in amplitude, phase and frequency, in order to safely connect the DFIG stator to the grid. This is an important issue for the DFIG based wind turbines, not present in the full scale converter wind turbine configurations.

The *synchronization phase* of a DFIG based wind turbine consists of:

- estimation of the initial rotor angle
- determination of the grid voltage phase, frequency and amplitude by PLL
- control of the stator voltage, through the rotor currents, by using a control strategy similar to the one presented in Figure 2.5

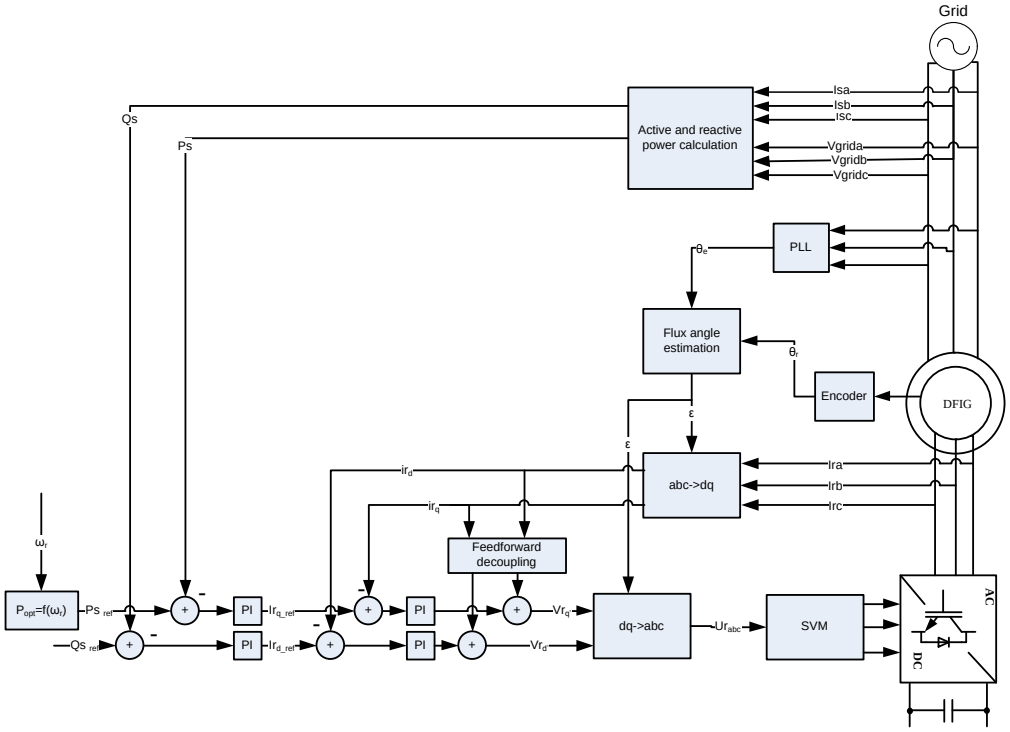


Figure 2.5: Rotor side converter control concept.

An important aspect for grid connected renewable energy sources, like the DFIG based wind turbines, is the fast and accurate determination of the grid voltage phase, frequency and amplitude. This issue is of great interest not only for the synchronization and normal operation phase of the DFIG, but also for the fast detection and riding of grid faults.

Special *phase-locked loop* techniques have to be employed for fast in accurate detection in case of unbalanced grid or faults. The *double-synchronous reference frame PLL* proposed in [20], which is able to determine the phase, frequency and amplitude of the positive and negative grid voltage components, has been adopted in the present project.

Further details regarding modelling, control design and implementation of the DFIG and the rotor side converter will be presented in Chapter 4.

### 2.3.2 Grid side converter control

The grid side converter has also a dual role, one is to control the DC-Link voltage, and the other is to control the reactive power injected into the grid. Usually the grid side converter is operated at unity power factor, but it can be used for voltage support during grid faults, by injecting reactive power in the grid.

*Vector oriented control* was chosen in this case also, aligned to the *grid voltage synchronous reference frame*, presented in Figure 2.6, obtained estimating the grid

voltage phase angle $\theta_s$, through a PLL technique.

There is also the possibility to employ other reference frames for designing the control, like the natural reference frame or the stationary reference frame [5], where *Proportional-Resonant* controllers are employed, equivalent with the *PI* controllers in the synchronous reference frame.

Similar to the rotor side converter control, this reference frame gives the possibility to decouple the active and reactive current controllers, by regulating the impressed grid filter currents [21, 22].

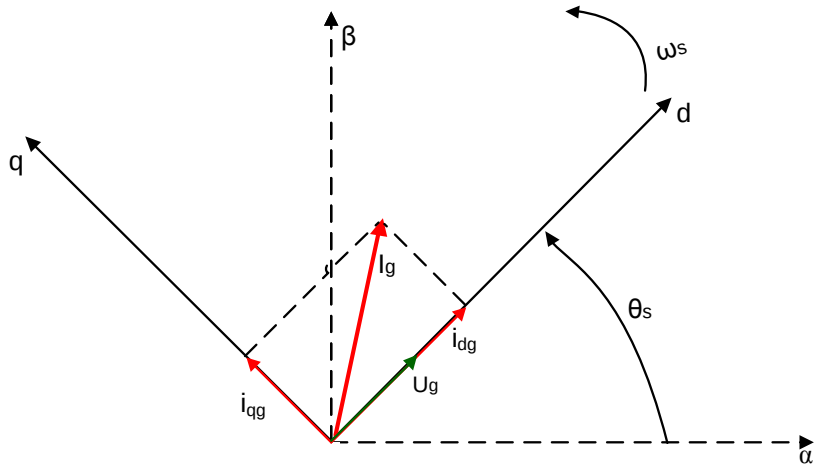


Figure 2.6: Grid voltage reference frame

The *grid filter* is usually of *LC* or *LCL* type, specifically designed to obtain a low current THD at the given operation conditions. There are several important issues that have to be taken into consideration when designing and controlling a *LCL* grid filter, treated in detail in [17], but which are out of the scope of the present project. As mentioned previously, a damped LCL filter has been chosen for the grid side filter, in order to avoid resonances and simplify the control.

The control concept for the grid side converter, as presented in Figure 2.7, similar to the rotor control strategy, consists of two cascaded control loops, a faster(inner) grid filter current control loop, and a slower(outer) DC-Link voltage/power control loop.

As mentioned earlier, the *grid voltage synchronous reference frame*, allows a decoupling of the active and reactive currents control.

Thus by controlling the *active component* of the grid filter current, the power injected into the DC-Link capacitor can be controlled, and in consequence the DC-Link voltage level.

Similarly, by controlling the *reactive component* of the grid filter current, the

reactive power injected into the grid can be controlled, but which is kept at zero reference during normal operation.

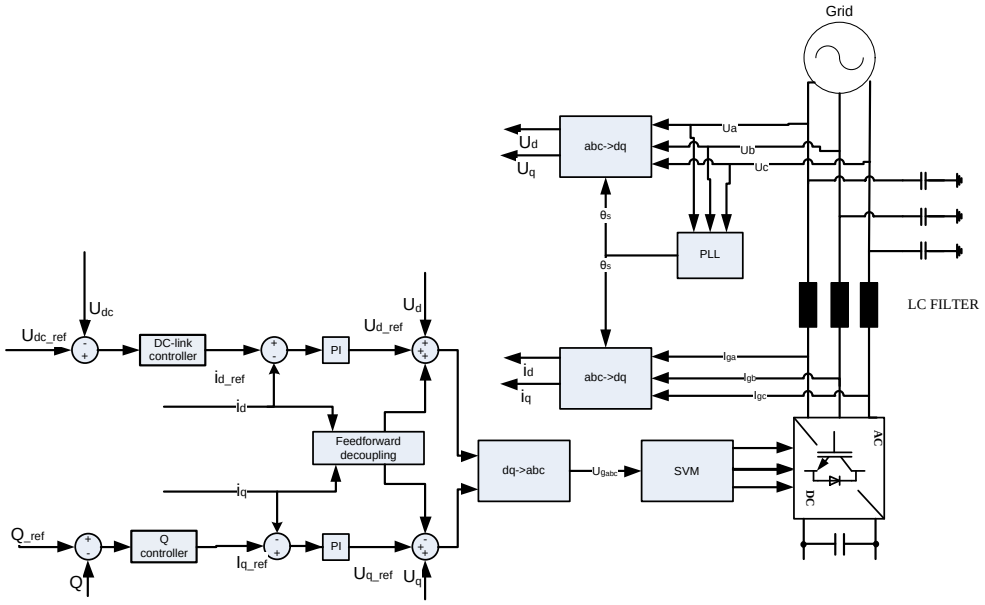


Figure 2.7: Grid side converter control concept.

Further details regarding modelling, control design and implementation of the grid filter and of the the grid side converter will be presented in Chapter 4.

# Chapter 3

# DFIG under fault condition

## 3.1 System behavior

During a grid short circuit fault, the DFIG based wind turbines have to face a big challenge, especially in light of the new stringent grid codes, which require dedicated control and protection measures. All issues can be tracked down to the stator-grid connection of the DFIG, and the small rotor power converter, which has to compensate, at least partially, the disturbances introduced into the DFIG during the grid fault.

In the following, some of the most important challenges that arise in a DFIG based wind turbne, during a grid fault, will be presented. As a demonstration, a detailed simulation for a DFIG based wind turbine, without any fault-ride through strategy implemented, during a severe voltage sag, has been carried out. A similar approach was described in [9], and is the base of the current analysis.

A voltage sag to 0.2 p.u. of the nominal grid voltage, as presented in Figure 3.1, can lead to large stator and rotor over currents, up to $2-5$ p.u. The rotor over currents can block the rotor side converter, or even damage the power electronics.

These currents appear as a consequence of the sudden voltage sag, which cause stator current DC-components to be induced into the system. On the rotor side these currents appear as AC, superposing the much slower steady-state rotor currents injected by the converter [9].

The high rotor currents lead to over voltages in the DC-Link capacitor, which also can damage the converter, if no protection measures are taken. In the simulation results presented in Figure 3.2, a rising of the DC-Link voltage to 1.4 p.u. can be observed. This value is limited by the fast controllers, but can get even higher, to $2-3$ p.u., as reported in the literature [9].

Disturbances and oscillations of the electromechanical torque, can cause severe stress on the wind turbine shaft, especially when the fault recovers.

A closer look at the DFIG vectorial model, presented in (2.8, 2.9), can give some insight into the problems that arise inside the generator during a grid voltage sag.

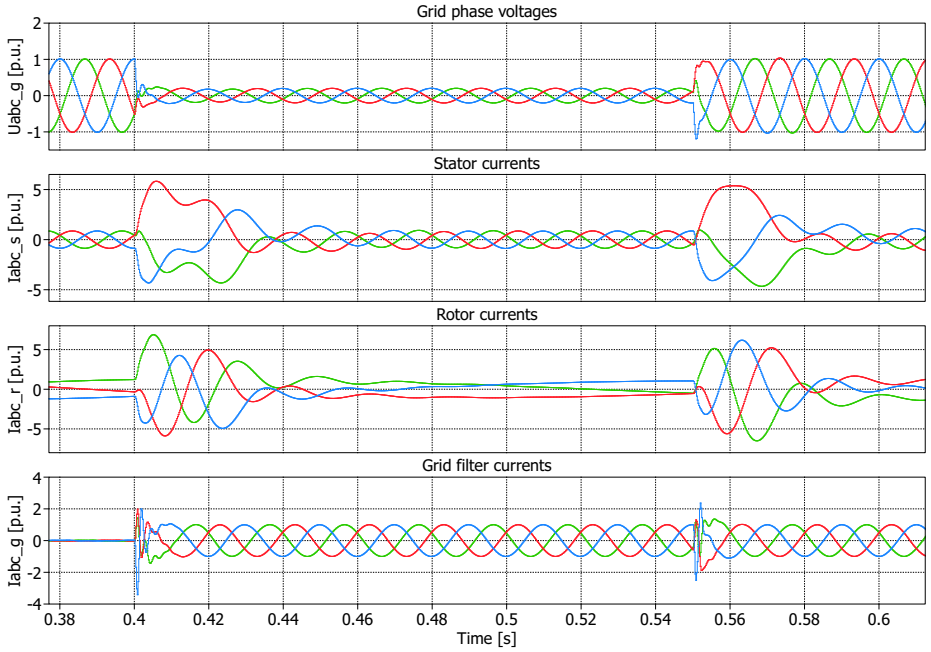


Figure 3.1: DFIG based WT voltage and currents during a severe voltage sag.

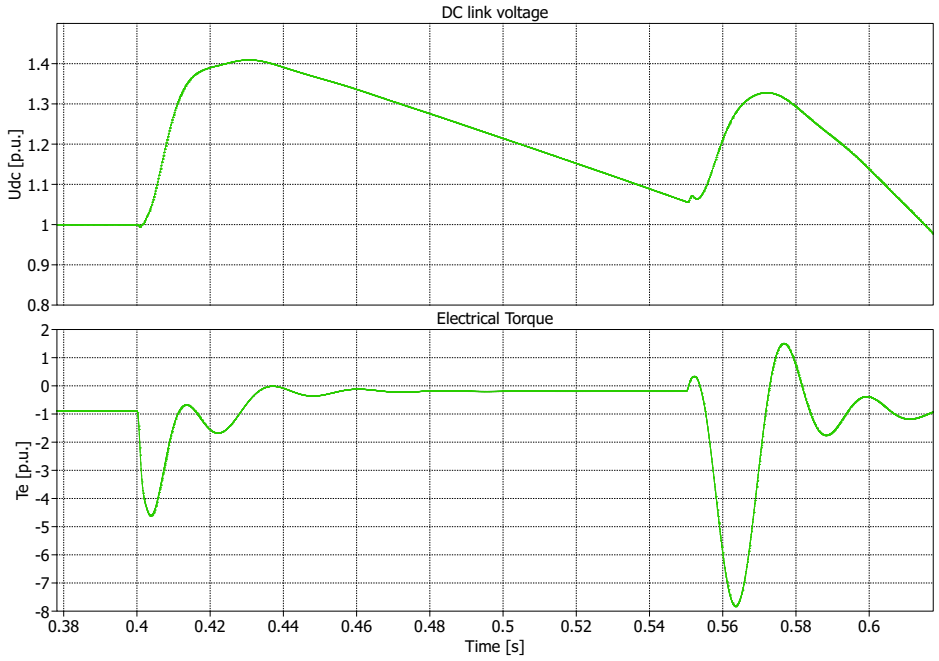


Figure 3.2: DC-Link voltage and electromechanical torque during a severe voltage sag.

First, by writing the stator flux equations in the *stationary reference frame* (3.1), it can be observed that a sudden jump in then stator voltage, as would happen during a grid short circuit fault, would introduce a DC-component in the stator flux.

$$\overrightarrow{\psi_s} = \int \left( R_s \overrightarrow{i_s} - \overrightarrow{v_s} \right) dt \tag{3.1}$$

The DC-components induced in the stator flux, can be observed more clearly in Figure 3.3. They appear both at the beginning and the clearing of the fault.

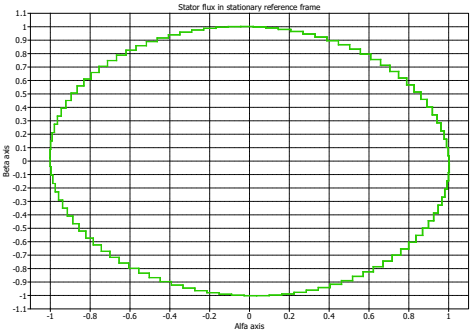


(a) Stator flux in normal operation

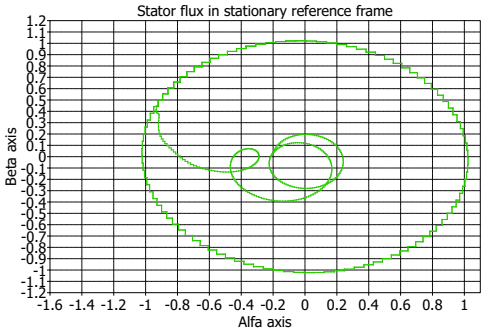


(b) Stator flux at the start of the fault

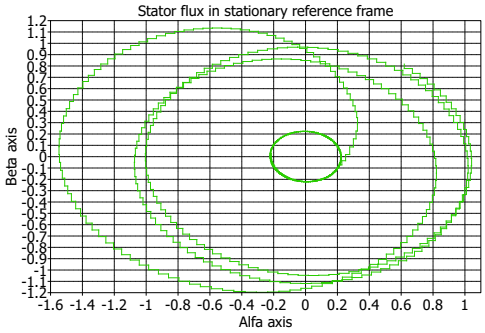


(c) Stator flux at the end of the fault

Figure 3.3: Stator flux DC-components in stationary reference frame.

These DC-components in the stator flux, in correlation with the jump in the stator flux derivative, will induce large rotor voltages which create most of the problems during a fault. This becomes more obvious by rewriting the rotor equations in the *arbitrary rotating reference frame* ($\omega$), in terms of rotor voltages, currents and stator flux, as in (3.2):

$$\overrightarrow{v_r} = R_r \overrightarrow{i_r} + \sigma L_r \frac{d\overrightarrow{i_r}}{dt} + \frac{L_m}{L_s} \frac{d\overrightarrow{\psi_s}}{dt} + j(\omega - \omega_r)\sigma L_r \overrightarrow{i_r} + j(\omega - \omega_r)\frac{L_m}{L_s}\overrightarrow{\psi_s} \tag{3.2}$$

where $\sigma = 1 - \frac{{L_m}^2}{L_s}$.

The $\frac{L_m}{L_s}\frac{d\overrightarrow{\psi_s}}{dt}$ voltage component, is created by the variation of the stator flux, which can be neglected during steady state, but can reach large values during a steep change in stator flux.

The second voltage component, $j(\omega - \omega_r)\frac{L_m}{L_s}\overrightarrow{\psi_s}$, represents the back e.m.f. created by the rotating stator flux, and can increase, if the stator flux contains DC-components. The DC components increase the back e.m.f. because on the rotor side, they are rotating with the rotor frequency, instead of the slip frequency.

The DC-components of the stator flux, can be observed more clearly, in the *synchronous rotating reference frame*, where they rotate at the mechanical rotor frequency, as in Figure 3.4.

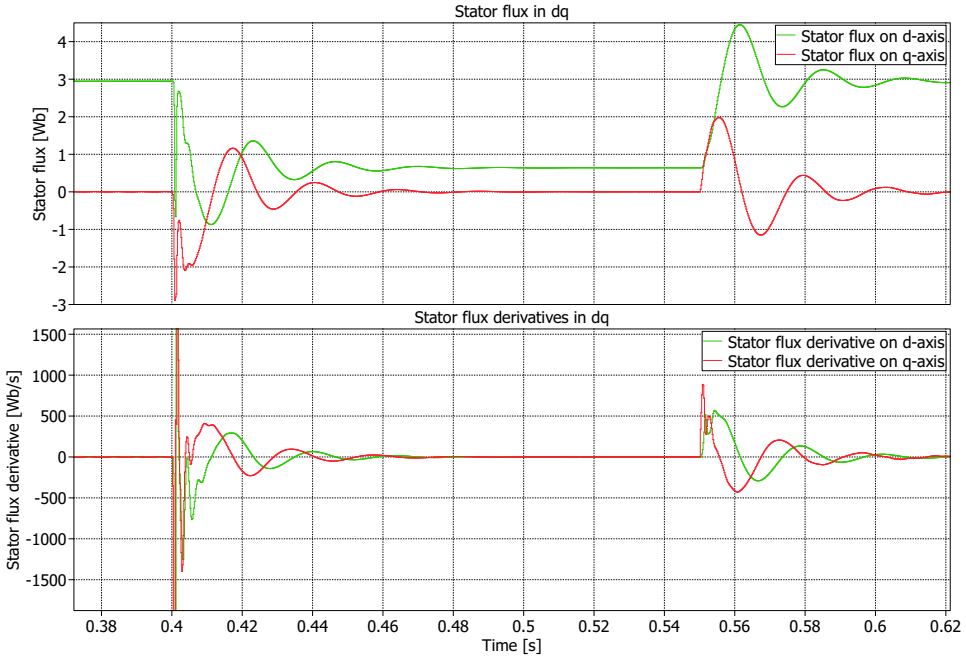


Figure 3.4: Stator flux in synchronous rotating reference frame during severe voltage sag.

Also the large magnitude of the stator flux derivatives, at the beginning and the end of the fault, will yield a large voltage component in the rotor windings of the DFIG. These voltage components, are basically disturbances in the system, and will have to be compensated by the control system, during fault ride-through.

### 3.1.1 Protection devices

Having presented the major problems that arise in a DFIG based wind turbine during a grid short circuit fault, there are several protection measures currently employed or researched, some of which were reviewed in the previous project and mentioned in the first chapter.

In the present project the *rotor crowbar* topology, and the simple *dc chopper*, as in Figure 3.5, have been implemented and compared to the newer *stator crowbar* topology.

At the moment there is an important debate regarding the economical feasibility of implementing new/extra power electronics into existent DFIG systems, as is the *stator crowbar*, or other solutions [23, 14], which would decrease the cost advantage of the DFIG based systems in comparison with the *full scale converter* systems. These economical aspects are left out the scope of the current project, as the focus is shifted more towards the theoretical aspects of DFIG fault-ride through.

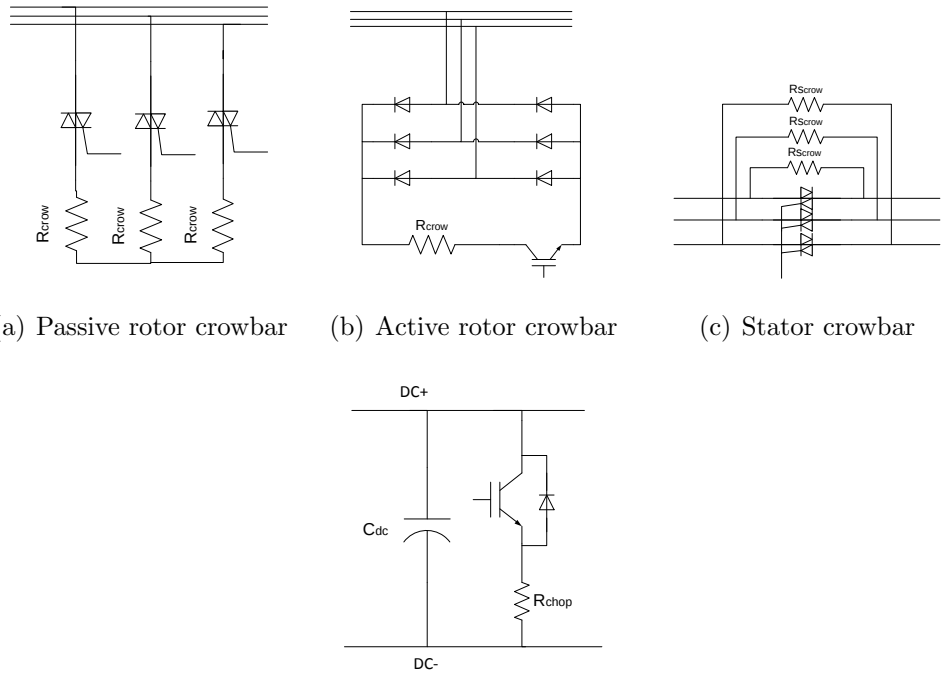


(a) Passive rotor crowbar (b) Active rotor crowbar (c) Stator crowbar

(d) DC chopper

Figure 3.5: Crowbar types and dc chopper.

Basically the rotor crowbar is a bank of bypass resistors connected at the rotor windings by controllable switches, as presented in Figure 3.5, and is among the most adopted solutions for protecting the rotor side converter [25, 16, 27, 23].

There are two main types, in which the crowbar circuit can be categorized, depending on the power electronics employed for switching the crowbar [25]:

- the *passive crowbar* constructed using thyristors as in Figure 3.5(a), which allow closing the circuit but not opening it until the zero-crossing of the rotor currents, which at low rotor frequencies can take hundreds of milliseconds
- the *active crowbar* is constructed using IGBTs, which allow opening the circuit in forced commutation, as in Figure 3.5(b), this configuration can also include a capacitor and be controlled just like a dc chopper

During rotor crowbar activation, the generator rotor windings are short circuited through the crowbar circuit, and the rotor currents are limited accordingly to the crowbar resistor dimensioning. Meanwhile, the RSC is deactivated, and control of the DFIG is lost, the generator behaving like a squirrel cage machine [25]. From

this behavior two significant challenges regarding the rotor crowbar topology can be observed:

- control of the generator is lost during crowbar activation, thus no reactive power support or torque oscillation damping can be achieved through the machine side [25]
- the generator behaves like a squirrel cage machine, thus sinking reactive current during the fault and possibly worsening the voltage sag [25]

The stator crowbar is composed of bidirectional switches and damping resistors connected in series with the stator [23]. The idea behind the stator crowbar is to increase the stator resistance during the fault, thus providing a passive damping of the stator flux and a better transient response of the system during faults.

A major advantage of this topology is that during crowbar activation, the RSC remains operational, and can assist the flux damping and provide reactive current to the grid, as demanded by the grid codes.

One disadvantage of the stator crowbar approach, are the conduction losses of the bidirectional switches during normal operation, thus special consideration has to be taken when designing the power electronics, for minimizing these losses [23].

## 3.2 System control

Besides adopting the necessary protection devices, the control system of the DFIG has to be properly modified, in order to cope with the eventual grid faults, and to safely ride-trough them, accordingly with the new grid code specifications. A summary of the most important requirements of the DFIG protection devices and the control system have to handle during a fault, was attempted in the first chapter.

In the following the necessary conceptual control system modifications for the RSC, LSC, rotor crowbar and dc chopper, in order to satisfy, at least partially, the fault-ride through requirements, will be presented.

### 3.2.1 Rotor side converter control

The first protection measure regarding the rotor side converter, that can be taken by the control system, is to disable the converter switches when the rotor current magnitude rises above a safety limit. In this manner, the converter IGBTs will be protected from over currents, and the rotor side converter will behave like a passive rectifier.

Figure 3.6 presents this simple control scheme, together with a timer that can simulate the enabling time of the converter, or can be used to prevent re-enabling the RSC too frequently.

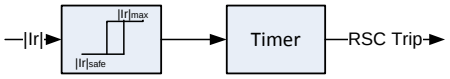


Figure 3.6: RSC over current protection.

Once the rotor currents have reached safe limits and the RSC can be re-enabled, the control system has to regain control of the rotor currents, a difficult task for the RSC, since it has limited power capabilities.

By studying equation (3.2) more closely, from a system control point of view, the disturbances that affect the system can be identified to the three last terms in the equation:

- $j(\omega - \omega_r)\sigma L_r \overrightarrow{i_r}$ the rotor back-e.m.f. or coupling between the dq components of the rotor current
- $j(\omega - \omega_r)\frac{L_m}{L_s}\overrightarrow{\psi_s}$ the stator back-e.m.f., which contains components at the slip frequency, and at the rotor frequency (due to the DC components of the stator flux)
- $\frac{L_m}{L_s}\frac{d\overrightarrow{\psi_s}}{dt}$ a large voltage disturbance due to the fast variation in stator flux

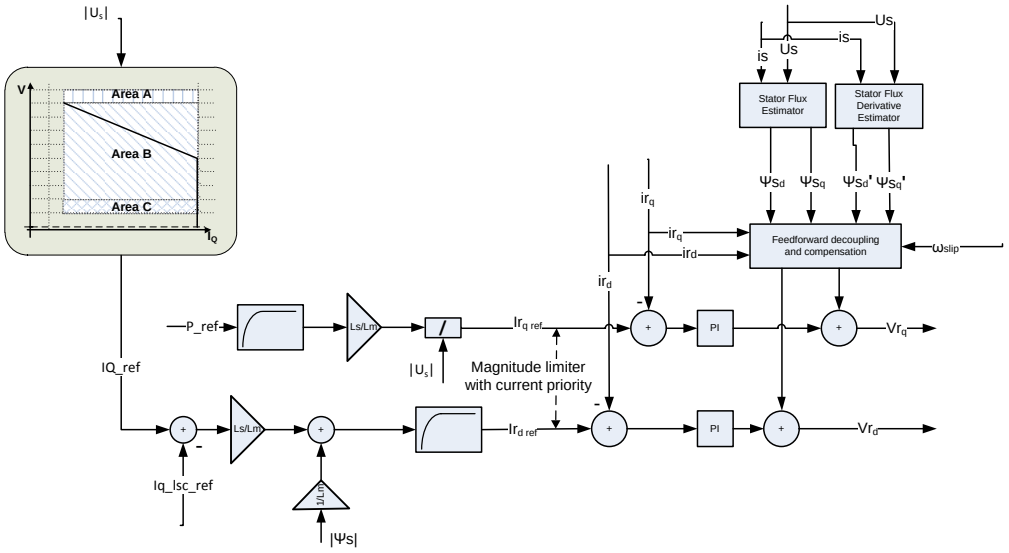


Figure 3.7: RSC fault-ride through modifications concept with full disturbance compensation.

As can be observed from Figure 3.4, the last two components have a significant variation and magnitude, especially the last one, thus special consideration has to be taken when designing the rotor current control.

In order for the RSC to regain and keep control of the rotor currents, these disturbances have to be compensated as fast as possible, and since the $PI$ controllers might not be fast enough, the disturbance has to be estimated and feed-forward compensated, as presented in Figure 3.7.

As will be presented in the next chapters, the rotor current control structure with full disturbance compensation has some important advantages, like fast rotor current limitation during faults, but also some disadvantages, like sustained stator flux oscillations.

In order to alleviate some of the disadvantages of this control structure, some of the fast current limitation capability has been traded for improved stator flux damping and transient response, in the control structure presented in Figure 3.8.

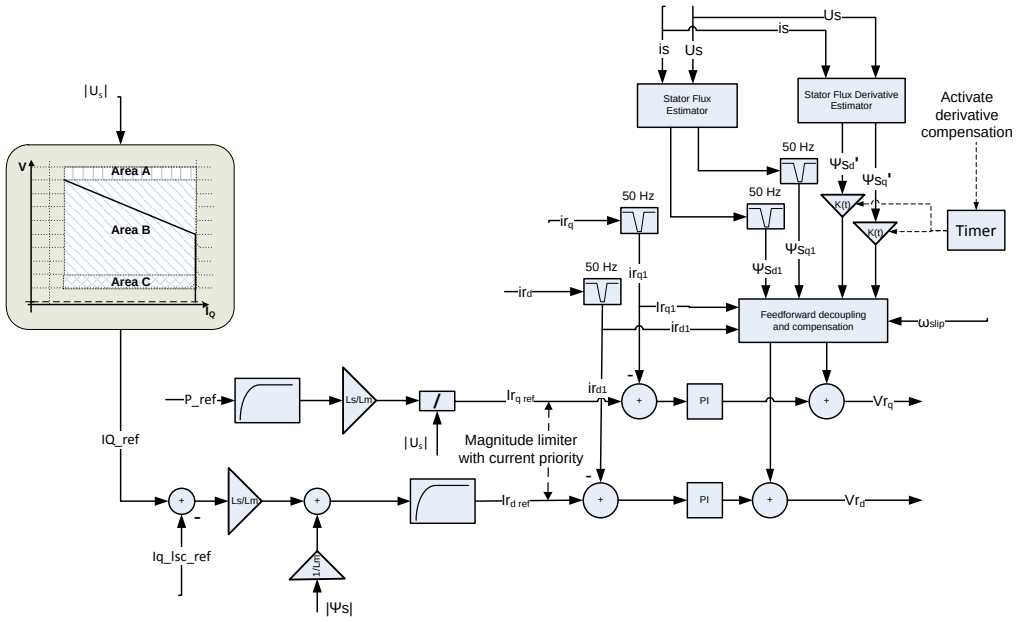


Figure 3.8: RSC fault-ride through modifications concept with partial disturbance compensation and improved flux damping.

This control structure differs from the previous by a slower current controller, designed with 50 Hz notch filters on the current and stator flux signals, also a time-dependent weighting of the feed-forward compensation of the stator flux derivative generated voltage disturbances.

More details regarding the implementation, advantages and disadvantages of these two structures will be presented in the next chapters.

Enhancements of the control structure, some of them presented in [9], are:

- stator flux estimation and feed-forward compensation
- stator flux derivative estimation and feed-forward compensation

- dq axes decoupling
- replacing the power controllers with higher bandwidth low-pass filter in order to increase the response time of the system
- feed-forward the reactive current reference required by the stator winding magnetization
- prescribe the reactive current reference according to the grid code requirements, in correlation with the grid side converter reactive current reference
- implement reactive current priority

### 3.2.2 Grid side converter control

During a grid fault, the LSC has to put less effort into riding through the fault than the RSC, since the control is faster. It's main tasks now are to provide DC-Link voltage control and reactive current support, according to the grid codes. Although if reactive current is prioritized, DC-Link voltage control could be lost, and other protection systems like the dc chopper or crowbar have to take over.

Usually the LSC can be overloaded during grid faults, for short periods of time, to up 50% of the rated DFIG current, as reported in the literature [8, 9]. A simple LSC control concept diagram, based on [9], is presented in Figure 3.9.

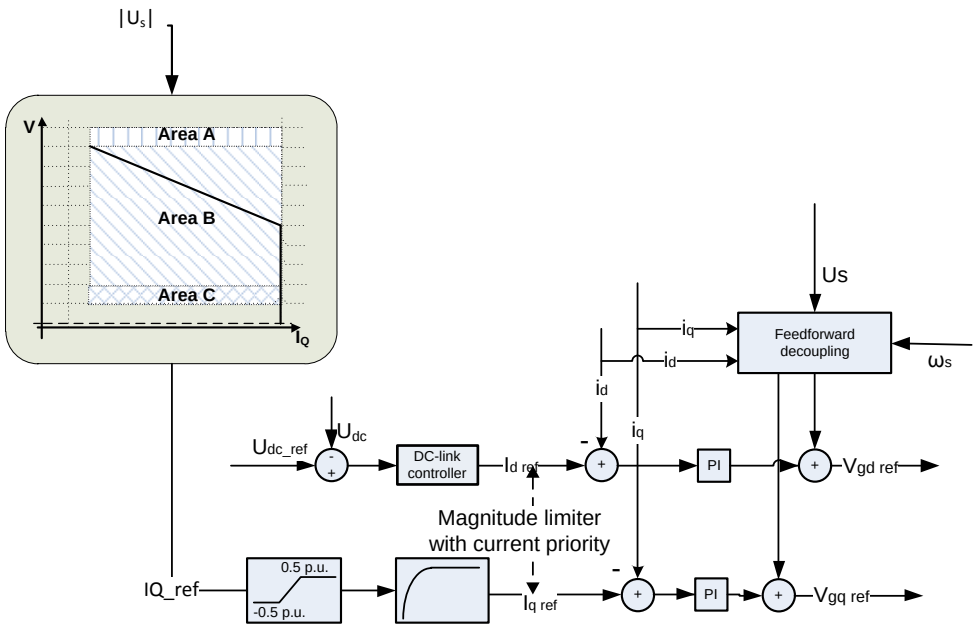


Figure 3.9: LSC fault-ride through modifications concept.

The control structure in Figure 3.9 has the following enhancements implemented:

- feed-forward compensation of the grid voltage
- decoupling of the dq axes
- replacing the reactive power controller with a higher bandwidth low-pass filter in order to increase the response time of the system
- prescribe the reactive current reference according to the grid code requirements
- overload the LSC to up $0.5p.u.$ of rated DFIG current
- implement reactive current priority

### 3.2.3 DC - chopper control

Once the RSC is disabled due to rotor over currents, the converter will behave as a diode bridge and the voltage in the DC-Link will rise very fast, thus possibly damaging the converter. As the LSC will not be able to evacuate the extra energy in the DC-Link capacitor fast enough, a DC chopper can be used to burn the extra power and limit the voltage in the DC-Link [28].

The control employed for the chopper is usually a simple hysteresis controller, as in Figure 3.10, with the DC-Link voltage limit about $1.1-1.2p.u.$, and is dimensioned along with the rating of power converters and the DC-Link [28].

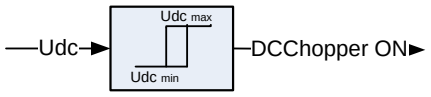


Figure 3.10: DC chopper hysteresis control.

### 3.2.4 Rotor crowbar control

The crowbar can be activated during more severe grid faults, when the RSC cannot regain control of the system, or when the DC chopper cannot limit the DC-Link voltage to safe values. A simple control structure, for an active crowbar, based on the hysteresis controller, is presented in Figure 3.11.

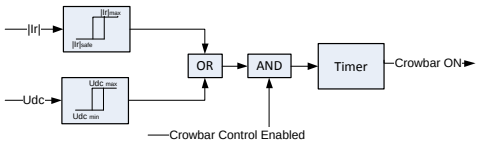


Figure 3.11: Rotor crowbar control concept.

Special consideration has to be taken on the duration the crowbar is active, since control of the DFIG is lost during this period, thus the reactive power support demanded by the grid codes will be delayed, until the crowbar is deactivated and the RSC regains control.

Another aspect that has to be considered when designing the crowbar control, is to avoid a second crowbar firing when the grid voltage recovers, since it could further destabilize the system [7].

### 3.2.5 Stator crowbar control

A simple method for controlling the stator crowbar is to activate it when a voltage dip is detected, maintain it active during the fault and a short while after the voltage recovers, in order to alleviate the second jump in the stator flux.

# Chapter 4

# Modelling and methodology

Compared with the previous two chapters, the present one will describe aspects related to the practical side of the project. The implemented models used for simulations will be analyzed and presented. The parameters used for each building block as well as other implementation details will be shown here.

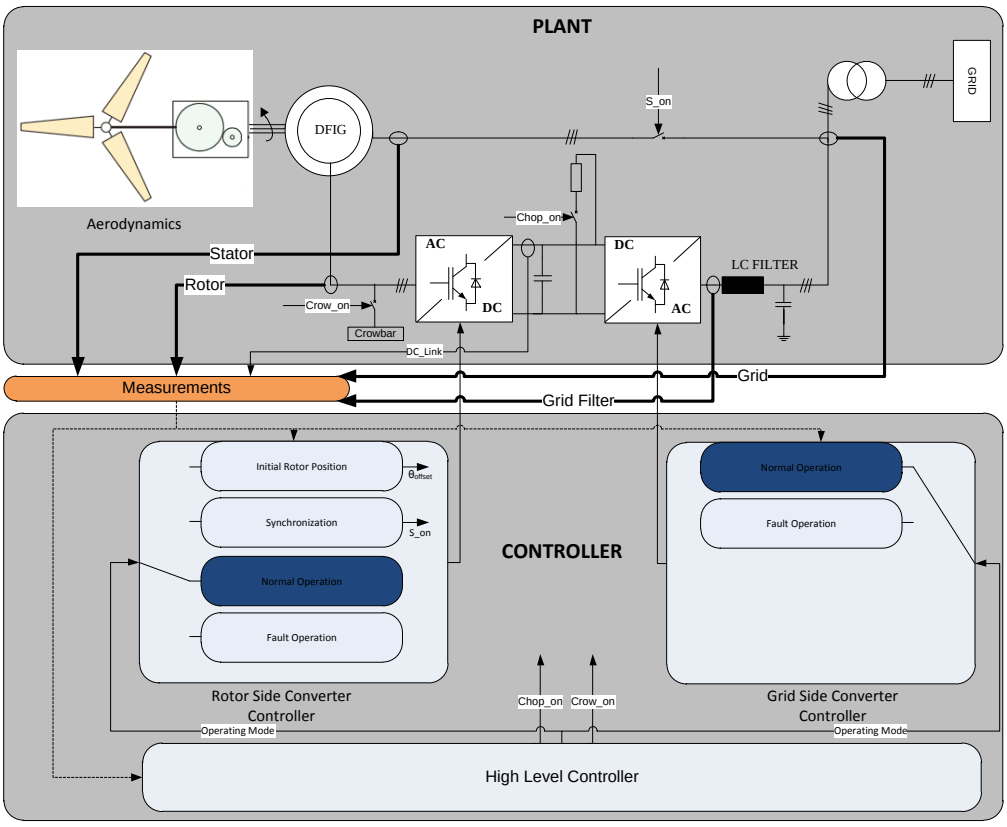


Figure 4.1: Block diagram of the overall modeled plant and controller.

Two main subsystems can be observed in Figure 4.1; the plant and the controller. The plant contains an implementation of the real electro-mechanical system. In this subsystem all the signals are continuous in time, and the building blocks have

been modeled using the PLECS toolbox. The controller subsystem contains all the logic that drives the plant. Here all the signals are discrete in time and the blocks have been implemented using Simulink and Stateflow.

The following two sections, one designated for describing the plant model, and one for the control system provide detailed description of each important subcomponent.

## 4.1 Plant modelling

### 4.1.1 Grid

Since fault ride through operation of the wind turbine was analyzed for this project, a simple voltage source was not enough to model the grid. In order to simulate voltage dips in the grid voltage, a small voltage divider, as presented in Figure 4.2, was implemented in PLECS. The working mechanism is a simple one. After the ratio between the two impedances is calculated so that a certain voltage drop will be achieved, an enable signal is sent to the two switches activating the voltage divider. When the enable signal is turned off, the two switches return to the initial position and the grid voltage recovers to the nominal value.

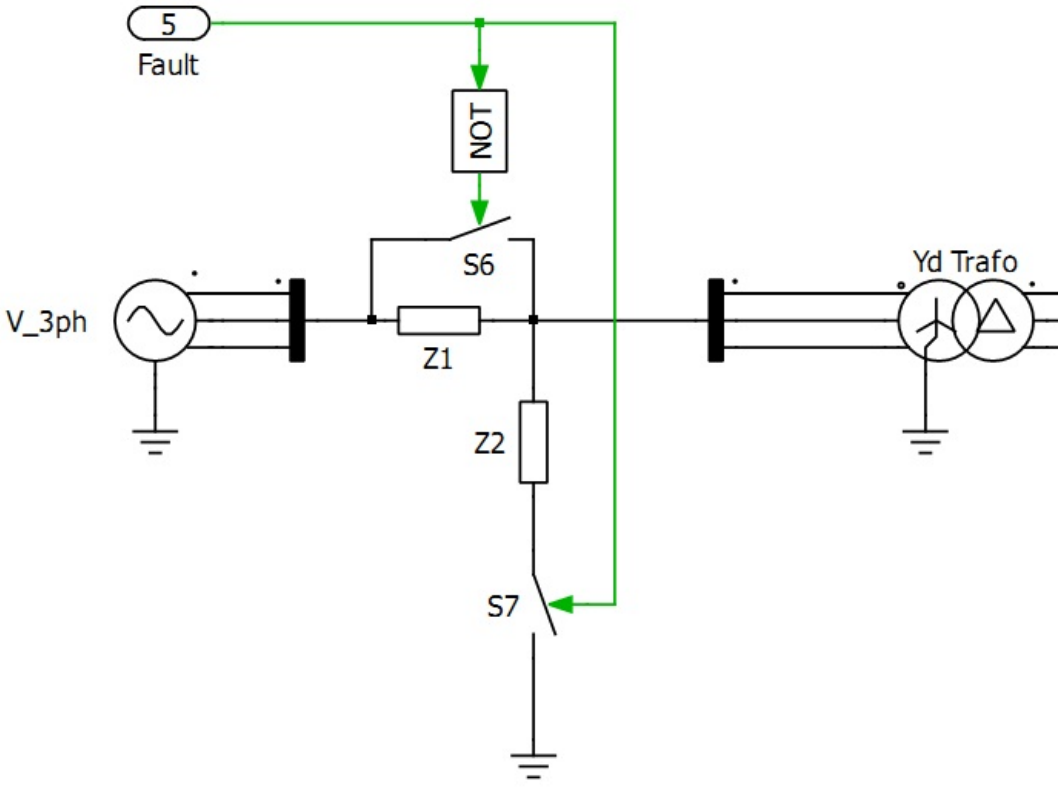


Figure 4.2: PLECS electrical diagram of the grid.

A transformer can also be observed in Figure 4.2. In a real system this transformer is usually a step up transformer that increases the voltage amplitude up to the

transmission level. In the laboratory system that was used for this project, the transformer has a 1:1 transfer ratio and it is used only for isolation and safety reasons. The leakage inductances of the transformer have to be taken into account when designing the control of the grid side controller. The parameters of the transformer used in the laboratory setup can be found in Appendix C.1.

### 4.1.2 Aerodynamics

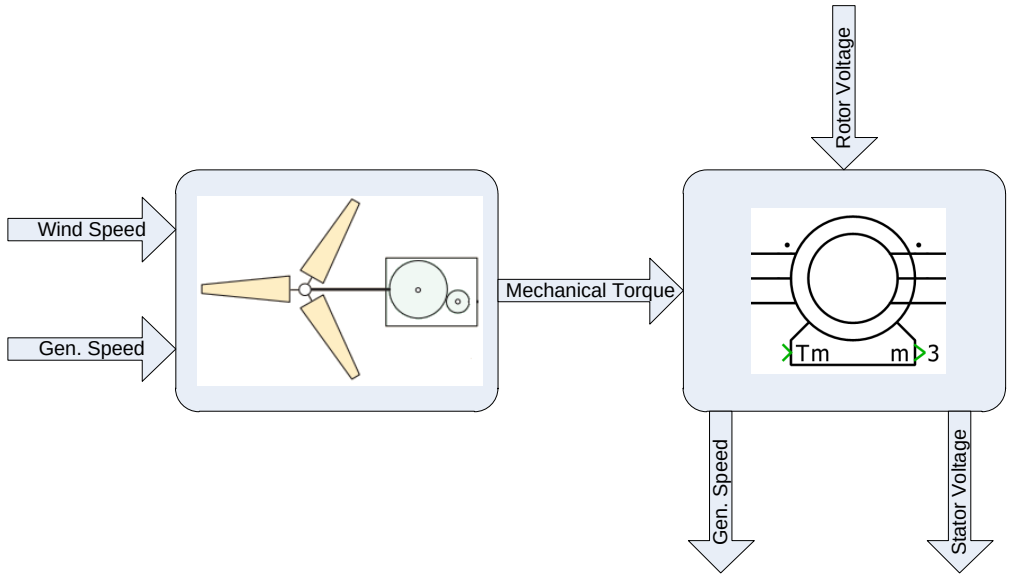


Figure 4.3: Block diagram of interaction between the aerodynamics and the generator subsystem.

The aerodynamic part of the wind turbine was of no interest to the purpose of the current project. However, the DFIG block used in simulations takes as an input the mechanical torque and not the speed. Because of this restriction an extra block, able to prescribe the mechanical torque based on wind speed and generator speed, was needed. A simple implementation based on equations (4.1) already exists in the SimPower Systems toolbox. From simplicity reasons this block was used in the final simulation model.

$$\begin{aligned} P_r &= \tfrac{1}{2}\rho\pi R^2 C_p(\lambda,\beta)V^3 \\ T_m &= \tfrac{P_r}{\omega_r} \end{aligned} \tag{4.1}$$

### 4.1.3 DFIG

The DFIG generator used in the simulation is one of the standard PLECS models. The implementation from Figure 4.4 is based on the generator's equivalent circuit presented in the previous chapter in Figure 2.2. The stator-to-rotor turns ratio

has been implemented as an ideal transformer, on the rotor side of the DFIG, as can be observed from the PLECS schematic.

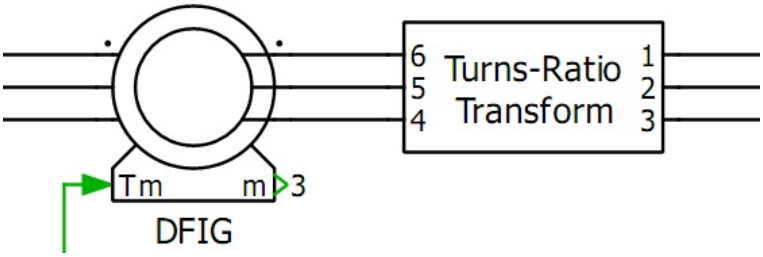


Figure 4.4: PLECS schematic for the DFIG including stator-to-rotor turns ration transformation.

The parameters of the generator used in the laboratory setup, referred to the stator side, can be found in Appendix C.2.

### 4.1.4 Grid filter

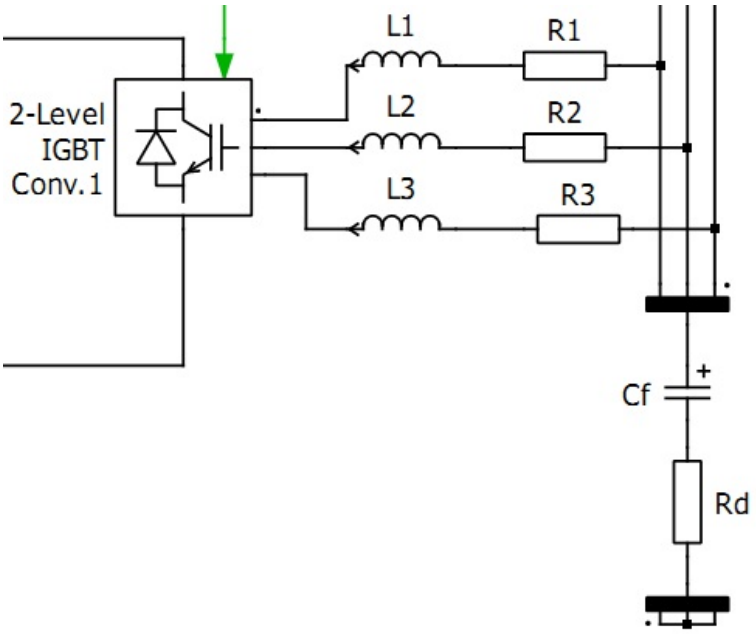


Figure 4.5: PLECS schematic for the grid filter.

From simplicity reasons the grid filter, as well as all the other electrical components of the system, has been modeled using the PLECS toolbox as it can be seen in Figure 4.5. The values used for the laboratory setup components are listed in Appendix C.4.

### 4.1.5 Frequency converters

In order to increase the accuracy of the simulation models both the rotor and the grid side converter were implemented using IGBT based switches as it can be seen in Figure 4.6. The standard configuration of the 2-Level IGBT Converter block, that already exists in the PLECS toolbox, does not allow disabling of the IGBT switches. Since this operation is required in some of the fault ride through strategies presented in the literature, some adjustments had to be performed to this block.

Since the upper transistor of each leg activates when the applied pulse is greater than zero, and the lower one activates when the pulse is smaller than zero it was chosen that a pulse equal to zero will disable that transistor. As the converters are connected to the rotor inductances and to the filter inductances, applying zero signals as pulses will suddenly interrupt an inductive current flow. Such an interruption is not tolerated by PLECS or Simulink and will generate numerical errors during simulation.

In order to avoid this problem, snubbers were mounted in parallel with each transistor as it can be seen in Figure 4.6. This implementation was inspired by the model of a real circuit breaker present in Simulink's SimPower toolbox. The snubber will offer, for a short while, an alternative path for the inductive current at the moment of the switch and thus the simulation will not experiment a sudden jump in inductive current so no errors will be generated.

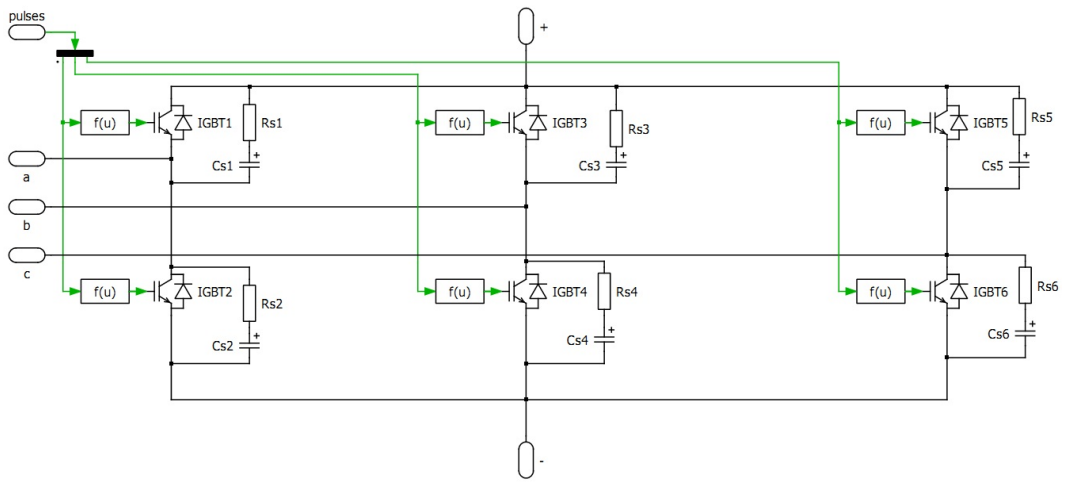


Figure 4.6: PLECS schematic for the frequency converter.

### 4.1.6 Protection devices - DC-Chopper; Crowbar

The protection devices were modeled in PLECS using controlled ideal switches that connect or disconnect a dissipating resistor in the circuit, as can be seen in Figure 4.7. The value used for the DC-Chopper resistance in the laboratory setup can be found in Appendix C.6. Values for the rotor and stator crowbar are

presented only for the full scale system, in Appendix A.6, since no experiments including the rotor or stator crowbar were performed in the laboratory.

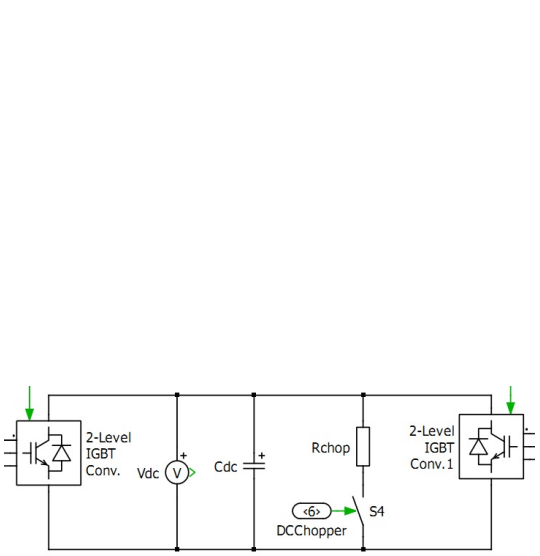


(a) PLECS schematic of the DC-Chopper

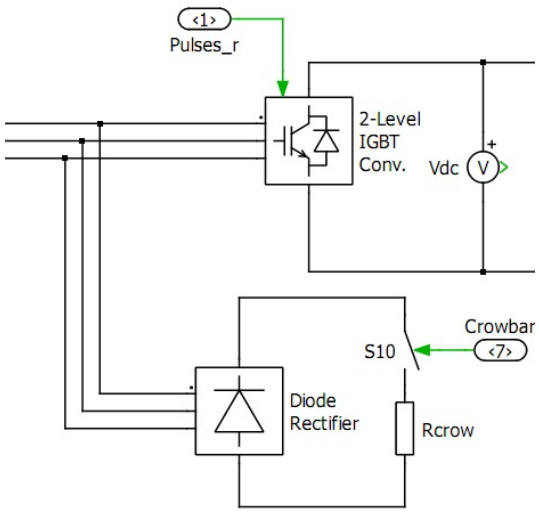


(b) PLECS schematic of the rotor crowbar

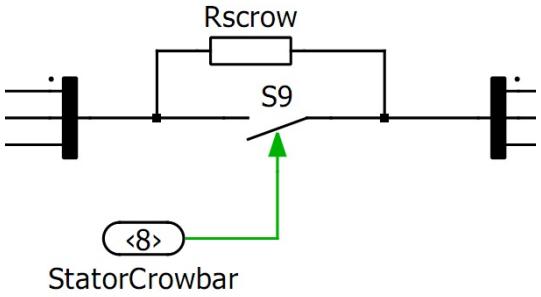


(c) PLECS schematic of the stator crowbar

Figure 4.7: Implemented models for protection devices used for fault ride through operation.

### 4.1.7 Complete plant schematic

The complete PLECS schematic of the DFIG plant, containing the previously described components, is presented in Figure 4.8.

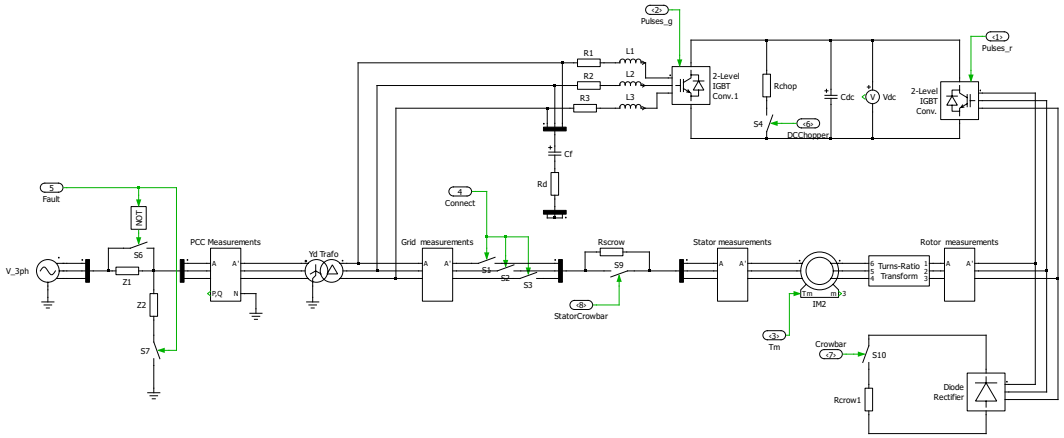


Figure 4.8: Complete PLECS schematic of the plant. A more detailed view of this graph can be seen in Figure A.1.

## 4.2 Control system modelling

The control of doubly fed induction generator based systems is a tedious task. Several aspects, like initial rotor position and synchronization, have to be taken into consideration before reaching normal operation. One of the purposes of this project was to provide a framework where all these prerequisites and operating modes are included in a single control schematic, as presented in Figure 4.1. In order to achieve this, different operating modes for the rotor and grid side converter controller have been defined. A *High Level Controller* that dictates the operating mode for the two converters has also been developed in order to complete the schematic and to provide a structured hierarchical control.

The next two subsections describe the control challenges and strategies applied in the different operating modes of the system, while the last one explains the role and the implementation for the *High Level Controller*.

### 4.2.1 Rotor side converter controller

As it can be seen in Figure 4.1 four operating modes have been identified for the rotor side controller, namely: *Initial Rotor Position*, *Synchronization*, *Normal operation* and *Fault operation*. Since different task sequence have to be followed for each operating mode, and different control structures have to be employed, it was decided to implement this controller as an *S-function* block. This method was preferred to the one that involves standard *Simulink* blocks from reasons related to compactness and readability. Also, parameter handling and sequential logic is easier to implement using C programming compared with standard *Simulink* blocks.

In the following the theoretical background for the four operating modes will be explained, together with basic equations for designing the controllers and their

implementation in the *Simulink* environment.

### Initial rotor position estimation

As it will be observed in the following sections, the rotor electrical position is an important quantity when looking at different control schemes. It has to be noted that an incremental encoder will only provide a measure of the relative angle rotated with respect to an initial position of the rotor, $\theta_{ri}$ [11]. This means that the electrical angle value obtained by the means of the encoder will only equal the actual position of the rotor and will be always shifted with the initial position. In order to compensate for this, prior to launching any control process, it is necessary to identify the *initial rotor position* $\theta_{ri}$; from this point onward the value provided by the encoder will just be added to this value.

As presented in [11], getting the initial rotor position when the DFIG stator is disconnected from the grid is not a difficult task. It is sufficient to feed the rotor with a three-phase balanced voltage and to measure the induced currents in the rotor and the voltages in the stator at steady state. After having these values the initial rotor position can be estimated as shown in equation (4.2).

$$\theta_{ri} = arctan(\frac{v_{s\beta}}{v_{s\alpha}}) - 90^o - arctan(\frac{i_{rq}}{i_{rd}}) \tag{4.2}$$

### Synchronization operating mode

In the synchronization operation mode there is no power exchange between the DFIG stator and the grid, the main task of the rotor converter controller is to synchronize the stator voltage with the grid voltage phase and amplitude.

**Synchronization rotor current controllers** In order to design the synchronization controller, the basic DFIG equations from (2.8, 2.9), have to be rewritten in the stator/grid flux reference frame, previously presented, and denoted by "e". This task can be achieved by setting $\omega = \omega_e$ (rotational frequency of the stator/grid flux obtained by means of PLL), and by making use of the fact that there is no power exchange during the synchronization phase, $\overrightarrow{i_s} = 0$. The resulting equations are presented in (4.3, 4.4).

$$\begin{aligned} v_{sd}^e &= L_m \frac{di_{rd}^e}{dt} - \omega_e L_m i_{rq}^e \\ v_{sq}^e &= L_m \frac{di_{rq}^e}{dt} + \omega_e L_m i_{rd}^e \end{aligned} \tag{4.3}$$

$$\begin{aligned} v_{rd}^e &= R_r i_{rd}^e + L_r \frac{di_{rd}^e}{dt} - (\omega_e - \omega_r) L_r i_{rq}^e \\ v_{rq}^e &= R_r i_{rq}^e + L_r \frac{di_{rq}^e}{dt} + (\omega_e - \omega_r) L_r i_{rd}^e \end{aligned} \tag{4.4}$$

Synchronization demands that in terms of space-phasors, $\overrightarrow{v_s} = \overrightarrow{v_{grid}}$. This means that the voltage induced in the open stator matches the voltage of the grid. Considering $\overrightarrow{v_{grid}}$ aligned with the q-axis, the voltage-matching requirement can be expressed as formulated in equation (4.5) [11].

$$v_{sd}^e = 0 \quad v_{sq}^e = |\overrightarrow{v_{grid}}| \tag{4.5}$$

Inspecting equation (4.3), it can be inferred that under steady-state conditions equation (4.5) is fulfilled if the $d$ and $q$ components of the rotor current reach the values pointed out in (4.6). This yields that the synchronization task can be viewed as a problem of regulating the rotor current components at the set points displayed in equation (4.6) [11].

$$i_{rd}^e = \frac{\overrightarrow{v_{grid}}}{\omega_s L_m} \quad i_{rq}^e = 0 \tag{4.6}$$

The design of the rotor current controllers begins from the rotor voltage equations in (4.4), by separating the linear terms from the nonlinear ones, as in (4.7), where ${v_{rd}^e}'$ and ${v_{rq}^e}'$ represent the linear dynamics of the system, for which PI controllers will be design, and ${v_{rd}^e}^{decouple}$ and ${v_{rq}^e}^{decouple}$ represent the coupling between the $dq$ axes and will be feed-forward compensated.

$$\begin{aligned}
&{v_{rd}^e}' = R_r i_{rd}^e + L_r \tfrac{di_{rd}^e}{dt} \\
&{v_{rq}^e}' = R_r i_{rq}^e + L_r \tfrac{di_{rq}^e}{dt} \\
&{v_{rd}^e}^{decouple} = -(\omega_s - \omega_r) L_r i_{rq}^e \\
&{v_{rq}^e}^{decouple} = (\omega_s - \omega_r) L_r i_{rd}^e \\
&{v_{rd}^e}^* = {v_{rd}^e}' + {v_{rd}^e}^{decouple} \\
&{v_{rq}^e}^* = {v_{rq}^e}' + {v_{rq}^e}^{decouple}
\end{aligned} \tag{4.7}$$

In order to design a discrete PI current controller for the synchronization mode the linear dynamics of the system are first expressed in the Laplace domain as a linear transfer function (4.8). This continuous time transfer function is further discretized with the sampling period $Ts$, including the *zero-order hold* effect of the A/D sampling and the inverter PWM dead-time as *one sample delay*, as presented in (4.9).

$$G_{syn}(s) = \frac{I_{rd}^e(s)}{V_{rd}^e{}'(s)} = \frac{I_{rq}^e(s)}{V_{rq}^e{}'(s)} = \frac{1/R_r}{1 + (L_r/R_r)s} \tag{4.8}$$

$$G_{syn}(z) = \frac{1}{z}\mathbb{Z}\left\{\frac{1 - e^{sT_s}}{s} G_{syn}(s)\right\} = \frac{z-1}{z^2}\mathbb{Z}\left\{\frac{G_{syn}(s)}{s}\right\} \tag{4.9}$$

The tuning of the discrete PI synchronization controller defined in (4.10) has been carried out using *Matlab SISO Tool*, by imposing the bandwidth, phase and gain margins with an acceptable overshoot, as can be observed from the controller design plots from Figure 4.9. The resulting parameters of the PI controller are presented in Appendix B

$$C_{syn}(z) = Ki\frac{T_s}{z-1} + Kp \tag{4.10}$$

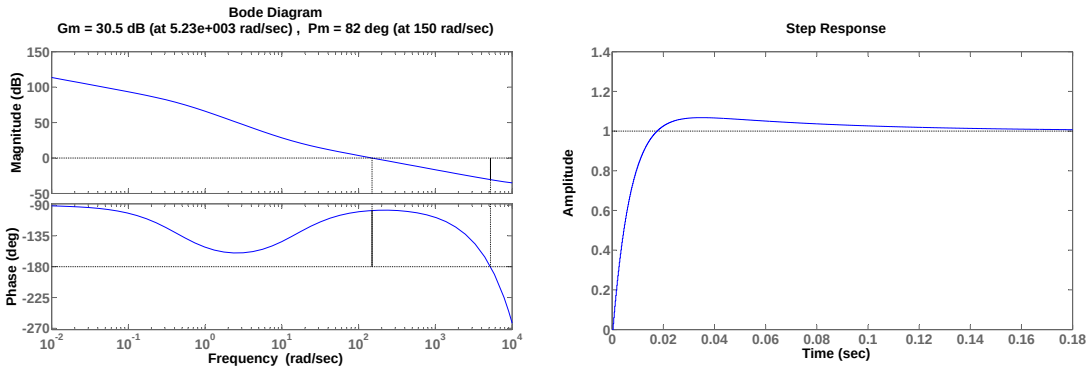


(a) Phase and gain margins of the open loop system

(b) Step response of the closed loop system

Figure 4.9: Frequency and time domain synchronization controller design plots.

Since the rotor current controller has a variable structure and parameters, depending on the operation mode of the DFIG, it has been implemented as an *S-function*, listed in Appendix E, and implemented in *Simulink* as presented in Figure 4.10. The $C_{syn}(z)$ PI controller is implemented inside this *S-function*, alongside with the feed-forward compensation terms, and its activation is controlled by the *RSCMode* input, which is controlled by the *High Level Controller*.

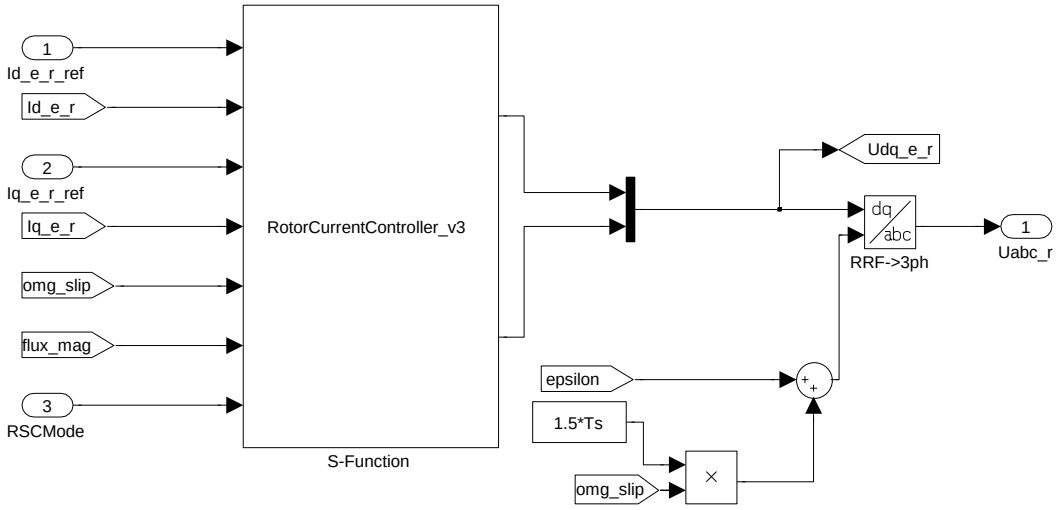


Figure 4.10: Variable structure rotor side converter current controller implementation.

### Normal operating mode

In normal operation the role of the rotor side converter is to provide control of the active and reactive power exchanged between the DFIG stator and the grid. This is achieved by use of cascaded controllers, composed of an inner (faster) rotor current control loop and an outer (slower) power controller, as previously presented in the conceptual diagram from Figure 2.5.

**Rotor current controllers** The rotor current controller in normal operation mode is designed by rewriting the basic DFIG equations from (2.8, 2.9) in the stator/grid flux reference frame, previously presented in Figure 2.4 and denoted by "e", similar to the synchronization mode. However, this time the stator current is non-zero. The resulting equations are presented in (4.11):

$$\begin{aligned} v_{dr}^e &= R_r i_{dr}^e + \sigma L_r \frac{di_{dr}^e}{dt} - \omega_{slip}\left(\sigma L_r i_{qr}^e + \frac{L_m}{L_s}\psi_{qs}^e\right) + \frac{L_m}{L_s}\frac{d\psi_{ds}^e}{dt} \\ v_{qr}^e &= R_r i_{qr}^e + \sigma L_r \frac{di_{qr}^e}{dt} + \omega_{slip}\left(\frac{L_m}{L_s}\psi_{ds}^e + \sigma L_r i_{dr}^e\right) + \frac{L_m}{L_s}\frac{d\psi_{qs}^e}{dt} \end{aligned} \tag{4.11}$$

where the slip angular frequency $\omega_{slip}$ and the total leakage factor $\sigma$ are:

$$\begin{aligned} \omega_{slip} &= \omega_e - \omega_r \\ \sigma &= 1 - \frac{{L_m}^2}{L_s} \end{aligned} \tag{4.12}$$

During normal operation, the system can be considered to be in steady state, thus the stator flux derivative terms can be neglected. Furthermore, by separating the linear and nonlinear terms we get the rotor converter reference voltages (4.13). Here ${v_{rd}^e}'$ and ${v_{rq}^e}'$ represent the linear dynamics of the system, for which PI controllers will be designed, and $v_{rd}^{e\ decouple}$ and $v_{rq}^{e\ decouple}$ represent the coupling between the *dq* axes, and will be feed-forward compensated.

$$\begin{aligned} {v_{rd}^e}' &= R_r i_{dr}^e + \sigma L_r \frac{di_{dr}^e}{dt} \\ {v_{rq}^e}' &= R_r i_{dr}^e + \sigma L_r \frac{di_{qr}^e}{dt} \\ v_{rd}^{e\ decouple} &= -\omega_{slip}\left(\sigma L_r i_{qr}^e + \frac{L_m}{L_s}\psi_{qs}^e\right) \\ v_{rq}^{e\ decouple} &= \omega_{slip}\left(\sigma L_r i_{dr}^e + \frac{L_m}{L_s}\psi_{ds}^e\right) \\ {v_{rd}^e}^* &= {v_{rd}^e}' + v_{rd}^{e\ decouple} \\ {v_{rq}^e}^* &= {v_{rq}^e}' + v_{rq}^{e\ decouple} \end{aligned} \tag{4.13}$$

Similar to the synchronization mode, the design of the discrete PI current controller in the normal operation mode starts by writing the plant dynamics in the Laplace domain, as in (4.14). This continuous time transfer function is further discretized with the sampling period $Ts$, including the *zero-order hold* effect of the A/D sampling and the inverter PWM dead-time as *one sample delay*, as presented in (4.15)

$$G_{rot}(s) = \frac{I_{rd}^e(s)}{V_{rd}^{e\prime}(s)} = \frac{I_{rq}^e(s)}{V_{rq}^{e\prime}(s)} = \frac{1/R_r}{1 + (\sigma L_r/R_r)s} \tag{4.14}$$

$$G_{rot}(z) = \frac{1}{z}\mathbb{Z}\left\{\frac{1 - e^{sT_s}}{s}G_{rot}(s)\right\} = \frac{z-1}{z^2}\mathbb{Z}\left\{\frac{G_{rot}(s)}{s}\right\} \tag{4.15}$$

The tuning of the discrete PI synchronization controller in (4.16) has been carried out in a similar manner as the synchronization controller. The afferent Bode and step response design plots are presented in Figure 4.11. It can be observed that large gain and phase margins have been imposed, this translates into increased relative stability of the closed loop system, this is important if the system parameters vary with time, or if they are not identified accurately.

$$C_{rot}(z) = Ki\frac{T_s}{z-1} + Kp \tag{4.16}$$

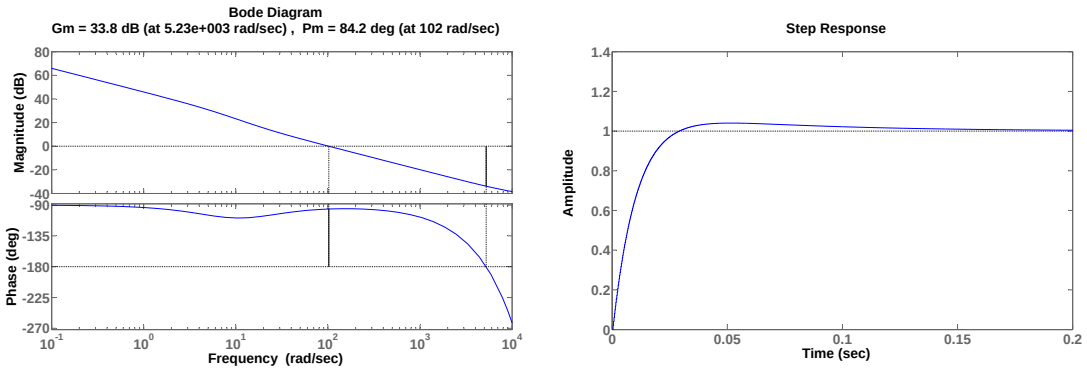


(a) Phase and gain margins of the open loop system

(b) Step response of the closed loop system

Figure 4.11: Frequency and time domain rotor current controller design plots.

The bandwidth of the rotor current controller has been chosen to be lower than for the grid side converter, this is appropriate taking into consideration the large time constants of the DFIG and the normal operation requirements. The resulting controller parameters can be found in Appendix B.

The normal operation rotor side current controller was implemented in the same *S-function* as the synchronization controller, listed in Appendix E, and presented in Figure 4.10. The $C_{rot}(z)$ PI controller and corresponding feed-forward decoupling terms, are activated in normal operation by the *High Level Controller*, through the *RSCMode* input.

**Stator power controllers** The stator power controllers are designed by writing the stator power equations in terms of the rotor currents, in the stator/grid flux reference as in equation (4.17) [13].

$$\begin{aligned} P_s &= -\frac{3}{2}\frac{V_s L_m}{L_s} i_{qr}^e \\ Q_s &= \frac{3}{2}\frac{V_s}{L_s}\psi_s^e - \frac{3}{2}\frac{V_s L_m}{L_s} i_{dr}^e \end{aligned} \tag{4.17}$$

If the rotor current controllers are much faster in comparison with the desired bandwidth of the power controllers, the current control dynamics can be neglected in the design process of the power controllers.

Alternatively, the closed loop dynamics of the rotor current controllers can be calculated as in (4.18), the plant dynamics for the power controllers resulting as (4.19).

$$G_{rot\_cl}(z) = \frac{C_{rot}(z)G_{rot}(z)}{1 + C_{rot}(z)G_{rot}(z)} \tag{4.18}$$

$$G_{rot\_pq}(z) = \frac{V_{dqr}^e(z)}{P_s(z)} = \frac{V_{dqr}^e(z)}{Q_s(z)} = -\frac{3}{2}\frac{V_s L_m}{L_s} G_{rot\_cl}(z) \tag{4.19}$$

The stator active and reactive power controllers $C_{rot\_pq}(z)$, have been tuned in a similar fashion with the *Matlab SISO Tool*. The associated stator power controller design plots are displayed in Figure 4.12. As can be observed, the relative stability

margins of the system are maintained, only the bandwidth of the power controllers is lower, as it is normal for a cascaded loop control system. The resulting parameters are presented in Appendix B.

$$C_{rot\_pq}(z) = Ki\frac{T_s}{z-1} + Kp \tag{4.20}$$

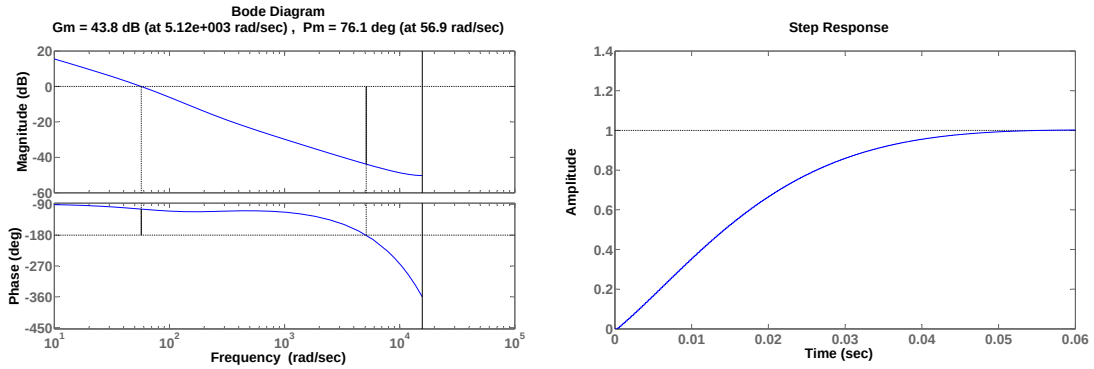


(a) Phase and gain margins of the open loop system

(b) Step response of the closed loop system

Figure 4.12: Frequency and time domain stator power controller design plots.

The overall control structure implementation of the rotor side converter, including the rotor current and stator power controllers, in normal operation, is presented in Figure 4.13.

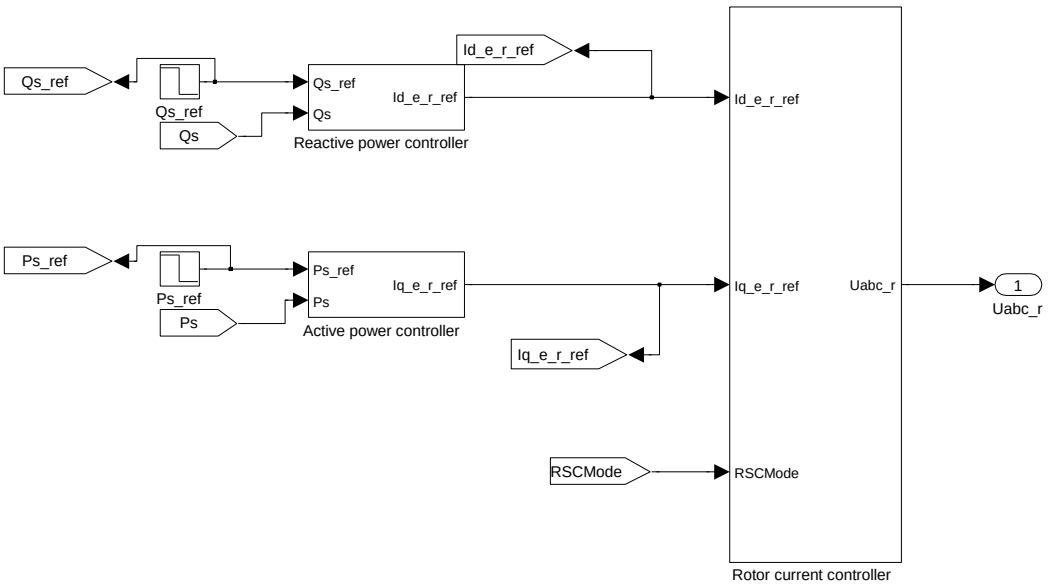


Figure 4.13: Rotor side converter control structure in normal operation.

### Fault operating mode

Two possible solutions for controlling the rotor side converter during symmetrical voltage sags have been proposed in Chapter 3, and will be further detailed next.

**Full disturbance compensation strategy** The concept behind this strategy was presented in Figure 3.7, and it is based on the idea to estimate and feed-forward compensate all the voltage disturbances that are induced in the rotor winding.

$$\overrightarrow{v_r} = R_r \overrightarrow{i_r} + \sigma L_r \frac{d\overrightarrow{i_r}}{dt} + \frac{L_m}{L_s}\frac{d\overrightarrow{\psi_s}}{dt} + j(\omega - \omega_r)\sigma L_r \overrightarrow{i_r} + j(\omega - \omega_r)\frac{L_m}{L_s}\overrightarrow{\psi_s} \tag{4.21}$$

By rewriting the general rotor voltage equation (4.21), in terms of rotor currents and stator flux, these voltage disturbance can be identified and categorized into two groups:

- rotor flux induced back-e.m.f., represented by the $j(\omega - \omega_r)\sigma L_r \overrightarrow{i_r}$ term
- stator flux induced back-e.m.f., represented by the $j(\omega - \omega_r)\frac{L_m}{L_s}\overrightarrow{\psi_s}$ and $\frac{L_m}{L_s}\frac{d\overrightarrow{\psi_s}}{dt}$ terms

The rotor flux induced disturbance is simply estimated from the measured rotor currents. The stator flux vector can be estimated from the measured stator and rotor currents, as in (4.22), if accurate machine model parameters are available.

$$\overrightarrow{\psi_s} = L_s \overrightarrow{i_s} + L_m \overrightarrow{i_r} \tag{4.22}$$

Last but not least, the most severe voltage disturbance induced in the rotor winding is created by the stator flux derivative components, thus an accurate estimation of the derivative is required. This can be achieved by estimating the stator flux derivative from the electrical model of the DFIG, instead of simply differentiating the stator flux.

By rewriting the stator voltage equation, in the *stationary reference frame* ($\omega = 0$), the stator flux derivative vector can be calculated from the stator currents and voltage measurements as in (4.23).

$$\frac{d\overrightarrow{\psi_s}}{dt} = \overrightarrow{v_s} - R_s \overrightarrow{i_s} \tag{4.23}$$

The main advantage of this method is that a fast rotor current limitation can be achieved through the fast feed-forward compensation. This limitation would not be possible using only the slow PI controller. With the fast current limitation, the rotor currents will be damped. Using this strategy the rotor converter control will be maintained in most of the cases as compared to other fault ride-through strategies that coast the rotor converter as result of over-currents.

There are some important drawbacks regarding this strategy that need to be pointed out. One is that the rotor converter could be saturated by the fast feed-forward compensation terms. Furthermore, as will be observed from the presented simulation cases, the stator flux DC components are sustained, and unbalanced components are introduced into the DC-Link voltage creating significant ripple.

**Partial disturbance compensation with improved flux damping strategy**
This strategy was developed in order to overcome some of the shortcomings of the previous strategy, and to reach an acceptable compromise between fast rotor current limitation and stator flux damping/DC-Link voltage stability.

The concept behind the strategy was presented in Figure 3.8, in the previous chapter, and consists of two major ideas:

- the rotor current controller should only regulate the positive sequence component of the rotor currents
- the severe voltage disturbance introduced by the derivative of the stator flux should be feed-forward compensated at the beginning and at the end of the fault, for a short duration, so that rotor current control can be maintained

The first idea can be implemented by extracting the positive sequence of the rotor currents. In the restricted case, when only symmetrical voltage sags are studied, it is enough to filter out the 50 Hz components of the rotor currents and stator flux in the synchronous reference frame.

Is it also necessary to redesign the current controllers, to take into consideration the dynamics of the 50 Hz notch filters on the current feedback paths. It has to be noted that by introducing the 50Hz notch filters into the control system, the upper bandwidth of the rotor current controller should be below 50 Hz, otherwise the stability and the dynamic response of the closed loop system will be negatively affected by the notch filter dynamics.

The second idea consists of weighting the stator flux derivative compensation term, as in (4.24), where $K(t)$ is a function of the voltage dip and activation time.

$$K(t)\frac{L_m}{L_s}\frac{d\overrightarrow{\psi_s}}{dt} \tag{4.24}$$

Other modifications to the control structure of the rotor side converter, as described in the previous chapter, are to replace the power controllers with low-pass filters. This is used in order to improve the response time and stability of the system and to implement a smart ramping of the active and reactive stator currents, dependent on voltage dip and grid code requirements.

The modified *Simulink* implementation of the rotor side converter control structure is presented Figure 4.14.

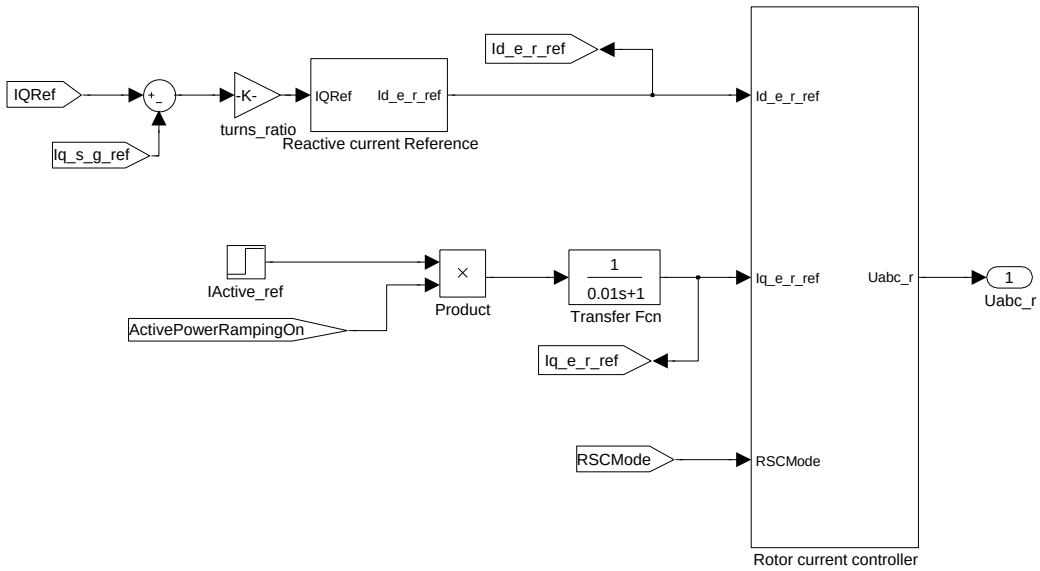


Figure 4.14: Rotor side converter control structure modified for fault ride through.

The stator reactive current reference calculation block is presented in Figure 4.15, where $IQRef$ is the reactive current reference required by the grid code, from which the reactive current provided by the grid side converter is subtracted.

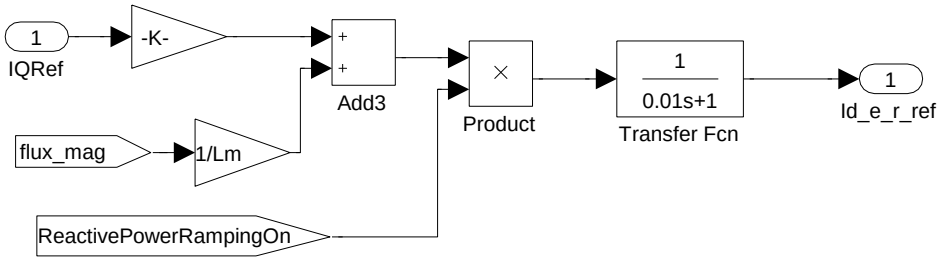


Figure 4.15: Stator reactive current reference calculation.

### 4.2.2 Grid side converter controller

Control of the grid side converter is less complex than its rotor side converter counterpart. As can be observed from Figure 4.1 only two operating modes have been identified for the grid side controller, namely:*Normal operation* and *Fault operation.*

These operating modes differ only from the tasks the grid side control has to achieve during normal or fault operation, the internal structure of the controller remaining the same.

In the following, the basic equation for designing the grid side converter controllers will be presented, along with a *Simulink* implementation.

### Normal operating mode

The operating concept of the grid side converter controller, presented in Chapter 2 and in the Figure 2.7, is that of a cascaded controller with two control loops, the inner grid filter current controllers, and the outer DC-Link voltage and reactive power controllers, similar to the rotor side controller concept.

**Grid filter current controllers** The first step in designing the grid side converter controller is to design the inner current control loops by starting from the basic grid filter equations from (2.11). These equations are rewritten in the *grid voltage reference frame*, previously presented in Figure 2.6 and denoted by "gv", by setting $\omega = \omega_s$ (rotational frequency of the grid voltage), thus resulting in equation (4.25).

$$\begin{aligned} v_{sd}^{gv} &= R_f i_{fd}^{gv} + L_f \frac{di_{fd}^{gv}}{dt} - \omega_s L_f i_{fq}^{gv} + v_{id}^{gv} \\ v_{sq}^{gv} &= R_f i_{fq}^{gv} + L_f \frac{di_{fq}^{gv}}{dt} + \omega_s L_f i_{fd}^{gv} + v_{iq}^{gv} \end{aligned} \tag{4.25}$$

Similar with the rotor side controller case, the linear dynamics of the system, $v_{id}^{gv\prime}$ and $v_{iq}^{gv\prime}$, are separated from the coupling terms between the $dq$ axes, $v_{id}^{gvdecouple}$ and $v_{iq}^{gvdecouple}$, which will be used for feed-forward compensation. Finally resulting in the grid inverter reference voltages, $v_{id}^{gv*}$ and $v_{iq}^{gv*}$, as calculated in (4.26).

$$\begin{aligned} v_{id}^{gv\prime} &= R_f i_{fd}^{gv} + L_f \frac{di_{fd}^{gv}}{dt} \\ v_{iq}^{gv\prime} &= R_f i_{fq}^{gv} + L_f \frac{di_{fq}^{gv}}{dt} \\ v_{id}^{gvdecouple} &= \omega_s L_f i_{sq}^{gv} + v_{sd}^{gv} \\ v_{iq}^{gvdecouple} &= -\omega_s L_f i_{sd}^{gv} + v_{sq}^{gv} \\ v_{id}^{gv*} &= -v_{id}^{gv\prime} + v_{id}^{gvdecouple} \\ v_{iq}^{gv*} &= -v_{iq}^{gv\prime} + v_{iq}^{gvdecouple} \end{aligned} \tag{4.26}$$

The simplified continuous transfer function of the grid filter is obtained from the linear dynamics of the grid filter voltage equations as in (4.27). It can be observed that the capacitor component of the LCL filter has been ignored in the grid filter voltage equations. This simplification is possible due to the fact that the capacitor is damped, and in the present case its dynamics can be neglected.

$$G_{filt}(s) = \frac{I_f^{gv}(s)}{V_i^{gv}(s)} = \frac{1}{L_f s + R_f} \tag{4.27}$$

The continuous time transfer function of the grid filter is further discretized with the sampling period $Ts$, including the *zero-order hold* effect of the A/D sampling and the inverter PWM dead-time as *one sample delay* as presented in (4.36)

$$G_{filt}(z) = \frac{1}{z}\mathbb{Z}\left\{\frac{1-e^{sT_s}}{s} G_{filt}(s)\right\} = \frac{z-1}{z^2}\mathbb{Z}\left\{\frac{G_{filt}(s)}{s}\right\} \tag{4.28}$$

Based on the plant transfer function $G_{filt}(z)$, the PI current controller presented in equation (4.29) has been tuned with the *Matlab SISO tool*. From the design plots presented in Figure 4.16 it can be observed that the bandwidth of the controllers is

large, compared to the rotor side controllers, this is necessary since a fast DC-Link voltage controller with good disturbance rejection needs to be designed on top of the current controllers. The large controller bandwidth is also possible since the small grid filter time constants allows it. The resulting controller parameters are presented in Appendix B.

$$C_{filt}(z) = Ki\frac{T_s}{z-1} + Kp \tag{4.29}$$

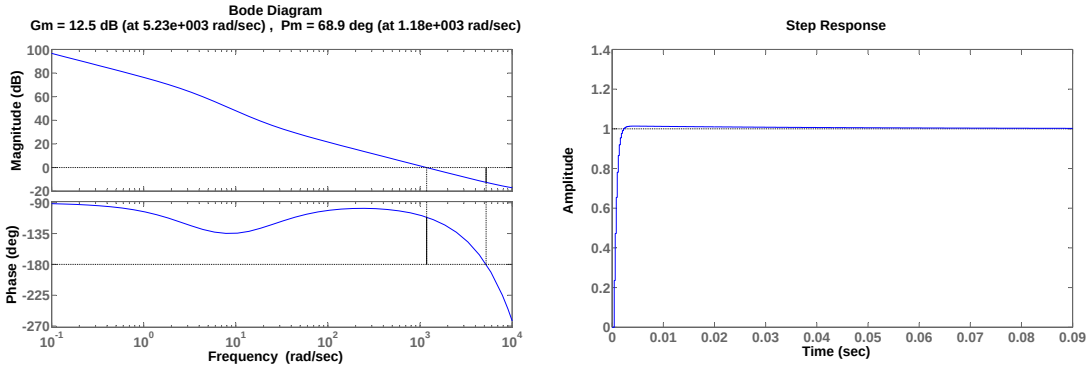


(a) Phase and gain margins of the open loop system

(b) Step response of the closed loop system

Figure 4.16: Frequency and time domain grid filter current controller design plots.

The *Simulink* implementation of these controllers is presented in Figure 4.17.

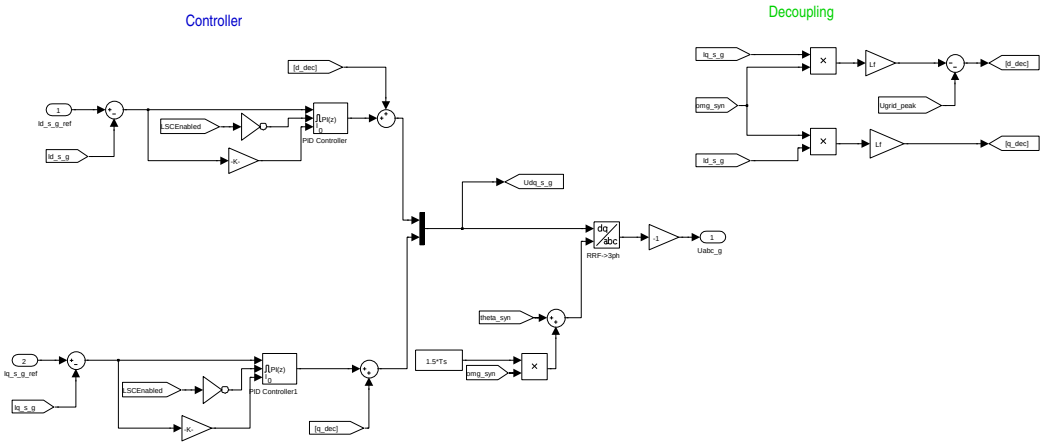


Figure 4.17: Simulink implementation of the grid side converter current controllers.

**DC-Link voltage controller** Once the current controllers are designed, the DC-Link voltage control design can commence by first writing the equation of the energy stored in the DC-Link capacitor, as in (4.30).

$$W_{dc} = \frac{1}{2}C_{dc}v_{dc}^2 \tag{4.30}$$

The variation of energy in the capacitor is dependent on the power delivered to the grid filter, $P_g$, and the power delivered to the rotor circuit, $P_r$ [22].

$$\frac{dW_{dc}}{dt} = \frac{1}{2}C_{dc}\frac{dv_{dc}^2}{dt} = P_g - P_r \tag{4.31}$$

this yields the variation of the DC-Link voltage as presented in equation (4.32):

$$C_{dc}v_{dc}\frac{dv_{dc}}{dt} = P_g - P_r \tag{4.32}$$

The condition for $v_{dc}$ to be constant is that $P_g = P_r$. Expressing the active power $P_g$ in terms of $dq$ components, in the *grid voltage oriented reference frame*, as in (4.33), one can see that the current $i_{fd}^{gv}$ is used in controlling the DC-Link voltage.

$$P_g = \frac{3}{2}v_{sd}^{gv}i_{fd}^{gv} \tag{4.33}$$

As it can be observed from equation (4.33) and equation (4.32), the relation between $v_{dc}$ and $i_fd$ is nonlinear. A way of simplifying the control is to utilize feedback linearization, where the nonlinear dynamics of the DC-Link are transformed into an equivalent linear model. This is done by choosing $W_{dc} = v_{dc}^2$ as the controlled variable instead of $v_{dc}$. In this way the voltage control is achieved by controlling the energy flowing in and out of the capacitor [22]. The resulted model is given in equation (4.34).

$$\frac{1}{2}C_{dc}\frac{dW_{dc}}{dt} = \frac{3}{2}v_{sd}^{gv}i_{fd}^{gv} - P_r \tag{4.34}$$

Where the $v_{sd}^{gv}$ term represents the peak grid voltage $V_{gp}$, and can be considered constant during normal operation. Furthermore, the term $P_r$ from equation (4.34) is considered a disturbance for the DC-Link control loop and will be compensated by the control.

The linear transfer function of the DC-Link result in equation (4.35).

$$G_{dc}(s) = \frac{I_{fd}^{gv}(s)}{W_{dc}(s)} = \frac{3V_{gp}}{C_{dc}s} \tag{4.35}$$

This continuous transfer function is then discretized with the sampling period $Ts$, including the *zero-order hold* effect of the A/D sampling, as in (4.36)

$$G_{dc}(z) = \mathbb{Z}\left\{\frac{1-e^{sT_s}}{s}G_{dc}(s)\right\} = \frac{z-1}{z}\mathbb{Z}\left\{\frac{G_{dc}(s)}{s}\right\} \tag{4.36}$$

The closed loop dynamics of the grid filter current control (4.37), can also be included in the plant dynamics of the DC-Link, as presented in equation (4.38).

$$G_{filt\_cl}(z) = \frac{C_{filt}(z)G_{filt}(z)}{1 + C_{filt}(z)G_{filt}(z)} \tag{4.37}$$

$$G_{dc\_filt}(z) = G_{dc}(z)G_{filt\_cl}(z) \tag{4.38}$$

A low-pass pre-filter can be included on the reference path of the DC-Link controller and has to be considered in the design process. This pre-filter improves the stability of the DC-Link voltage controller. Also since the main control goal of the DC-Link voltage controller is to maintain a constant DC-Link voltage, the designed requirements for the controller will focus mainly on fast disturbance rejection.

$$C_{dc}(z) = Ki\frac{T_s}{z-1} + Kp \tag{4.39}$$

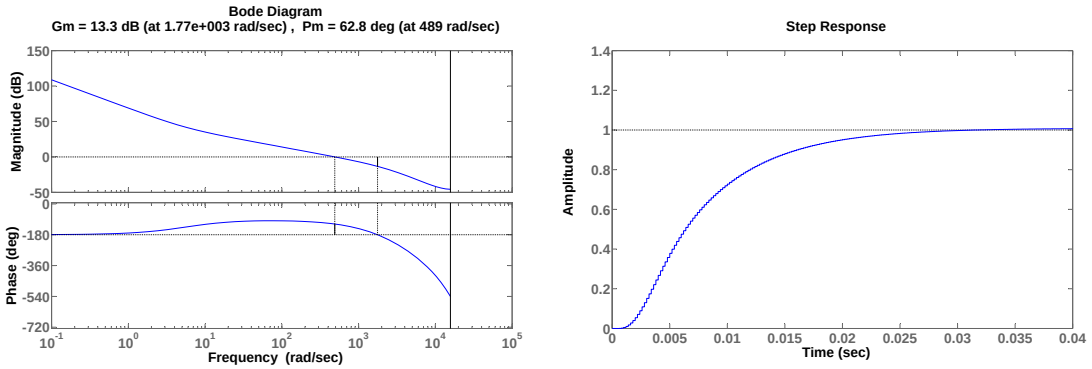


(a) Phase and gain margins of the open loop system

(b) Step response of the closed loop system

Figure 4.18: Frequency and time domain DC-Link voltage controller design plots.

The Bode diagram of the DC-Link open loop control system in Figure 4.18, show good gain and phase margins of the systems, and a fast controller response, this together with the high open loop gain of the system will provide good disturbance rejection capabilities to the closed loop system.

Furthermore, the low-pass pre-filter of the DC-Link voltage controller eliminates any significant overshoot, as can be observed from the step response of the closed loop system in Figure 4.18(b).

The *Simulink* implementation of DC-Link voltage controller controller, with pre-filter, dynamic command limitation and anti-windup, is presented in Figure 4.19.

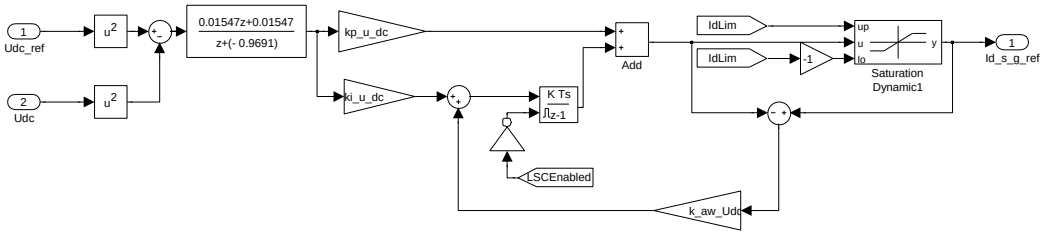


Figure 4.19: Simulink implementation of the DC-Link voltage controller.

### Fault operating mode

The modifications proposed for fault operation mode of the grid side converter, discussed in the previous chapter and in the conceptual diagram from Figure 3.9, are:

- implementation of a grid current reference magnitude limiter, with (partial) reactive current priority
- implementation of the grid code reactive current prescription as a function of the voltage dip
- overloading of the grid side converter for the duration of the voltage dip, in order to get more reactive current output through the grid filter

The logic of the first two modifications was implemented as *Embedded Matlab functions*, as presented in Figure 4.20.

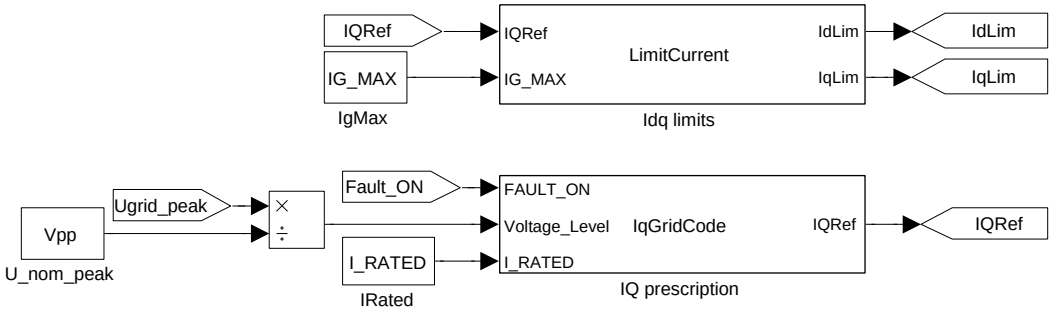


Figure 4.20: Reactive current prescription during fault and grid filter current priority calculation.

The overloading of the grid side converter modification was included in the current priority calculation, by temporarily increasing the rated current limit parameters of the converter.

The overall implementation of the grid side converter controller with fault operation modifications is presented in Figure 4.21.

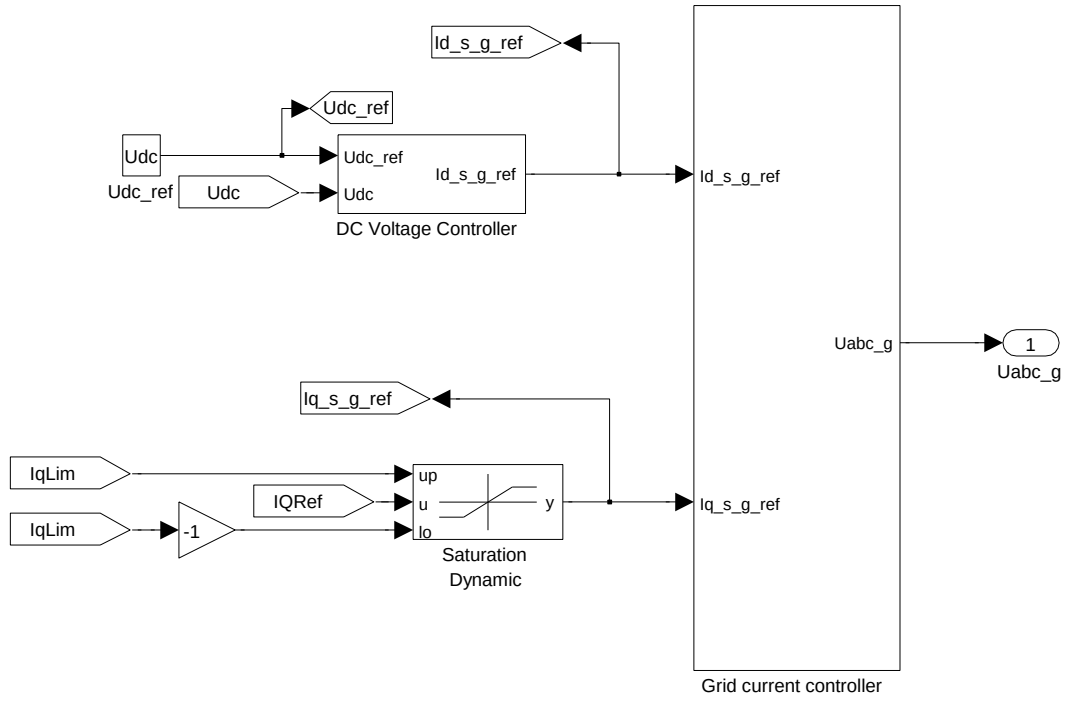


Figure 4.21: Grid side converter controller with fault operation modifications.

### 4.2.3 High level controller

The *High Level Controller* logic has been implemented as a state machine in *Stateflow*. It is composed of three parallel running sub-state machines: the *rotor side converter control logic*, the *grid side converter control logic* and the *rotor side converter protection logic*, as presented in Figure 4.22, and described next.

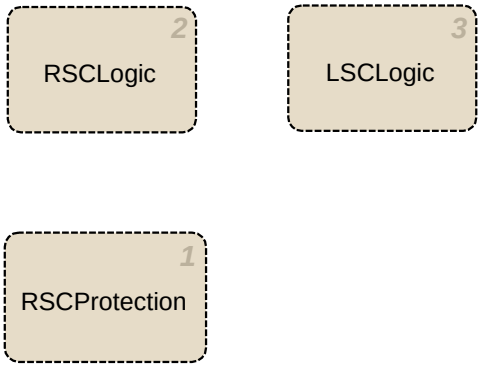


Figure 4.22: High level controller main processes.

**RSCLogic state machine** The *rotor side converter control logic* is the most complex from the three sub-state machines of the *High Level Controller*, and is

presented in Figure 4.23. Its main functionality is to monitor and control the different operating stages of the DFIG, manage timing issues between the operating states, and to provide references and ramping for the *lower level controllers*.

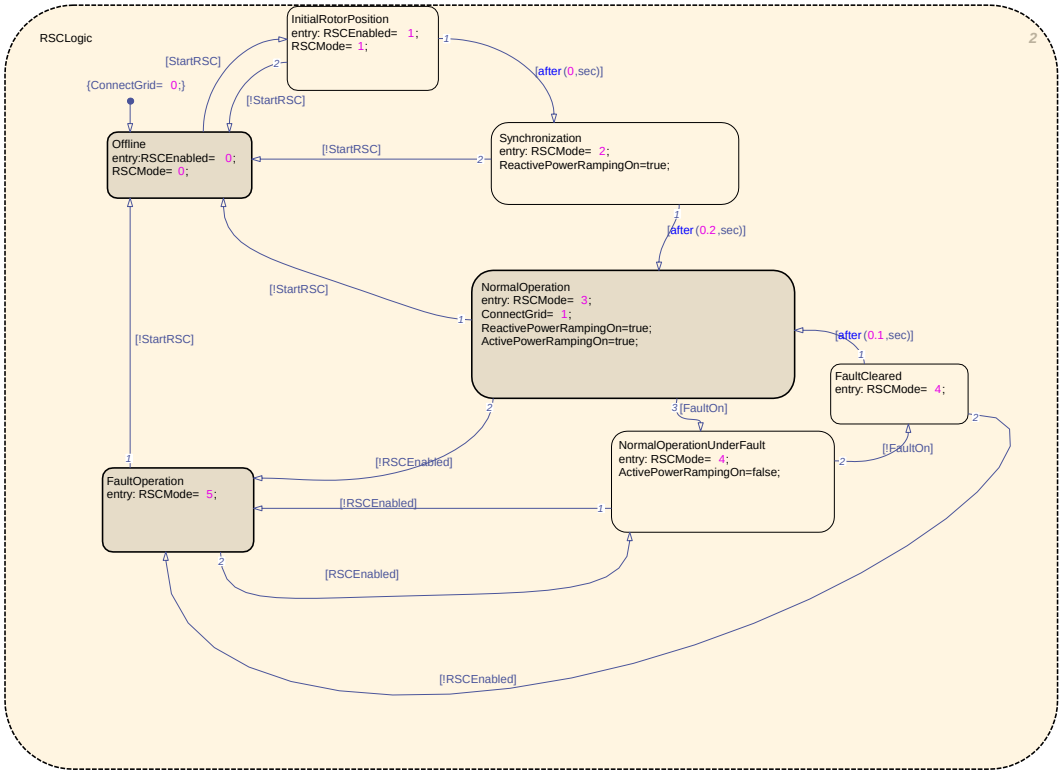


Figure 4.23: Rotor side converter control state machine.

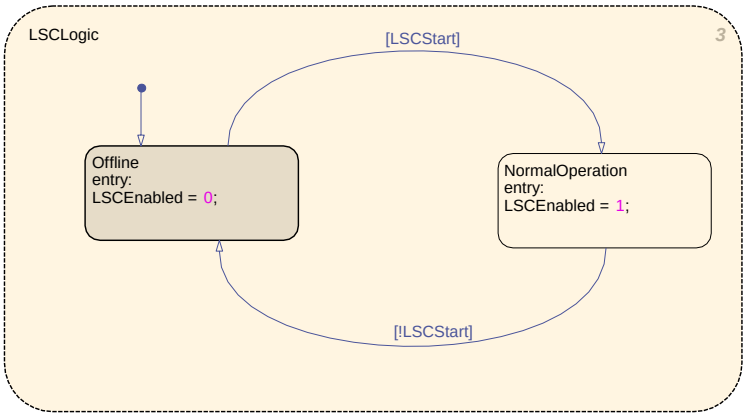


Figure 4.24: Grid side converter control state machine.

**LSCLogic state machine** The grid side converter control logic is quite straightforward, as can be observed from 4.24, it only controls the enabling of the grid side converter.

**RSCProtection state machine** The rotor side converter protection mechanism, presented in Figure 4.25, is composed of three parallel running processes which handle: the *software over-current tripping* of the rotor side converter, the *rotor crowbar timing and control*, the *stator crowbar timing and control*.

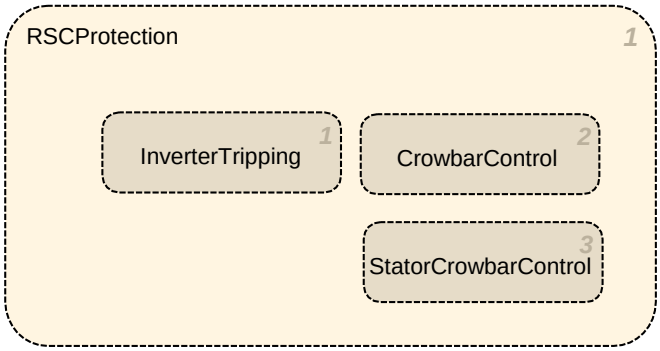


Figure 4.25: Rotor side converter software protection logic.

The rotor converter over-current tripping mechanism, depicted in Figure 4.26, monitors the rotor current magnitude and disables the switches in case the maximum allowed value $IR\_MAX(2 \times INV\_RATED)$ is exceeded. The switches are re-enabled after the rotor current magnitude has decreased to the safe value of $IR\_MIN(0.4 \times INV\_RATED)$, and after a minimum coasting time.

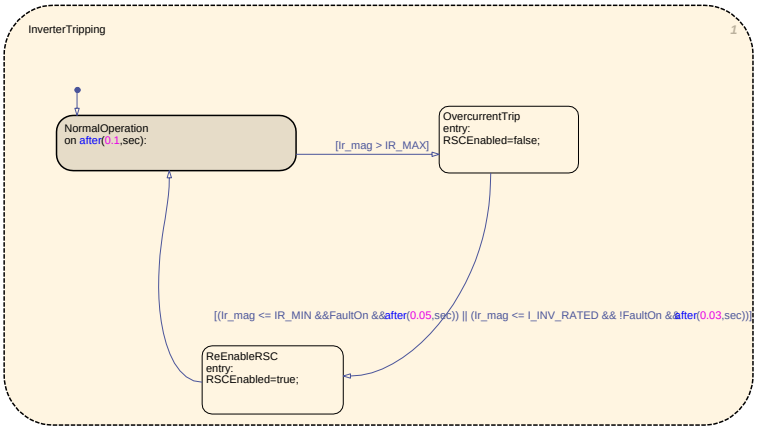


Figure 4.26: Software over-current tripping of the rotor side converter.

The rotor side converter coasting mechanism has been designed this way in order to ensure the rotor side converter can regain control of the rotor currents, and subsequent over-current tripping of the inverter is avoided. Increasing the short period over-current limits when designing the converter switches, can have a positive effect on the fault ride-through performance of the DFIG system. This is an important aspect when considering generating reactive current through the DFIG

stator during the fault in conformity with the grid codes, since the rotor side converter should regain control of the rotor currents in under 100 ms, after the initial voltage sag.

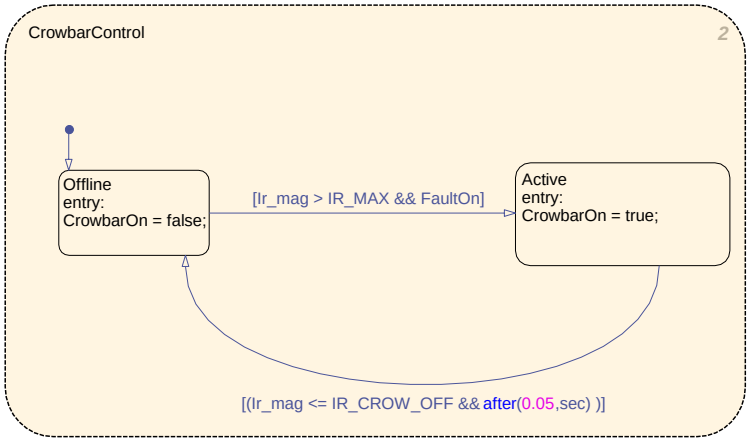


Figure 4.27: Rotor crowbar control and timing logic.

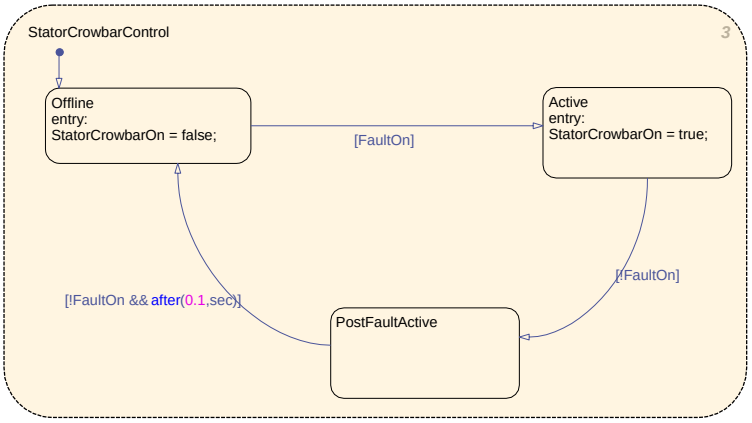


Figure 4.28: Stator crowbar control and timing logic.

The rotor crowbar control logic from Figure 4.27, implements a simple hysteresis controller with a delay mechanism, in order to avoid destabilizing the system by firing the crowbar to often.

The stator crowbar control logic was implemented as suggested in [23], the stator crowbar is active for the entire duration of the fault and a short period after, in this way the stator damping is increased during the fault transients and stability of the entire system is improved.

# Chapter 5

# Simulation of full scale system

In order to validate the concepts presented in the previous chapter, simulation scenarios have been employed on a full scale system built around a 2MW DFIG. The parameters of this machine as well as the description for the other components used in the final system are detailed in Appendix A.3.

Three different aspects will be covered next. Firstly, results that validate the normal operation of the system are presented. Than the behavior of the system under a 40% voltage sag is analyzed, and the results from the two control strategies previously described are compared. In order to test the feasibility of the system in terms of LVRT, a 80% voltage sag study case is presented in the last section of this chapter. The two control strategies are tested on both rotor and stator mounted crowbar-systems. The obtained results are compared and analyzed in relation with the latest Danish grid codes, and calculated according to IEC:2008 61400-21 standard for measurement and assessment of power quality characteristics of grid connected wind turbines. The calculation formulas employed by this standard are presented next:

The fundamental's Fourier coefficients of the phase voltages are first calculated over one fundamental cycle $T$, where $f1$ is the fundamental frequency.

$$u_{a,cos} = \frac{2}{T}\int_{t-T}^{t} u_a(t)\cos\left(2\pi f_1 t\right)\,\mathrm{d}t \tag{5.1}$$

$$u_{a,sin} = \frac{2}{T}\int_{t-T}^{t} u_a(t)\sin\left(2\pi f_1 t\right)\,\mathrm{d}t \tag{5.2}$$

The voltage and current vector components of the fundamental positive sequence are calculated using:

$$u_{1+,cos} = \frac{1}{6}\left[2u_{a,cos} - u_{b,cos} - u_{c,cos} - \sqrt{3}\left(u_{c,sin} - u_{b,sin}\right)\right] \tag{5.3}$$

$$u_{1+,sin} = \frac{1}{6}\left[2u_{a,sin} - u_{b,sin} - u_{c,sin} - \sqrt{3}\left(u_{b,cos} - u_{c,cos}\right)\right] \tag{5.4}$$

$$i_{1+,cos} = \frac{1}{6}\left[2i_{a,cos} - i_{b,cos} - i_{c,cos} - \sqrt{3}\left(i_{c,sin} - i_{b,sin}\right)\right] \tag{5.5}$$

$$i_{1+,sin} = \frac{1}{6}\left[2i_{a,sin} - i_{b,sin} - i_{c,sin} - \sqrt{3}\left(i_{b,cos} - i_{c,cos}\right)\right] \tag{5.6}$$

The active and reactive powers of the fundamental positive sequence are then:

$$P_{1+} = \frac{3}{2}\left(u_{1+,cos}i_{1+,cos} + u_{1+,sin}i_{1+,sin}\right) \tag{5.7}$$

$$Q_{1+} = \frac{3}{2}\left(u_{1+,cos}i_{1+,sin} - u_{1+,sin}i_{1+,cos}\right) \tag{5.8}$$

and the effective phase-to-phase voltage of the fundamental positive sequence is:

$$U_{1+} = \sqrt{\frac{3}{2}\left(u_{1+,cos}^2 + u_{1+,sin}^2\right)} \tag{5.9}$$

The effective active and reactive currents of the fundamental positive sequence are:

$$I_{P1+} = \frac{P_{1+}}{\sqrt{3}U_{1+}} \tag{5.10}$$

$$I_{Q1+} = \frac{Q_{1+}}{\sqrt{3}U_{1+}} \tag{5.11}$$

When analyzing the behavior of DFIG under fault conditions several quantities like stator voltages, rotor currents, DC-Link voltage, etc are of interest. Plotting all these quantities together yields *crowded* figures that might be difficult to read at the default scaling factor. In order to surpass this, all the figures containing simulation and experimental results are listed once more in Appendix F.1 and Appendix F.2 with a higher scaling factor.

## 5.1 Normal Operation

As stated before, the present study case is used in order to confirm the nominal behavior of the system under normal operation. This scenario will not be detailed exhaustively since it is not of main interest.

The study case starts after the DFIG has passed the synchronization phase and is running at super-synchronous speed, ready to start exchanging power with the grid. After 0.9 seconds the active power reference for the stator is changed and is reflected as a -0.4 p.u. step in the stator active current. Shortly after, when the simulation time has reached 1 second, the reactive current reference for the grid side converter is changed from 0 to -0.3 p.u. Finally the reactive power reference for the stator is changed and it seen as a -0.06 p.u. step in reactive current at 1.4 seconds.

Figure 5.1 presents the behavior of the DFIG under normal operation in terms of active and reactive current injection into the grid. The first graph presents the line to line voltage amplitude in per unit at the point of common coupling (PCC). This value as well as the others presented in Figure 5.1 are expressed as suggested by the IEC:2008 61400-21 standard for measurement and assessment of power quality characteristics of grid connected wind turbines.

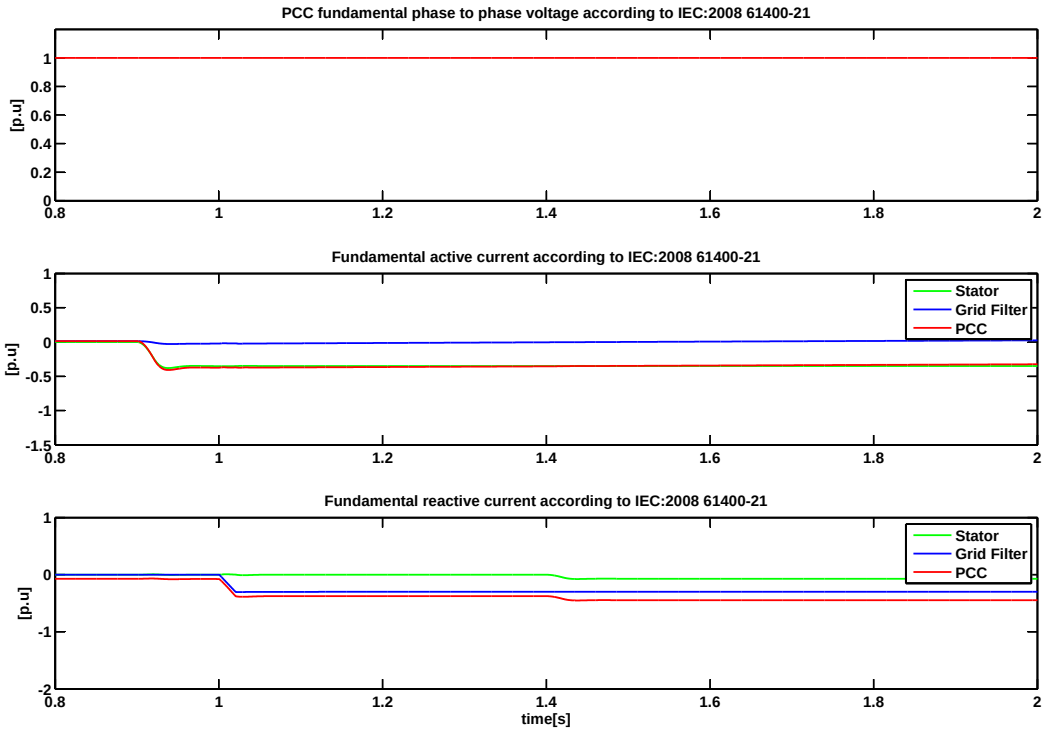


Figure 5.1: Fundamental quantities according to IEC:2008 61400-21 during normal operation.Appendix F.1.

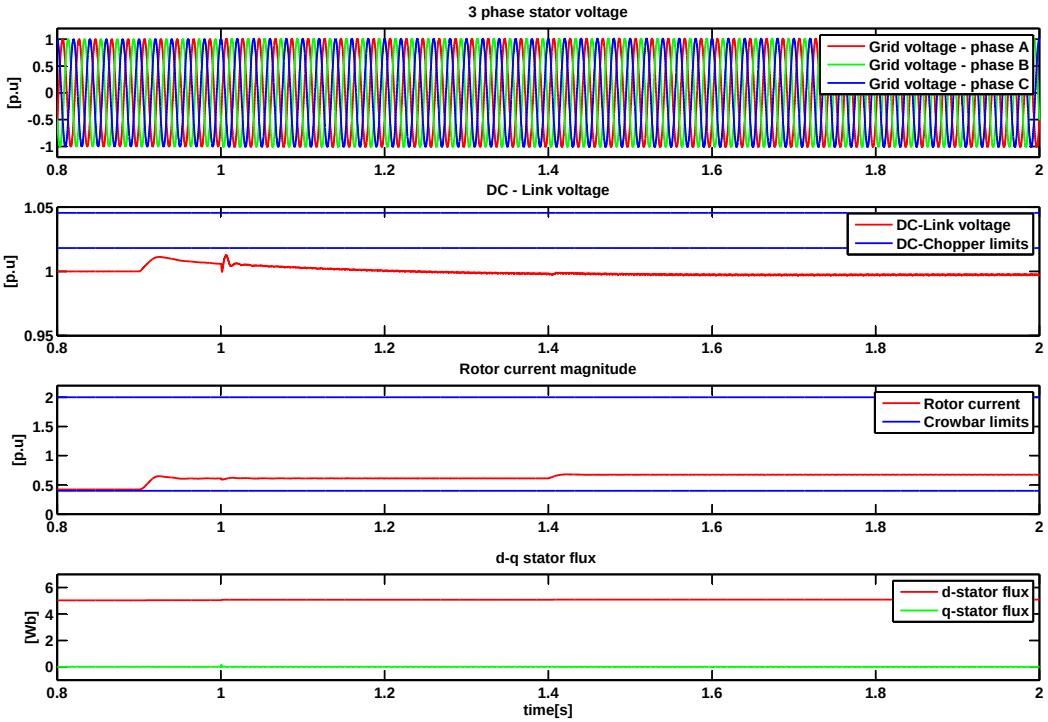


Figure 5.2: Instantaneous measurements during normal operation.Appendix F.2.

The second graph on Figure 5.1 presents the active current exchange. A step in the active stator current at 0.9 seconds, corresponding to the power reference change, can be observed. It can also be seen that a small amount of active current is injected through the grid side converter because of the super-synchronous generator speed. After the generator is slowed down, the grid side converter starts to consume active current and the value seen at the PCC is slightly smaller than the one provided through the stator.

The last graph on Figure 5.1 shows the reactive current flow. A small offset in the reactive current can be seen at the PCC. This can be accounted to the presence of the capacitor in the grid side filter. Steps in the reactive current after 1 and 1.4 seconds as prescribed in the initial scenario can be observed.

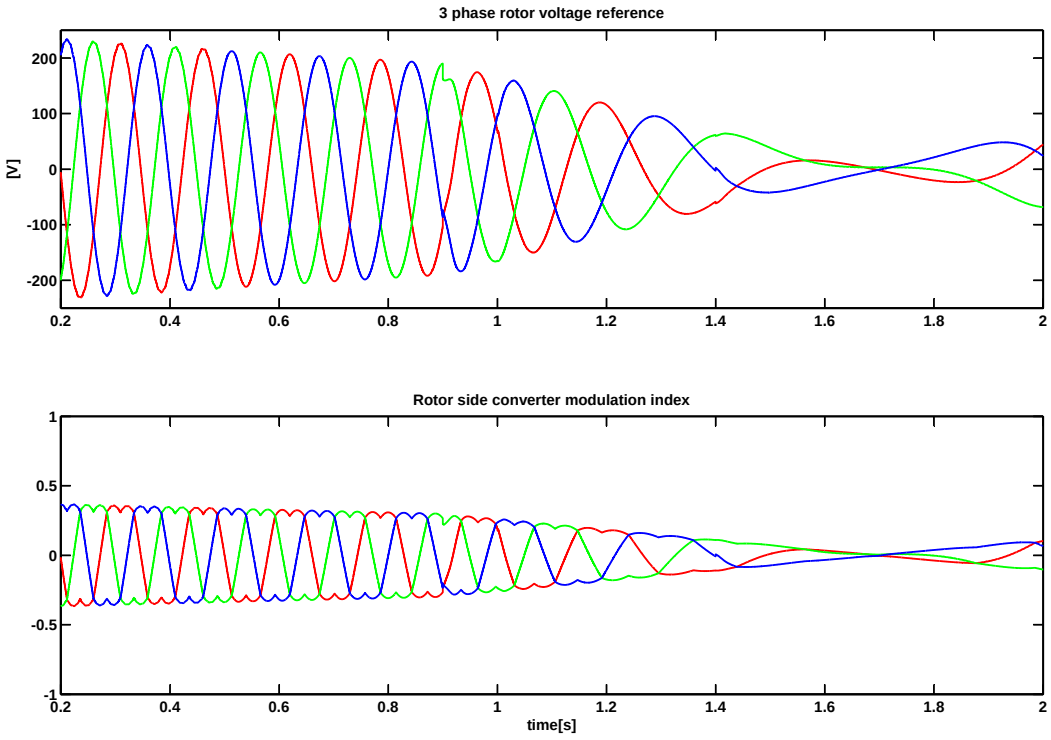


Figure 5.3: Rotor voltage reference and modulation during normal operation.Appendix F.3.

Figure 5.2 emphasizes the steady behavior of system values, like: DC-Link voltage, rotor current and stator flux, during normal operation. These values are presented here in order to serve as reference point for the following subsections where these quantities are analyzed for the system under fault conditions.

It can be observed that both the DC-Link voltage and the rotor current magnitude have linear behavior, between the safety limits. Small transients corresponding to the moments when the power/current references change can be observed in both the DC-Link and the rotor current. One important aspect that has to be noticed is the perfect constant flux on the d-q axes. As it will be seen in the following sections, the stator-flux is seriously perturbed during fault conditions.

Analyzing Figure 5.1 and Figure 5.2 it can be concluded that the control concepts implemented for normal operation function as expected.

Figure 5.3 presents the output of the rotor side converter control strategy. The output rotor voltage is presented together with the modulation index of the inverter. As mentioned before, the generator is running at super-synchronous speed. The transition to sub-synchronous speed occurs, as it can be deducted from Figure 5.3, after around 1.7 seconds of simulation time.

## 5.2 Medium Voltage Drop

This section provides analysis of the system behavior for a 40% voltage sag. As it was presented in the previous chapter, two methods for improving the DFIG control in order to enhance its FRT capability have been identified and implemented. The results for each of these two strategies are presented next, keeping in mind that the Danish grid codes requirement for a voltage drop of this magnitude impose 0.8 p.u. reactive current support, provided with a tolerance of 20% after 100ms from the fault inception.

### 5.2.1 Method 1: Full disturbance compensation

This study case, as well as all the other analyzed FRT study cases, starts with the DFIG running in normal operation. After 0.3 seconds of simulation time a 0.65 p.u. step change in the stator active current is applied. After 0.4 seconds, the grid voltage drops to 60% of its nominal value for a duration of 0.5 seconds and the FRT strategies are enabled.

It has to be reminded here, that the active and reactive stator power controllers are replaced by low pass filters in the FRT control strategy, in order to improve the stability and the time response of the system. Under these aspects, the reference for the active and reactive current is prescribed directly.

The full disturbance compensation method implies, as described in Chapter 4, estimation of the disturbing terms resulting from the rotor flux induced back-e.m.f., represented by $j(\omega-\omega_r)\sigma L_r \overrightarrow{i_r}$ and from the stator flux induced back-e.m.f., represented by the $j(\omega-\omega_r)\frac{L_m}{L_s}\overrightarrow{\psi_s}$ and $\frac{L_m}{L_s}\frac{d\overrightarrow{\psi_s}}{dt}$. After these quantities are estimated they are used as feed-forward terms in the control structures.

Figure 5.4 presents the active and reactive current flow for this scenario, as required by the IEC:2008 61400-21 standard. The first graph presents the phase to phase voltage at the PCC. A 40% drop in amplitude lasting for 0.5 seconds can be observed after 0.4 seconds.

When a voltage drop is detected, the injection of active current is ramped down to zero, and the injection of reactive power receives primary priority, as imposed by the grid codes. It can be seen, from the last two graphs in Figure 5.4 that after 100 ms the active power production reaches 0, and the reactive current injection reaches the set-point imposed by the grid codes.

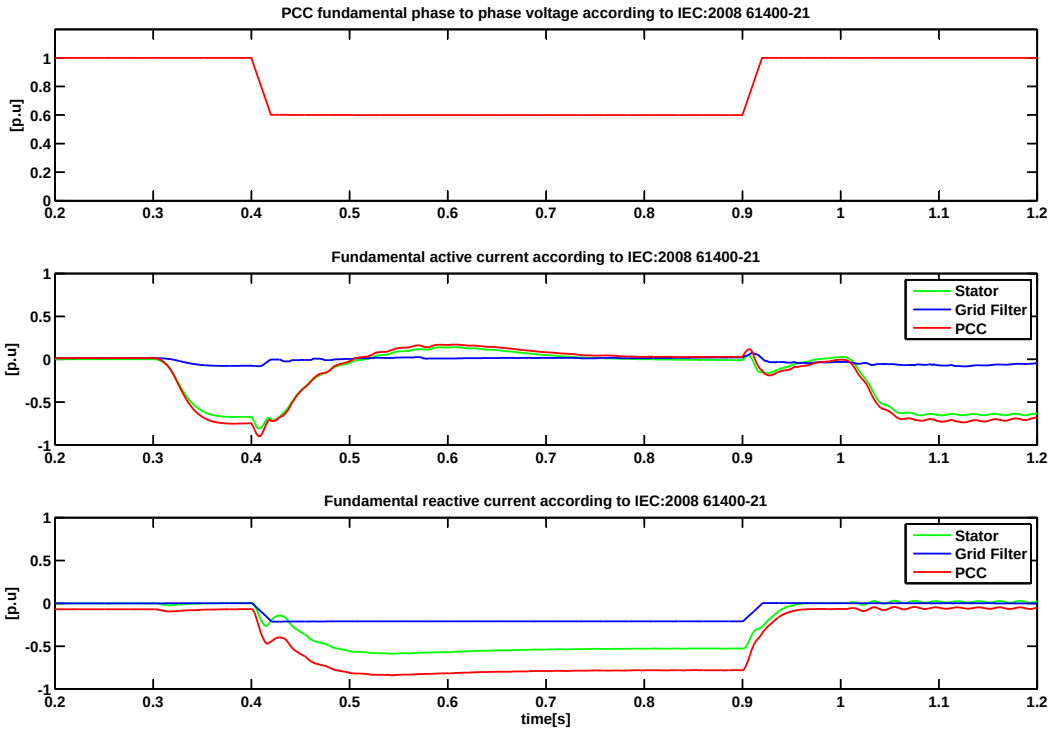


Figure 5.4: Fundamental quantities according to IEC:2008 61400-21 during a 40% voltage sag. Full disturbance compensation method.Appendix F.4.

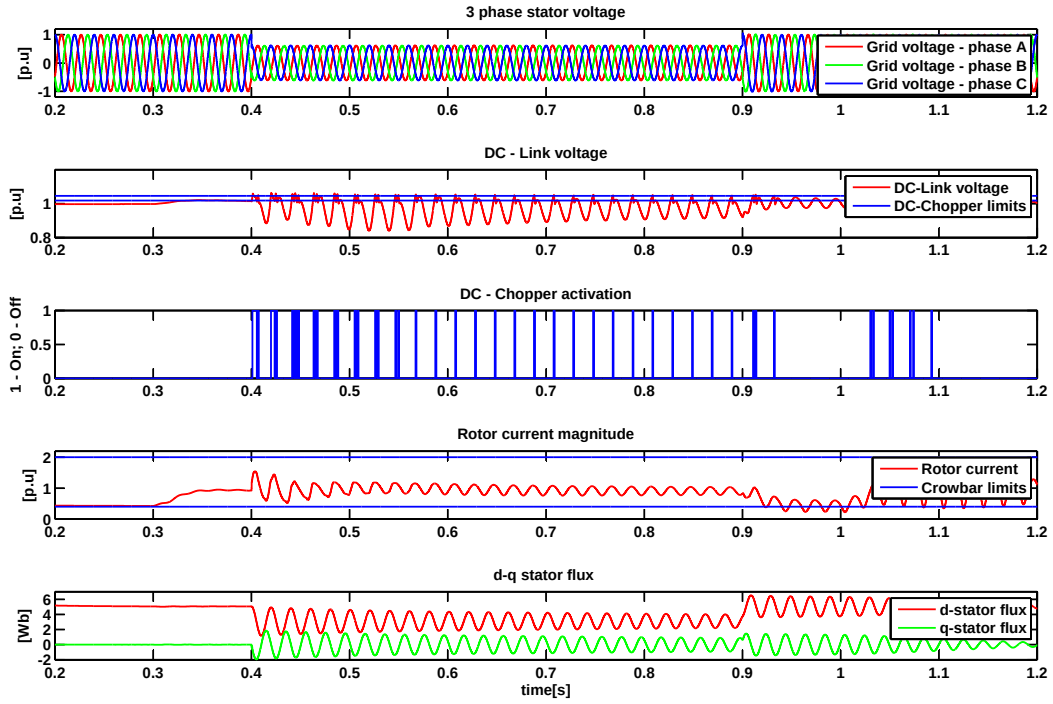


Figure 5.5: Instantaneous measurements during a 40% voltage sag. Full disturbance compensation method. Appendix F.5.

The reactive current is injected from both the stator and the grid side. The grid side provides steady reactive current injection throughout the entire voltage drop duration. However, the current injected through the stator is not that stable, and this is because, as seen in Figure 5.5, the rotor side current controller has to face serious transients induced by the voltage drop.

Analyzing from the PCC perspective and using the IEC:2008 61400-21 standard it can be said that this strategy provides good FRT capability, with reactive current injection aligned with the grid codes requirement. However from a system point of view the results are not that satisfactory, as can be seen in Figure 5.5.

Compensating all the disturbances as feed forward terms has as major drawback, the saturation of the rotor side converter (see Figure 5.6), thus resulting in a delay in damping the 50Hz component induced in the d-q stator-flux. The 50Hz component in the rotating frame appears as a cause of the DC components induced in the flux in the natural reference frame by the drop in the voltage. The undamped oscillating stator flux perturbs the rotor current making it difficult to be handled by the controllers. The control of the hectic rotor current, in addition to the injection of reactive current, as required by the grid codes, unbalance the DC-Link resulting in unstable behavior and multiple activations of the DC-Chopper.

Concluding the performance of this strategy it can be said that, even though it provides good FRT capability from a network point of view, from a structural point of view the oscillating stator flux might result in mechanical stress on the wind turbine. Even more, the diodes of the converter, together with the switch that activates the DC-Chopper, are overloaded during the fault, and can be damaged.

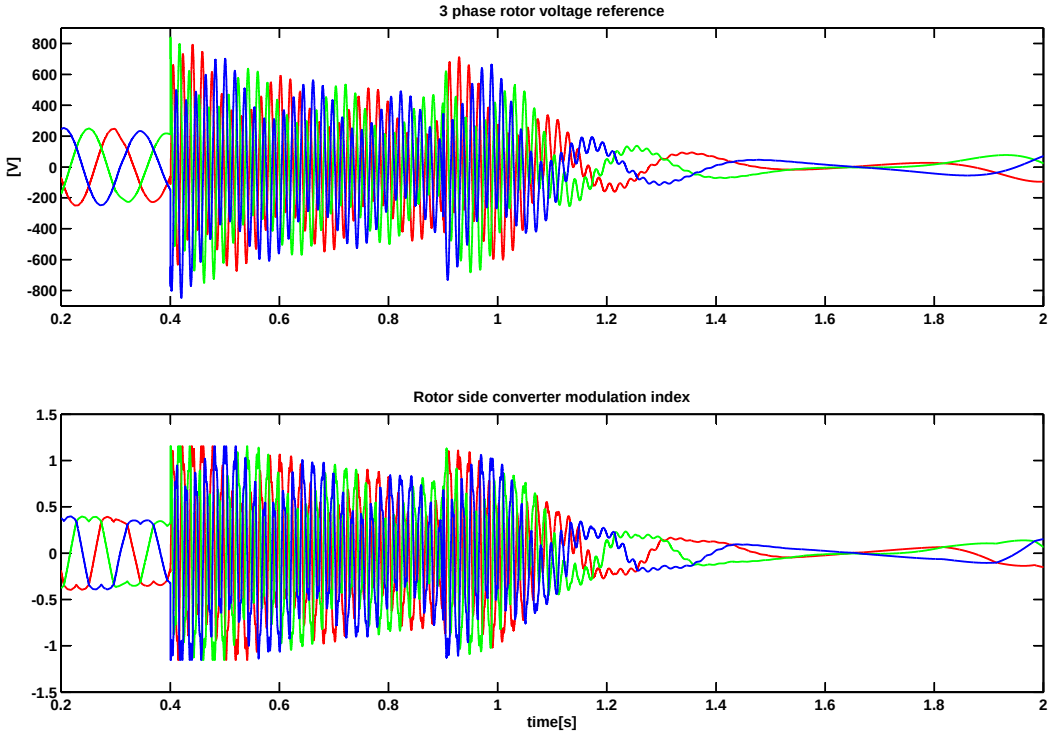


Figure 5.6: Rotor voltage reference and modulation during a 40% voltage sag. Full disturbance compensation method.Appendix F.6.

### 5.2.2 Method 2: Partial disturbance compensation with improved flux damping

In order to avoid the stress imposed on the wind turbine and on the power electronics by the oscillating stator flux during a grid fault, an alternative method has been proposed and described in Chapter 4. The partial disturbance compensation with improved flux damping strategy tries to avoid the saturation of the rotor side converter by reengineering the control structure so that it reacts only to the fundamental components of the stator flux and rotor current. In order to do this, notch filters are placed on the rotor current feedback path and on the stator flux feed forward terms, and the controller is redesigned so that it accounts for these new structural changes. Moreover, the rotor currents spikes are avoided by applying the disturbance compensation with a weighting factor decreasing with time.

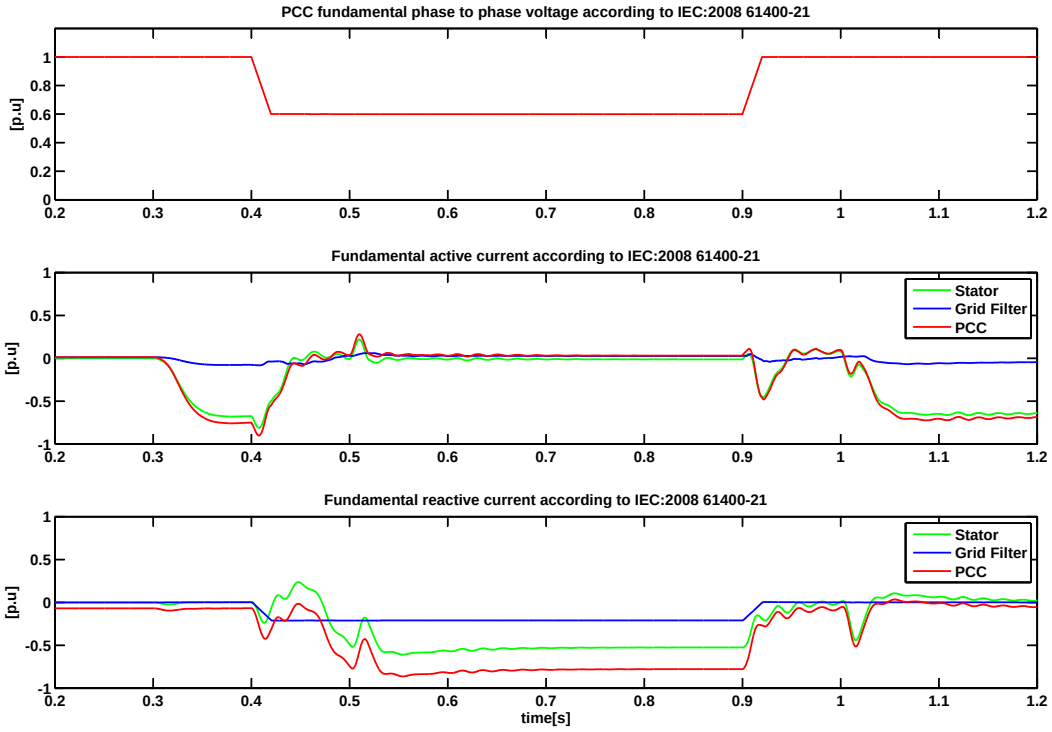


Figure 5.7: Fundamental quantities according to IEC:2008 61400-21 during a 40% voltage sag. Partial disturbance compensation with improved flux damping method.Appendix F.7.

In order to test this control strategy, the simulation scenario presented in the previous subsection was used. Figure 5.7 presents the current flow in the system according to the IEC:2008 61400-21 standard. As before, the first graph shows the line to line voltage drop in p.u, while the last two graphs show the variation in active and reactive current.

As in the previous study case, once a voltage drop is detected, the active current is ramped to zero and reactive current injection as required by the grid codes is initiated.

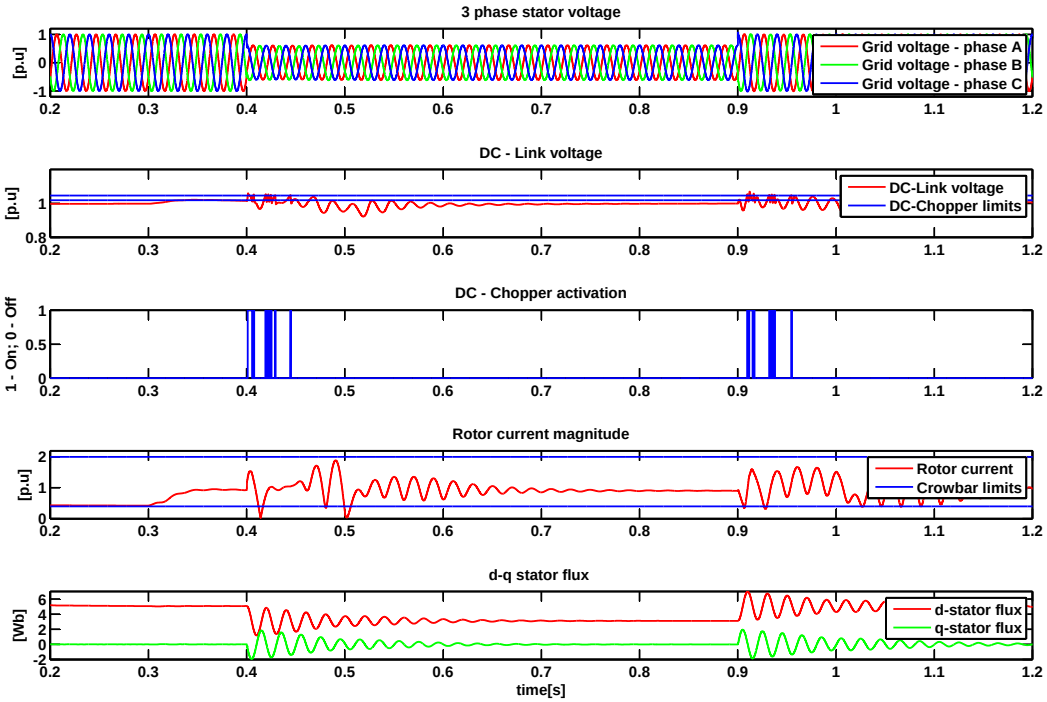


Figure 5.8: Instantaneous measurements during a 40% voltage sag. Partial disturbance compensation with improved flux damping method.Appendix F.8.

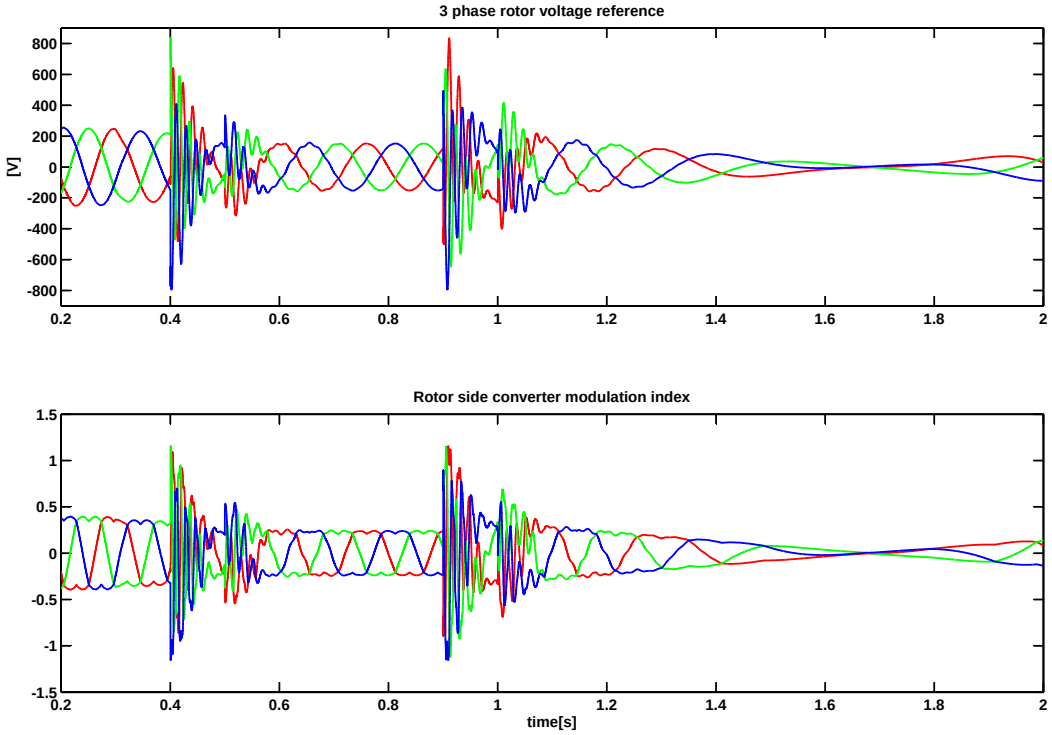


Figure 5.9: Rotor voltage reference and modulation during a 40% voltage sag. Partial disturbance compensation with improved flux damping method.Appendix F.9.

It can be seen that the reactive current injection takes around 150ms to reach the set point imposed by the grid codes compared with the required value of 100ms, satisfied by the previous strategy. Even more, for a short period of time at the beginning of the fault, the generator consumes all the reactive power generated by the grid side converter. This is due to the fact that the rotor current references are ramped to zero for a short period at the beginning of the fault in order to avoid high rotor currents that would coast the inverter.

From a network point of view, this method does not perform as good as the previous one. However, this strategy has its advantages when looking at the system dynamics and stress during fault, see Figure 5.8.

Compared with Figure 5.5 from the previous subsection, the quantities presented in Figure 5.8 present a less *aggressive* behavior. The rotor side converter is saturated only for a short period of time, while the full compensation is applied. Otherwise, as seen in Figure 5.9, only the 50Hz fundamental component is control by the rotor side converter.

The flux damping strategy works and, as it can be seen on the last graph presented in Figure 5.8, the 50Hz component induced in the d-q stator flux is eliminated.

The rotor current magnitude also stabilizes as soon as the stator-flux reaches steady values and the oscillating feed-forward terms are canceled. In this situation, the DC-Link also presents a much more stable behavior and the DC-Chopper only activates at the inception and at the clearing of the fault, when the feed-forward terms have their maximum value.

Concluding the performance of this strategy it can be said that it has better results from a structural point of view. The stress on the system is smaller than the one induced by the full disturbance compensation method. Conversely this method comes with the disadvantage of not fulfilling the grid code requirements completely.

This method could be improved if the short period current overloading limit of the switches would be increased. In this manner the reactive current reference would not have to be ramped down at the beginning of the fault, thus reactive current support would be achieved faster.

## 5.3 Low Voltage Drop

In order to test the LVRT performance of the two control strategies a 80% voltage sag study case was employed. A voltage drop of 80% is the lowest a wind turbine has to withstand without disconnecting according to the Danish grid codes. For a voltage drop of this magnitude the afore mentioned grid codes impose 1 p.u. reactive current support, provided with a tolerance of 20% after 100ms from the fault inception.

Simulations were firstly conducted on the classic system, that involves a rotor crowbar as a protection mechanism. Later on, the improved control system was tested in addition with a newer system that proposes mounting the crowbar on the stator.

The complete simulation schematic of the plant can be found in Section 4.1.7 and the parameters for the components are listed in Appendix A. Results from the four study cases will be analyzed next.

### 5.3.1 Method 1: Rotor Crowbar. Full disturbance compensation

The hypothesis of the present study case are similar to the ones presented in the previous sections. The only difference is that the voltage sag is doubled in size, reducing the line to line voltage to 20% of its nominal value.

Before looking at the interaction between the turbine and the grid in terms of active and reactive current injection it makes sense to analyze the behavior of the control system and of the protection devices. Figure 5.10 shows the quantities of interest in this case.

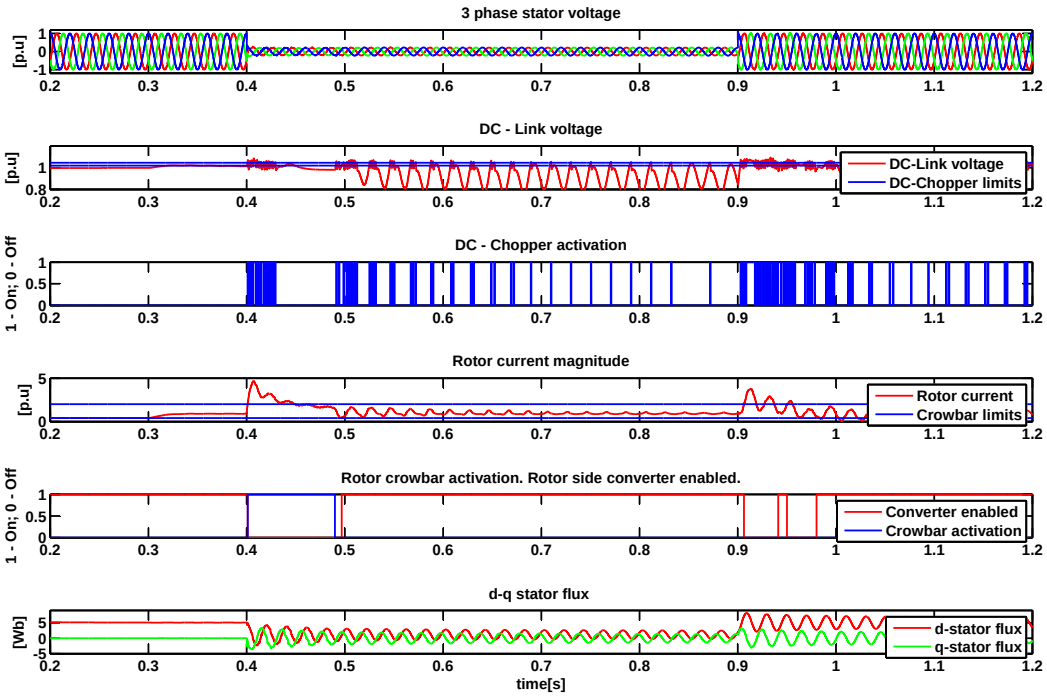


Figure 5.10: Instantaneous measurements during an 80% voltage sag. Rotor Crowbar. Full disturbance compensation method.Appendix F.11.

A first aspect that should be noted is that, when a voltage drop of this magnitude occurs, the rotor current magnitude can not be controlled by the rotor side inverter not even with the disturbance compensation strategy activated. Consequently the current magnitude exceeds the safety limits, thus the crowbar is activated and the rotor side converter is disabled. After 100ms the rotor side converter is re-enabled and tries to regain control. The crowbar is only deactivated when the rotor currents have reached the predefined safety limit.

The problems previously identified for this control strategy can also be observed for low voltage drops. The undamped stator flux and the large ripple in the DC-Link generating numerous activations of the DC-Chopper can be observed in Figure 5.10.

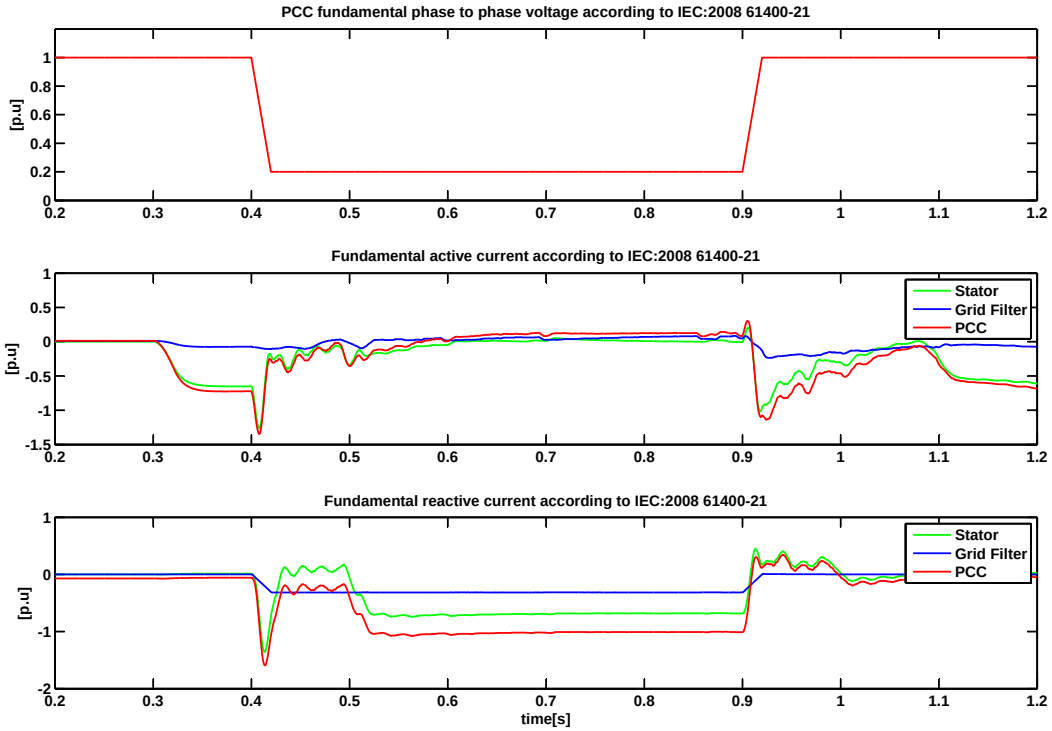


Figure 5.11: Fundamental quantities according to IEC:2008 61400-21 during an 80% voltage sag. Rotor Crowbar. Full disturbance compensation method.Appendix F.10.

Figure 5.11 shows the exchange of active and reactive current between the stator, the grid and the grid filter. The main problem of the systems having the crowbar mounted on the rotor is that during crowbar activation the rotor gets short circuited and the generator starts to consume reactive current. Also, disabling the rotor side converter delays the injection of reactive current, as suggested by the grid codes. On the last graph in Figure 5.11 it can be seen that the reactive current at the PCC reaches the value dictated by the grid codes after approximately 150 ms, the reactive current injection through the stator being delayed by the crowbar activation.

By using this improved control strategy, the crowbar doesn't have to be activated again at the moment when the fault is cleared. It is enough just to disable the inverter in order to avoid the rotor over current. It can be seen in Figure 5.10 that the crowbar doesn't activate at the end of the fault, but the inverter gets disabled twice due to over currents.

### 5.3.2 Method 2: Rotor Crowbar. Partial disturbance compensation with improved flux damping

Figure 5.12 and Figure 5.17 picture the behavior of the system equipped with the partial disturbance compensation strategy while experiencing the same voltage drop as in the previous scenario. It can be seen that the stator flux is damped and the DC-Link is more stable than in the previous case.

Two major disadvantages can be identified by analyzing the two figures below. The first one is that the rotor currents take longer to reach the safety limits so the reactive current injection through the stator is delayed even more. Only after around 200 ms the reactive current injection reaches the value required by the grid code.

The second drawback is that the controller can not regain control of the rotor currents without a second crowbar firing at the moment of fault clearing. This has as secondary effect reactive power consumption by the stator, as seen in Figure 5.17. This kind of behavior is not recommended because it could destabilize the transmission network.

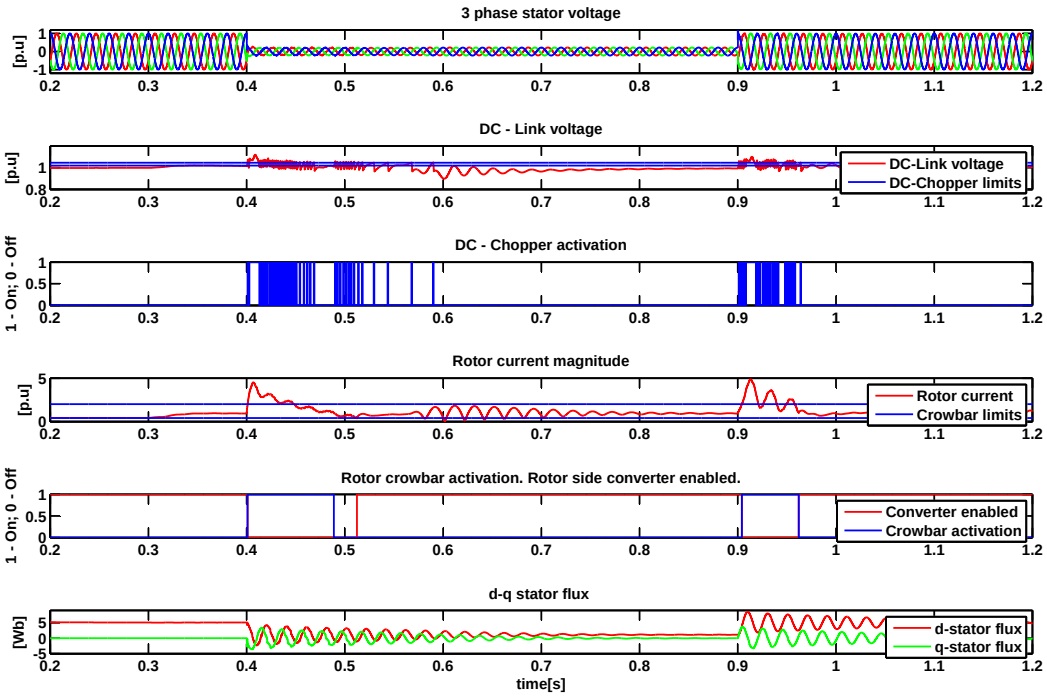


Figure 5.12: Instantaneous measurements for DFIG experiencing a 80% voltage sag. Rotor Crowbar. Partial disturbance compensation with improved flux damping method.Appendix F.13.

To conclude the performance of the rotor-crowbar based systems in correlation with the improved control strategies it can be said that rotor crowbar systems together with the full disturbance compensation strategy have a good chance of providing LVRT, but at the cost of extended stress on the mechanical and elec-

trical components of the WT. From the obtained results it can be said that the partial compensation strategy has more disadvantages than advantages and is not recommended.

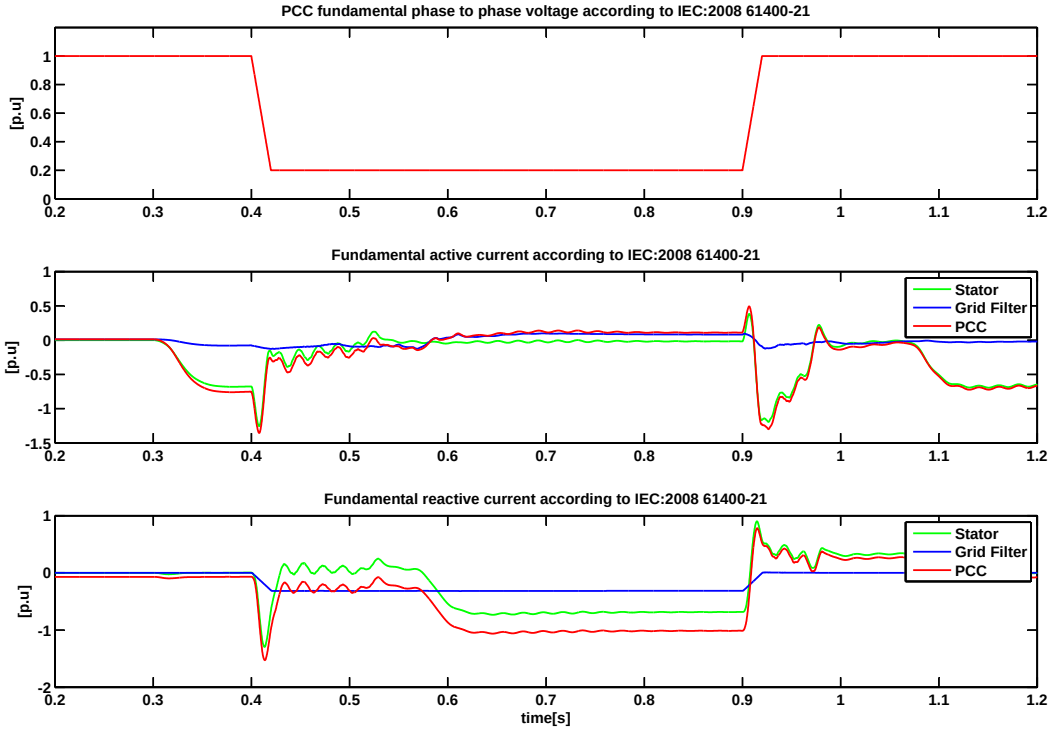


Figure 5.13: Fundamental quantities according to IEC:2008 61400-21 during an 80% voltage sag. Rotor Crowbar. Partial disturbance compensation with improved flux damping method. Appendix F.16.

### 5.3.3 Method 3: Stator Crowbar. Full disturbance compensation

One of the main identified problems when dealing with DFIG systems under fault conditions is the oscillating stator flux in the d-q reference frame. Flux damping methods have been presented before by feed forwarding the flux disturbance to the controller. A simpler method, involving a stator mounted crowbar, was presented in Chapter 3. The idea behind the stator crowbar is to increase the stator resistance during the fault, thus providing a passive damping of the stator flux.

The same simulation scenario as in the previous study cases has been conducted, only this time the crowbar was mounted on the stator and activated during the entire fault duration.

Figure 5.14 presents the values of interest from the system. It can be noted that the stator flux oscillations are smaller in amplitude and are damped even while using the full disturbance compensation strategy. The two rotor current spikes occurring at the beginning and clearing of the fault are smaller in magnitude, and the rotor current in general has a more stable behavior.

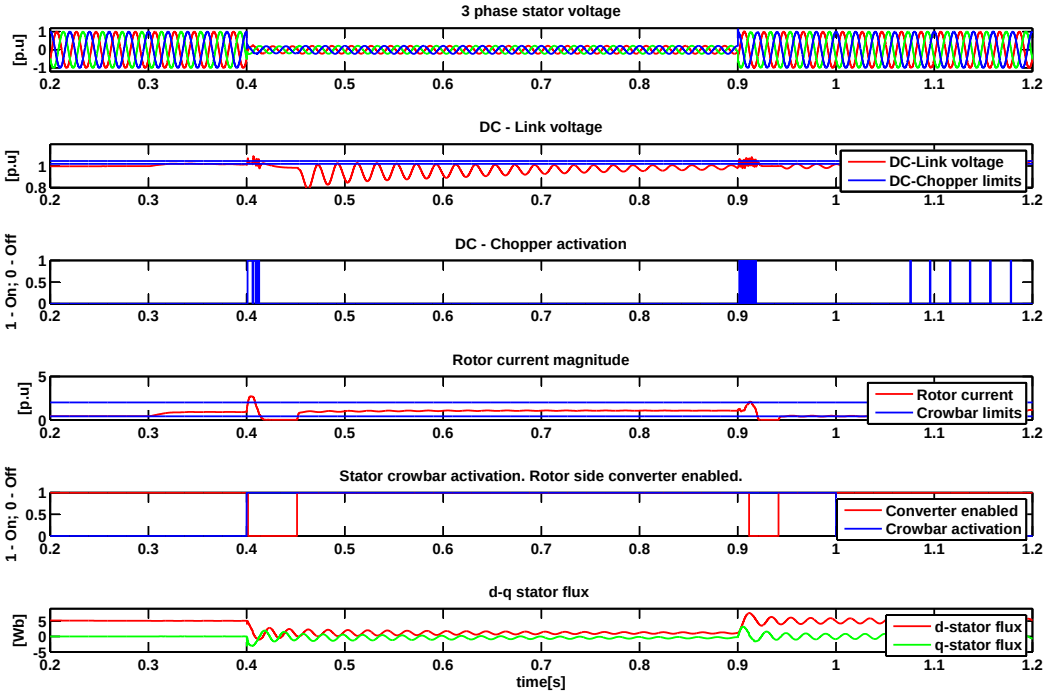


Figure 5.14: Instantaneous measurements for DFIG experiencing a 80% voltage sag. Stator Crowbar. Full disturbance compensation method. Appendix F.15.

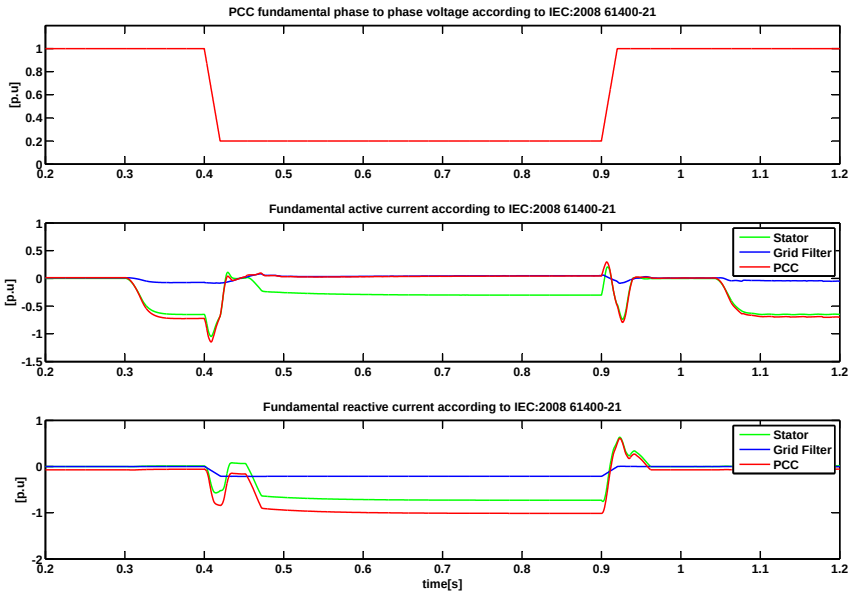


Figure 5.15: Fundamental quantities according to IEC:2008 61400-21 for DFIG experiencing a 80% voltage sag. Stator Crowbar. Full disturbance compensation method. Appendix F.14

The inverter is coasted twice, once at the beginning of the fault and once at the moment of clearing to avoid the overcurrents, but as it can be seen in Figure 5.15

this doesn't affect the generation of reactive current. The value at the PCC reaches 1 p.u. of reactive current, as requested, in less than 100 ms fulfilling the grid codes requirements.

Oscillations in DC-Link can also be observed, but not of such high amplitude as before. The DC-Chopper is only activated several times at the beginning and clearing of the fault.

### 5.3.4 Method 4: Stator Crowbar. Partial disturbance compensation with improved flux damping

The same stator crowbar system presented above is used in the present test scenario in addition to the partial disturbance compensation with improved flux damping FRT control strategy.

The results presented in Figure 5.16 and Figure 5.17 preserve pattern of results yield by this control strategy. The stator flux is significantly damped and the rotor current response is also improved.

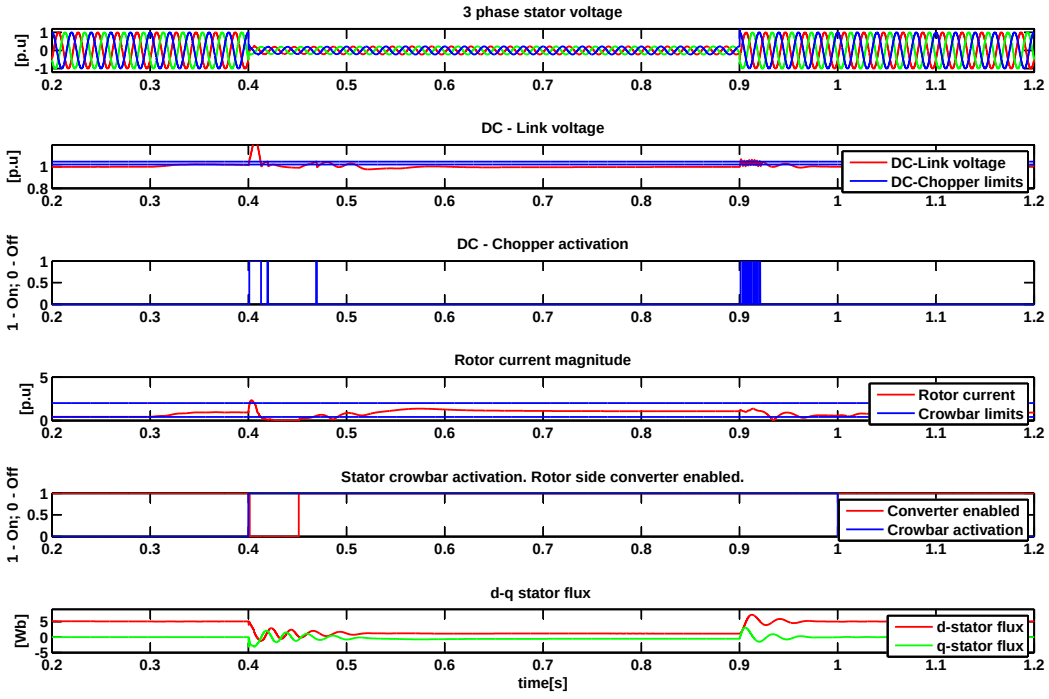


Figure 5.16: Instantaneous measurements for DFIG experiencing a 80% voltage sag. Stator Crowbar. Partial disturbance compensation with improved flux damping method. Appendix F.17.

It can be seen that only the current spike at the inception of the fault disables the inverter, while the second one is kept between safety limits by the controller. The DC-Link has a stable behavior, triggering only several DC-Chopper activations.

Even though the system behavior is more stable using this strategy, the reactive current injection is delayed and the current reaches 1 p.u. only after 200 ms.

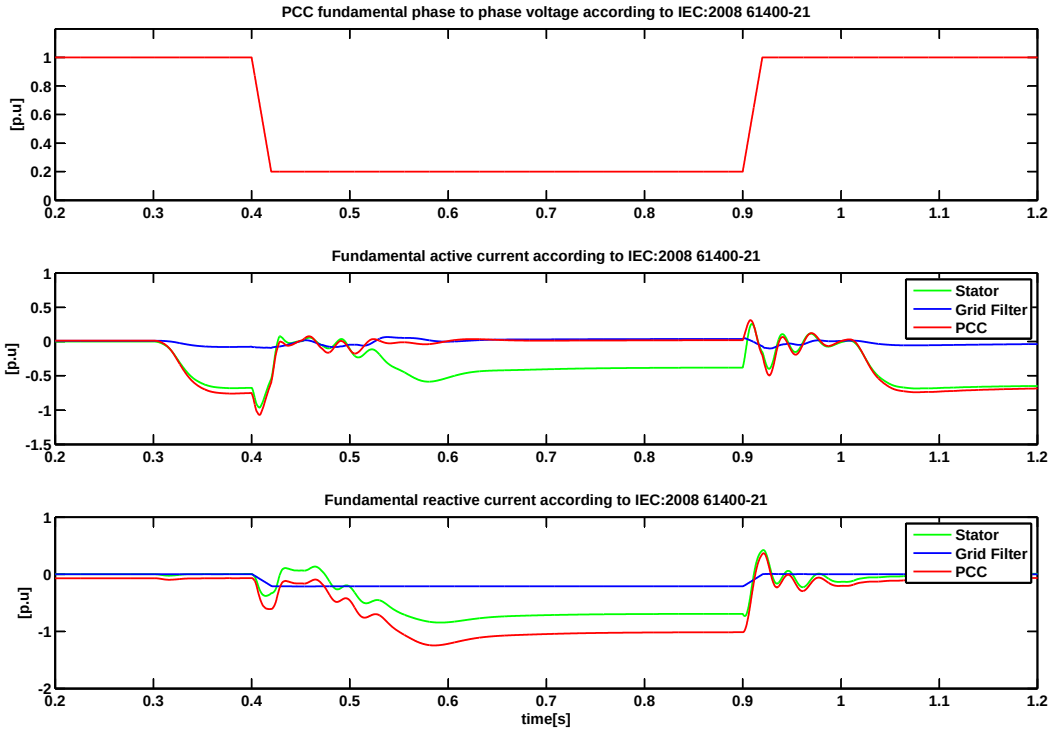


Figure 5.17: Fundamental quantities according to IEC:2008 61400-21 for DFIG experiencing a 80% voltage sag. Stator Crowbar. Partial disturbance compensation with improved flux damping method. Appendix F.16.

Analyzing the overall performance of the systems having the crowbar mounted on the stator it can be concluded that they perform better than the rotor-mounted ones, from both structural and network point of view. However the economic feasibility of these systems is questionable at the present moment. The switches that connect the stator crowbar are under continuous stress and represent a fissure in the overall robustness. Also, as mentioned in Chapter 3, conduction losses of the bidirectional switches during normal operation is another aspect that maintain this topology at a theoretical level.

# Chapter 6

# Laboratory setup

In order to provide further evidence for the concepts described in the previous chapters a laboratory-size experimental setup was put together. Details about the used components and the applied laboratory methodology can be found through out the present chapter. The chapter is divided in two sections as it can be seen in the following. The first one presents the test setup used for implementing and testing the normal operation control of the DFIG, while the second briefly approaches test scenarios related to FRT operation.

## 6.1 Normal operation test setup

The final, main test setup is presented in Figure 6.1 and it is built around two DFIG machines, one acting as the generator of the WT, while the other is used as a squirrel cage motor, emulating the aerodynamic system. This laboratory-size experimental setup was assembled in order to implement and test the normal operation and control of the DFIG.

Putting together the final test-setup was no easy task and implied identification, calibration and testing of each used component. Some unexpected behavior from some of the components made the laboratory work even more cumbersome and time consuming.

The data acquisition and control system chosen for driving the setup is a modular DS1006 real-time processor board. This processor board represents the core of dSpaces modular hardware. It provides the computing power for the real-time system and also functions as an interface to the I/O boards and the host PC. The advantages of using dSpace for system prototyping are numerous and well known. The direct interface with Simulink and Real Time Workshop together with Control-Desk for monitoring purposes offer a fast and out of the box solution for implementing real-time control solutions.

In order to fit the requirements of the real-time system, the core system was further extended with a DS2004 High-Speed A/D Board, a DS2001 D/A Board, a DS3001 Incremental Encoder Board, and a DS5101 Digital Waveform Output Board equipped with an IPC2 Optical Interface.

The default dSpace system is equipped with a DS2002 Multi-Channel A/D Board for data acquisition. This board offers 32 input channels driven by 2 independent A/D converters, 16 multiplexed inputs for each converter. Even though it offers a large number of input channels, the slow conversion time and the sample-time triggered acquisition make this default board not suitable for PWM driven applications.

Moreover, the DFIG machine used in this project presented high capacitive windings that generated current oscillations at the switching instants of the converter. This particular behavior required for a fast data acquisition board that can trigger the reading at every sample period before the current transients appear.

Under these circumstances the DS2002 was replaced with the DS2004. DS2004 offers only 16 input channels, but each of these channels have an independent A/D converter with a resolution of 16 bits and differential inputs. The conversion time is considerably reduced - 800 ns compared with 66.9 $\mu$s for the DS2002. The fast conversion times together with the 4 external trigger inputs made this board a valid candidate to fulfill the afore mentioned requirements.

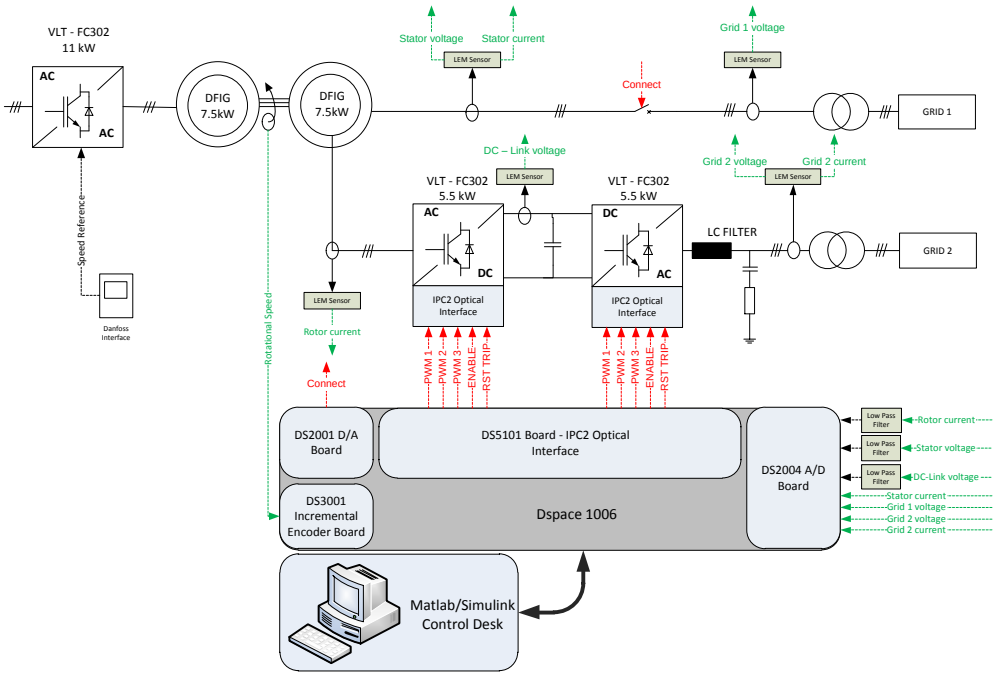


Figure 6.1: Laboratory setup used for testing the normal operation control of the DFIG

As stated before, in order to surpass the sampling problems generated by the capacitive behavior of the DFIG, the acquisition process had to be triggered before the establishment of current transients. To achieve this, the IPC2 optical interface of the DS5101 was altered so that access was gained to the clock signal of the PWM modules that control the two inverters. Then the acquisition was synchronized with the rising front of the clock signal of the DS5101 board used for PWM control of

the two converters.

Using this method for the data acquisition improved significantly the quality of the signals used in the control system as it can be seen in Figure 6.2. To improve the quality of these signals even more, filters have been mounted on some of the measuring channels as it can be observed in Figure 6.1. These 2.5 kHz low pass filters have been designed so that they reject the high frequency noise present in the measuring cables and they don't interfere with the control loops designed with lower bandwidths, as presented in Chapter 4.

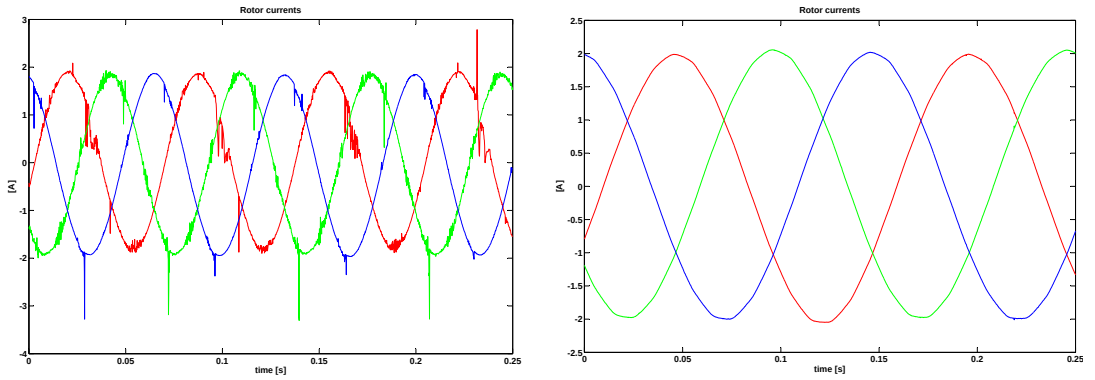


(a) Sampled rotor currents using the DS2002 Multi-Channel A/D Board

(b) Sampled rotor currents using the DS2004 High-Speed A/D Board

Figure 6.2: Comparison of sampled DFIG rotor currents using DS2002 and DS2004 as acquisition boards.

An overview of the main components used in the final laboratory setup is presented bellow:

- Real-time system:
  - a three pole pairs DFIG machine; its rotor is short-circuited thus acting as a squirrel cage machine; the data and parameters for this machine are presented in Appendix C.3.
  - a 2R12500 Scancon encoder, used for reading the electrical position of the motor.
  - an 11kW FC302 Danfoss frequency converter used to control the speed of the motor.The speed is prescribed through the interface of the inverter after providing the required motor parameters.
  - two 5.5kW FC302 Danfoss frequency converters, back-to-back configuration, used to control the generator. IPC2 optical interfaces have been mounted on both converters.
  - a two pole pairs DFIG, having its shaft connected with the squirrel cage motor. The parameters for this machine are also given in Appendix C.2.
  - 8 LEM current sensors.
  - 8 LEM voltage sensors.

  - a high power mechanical relay used for connecting and disconnecting the stator to the grid.
  - a low power solid state relay used for controlling the high power relay.

- Data aquistion and control:

  - a computer where Matlab, Simulink and Control Desk, an experiment software which provides all the functions for controlling and monitoring real-time experiments through the dSpace board, are installed.
  - a modular DS1006 real-time processor board - provides the computing power for the real-time system and also functions as an interface to the I/O boards and the host PC.
  - a DS2004 High-Speed A/D Board - serves as data acquisition system. The output from the 16 LEM sensors are connected to this board.
  - a DS2001 D/A Board - controls the low power relay that connects the stator to the grid.
  - a DS3001 Incremental Encoder Board - serves as input for the rotational speed of the shaft. The output of the encoder is connected to this board.
  - a DS5101 Digital Waveform Output Board, equipped with an IPC2 Optical Interface - controls the two back-to-back converters.

The limited number of input channels on the DS2004 board did not allow measurement of all the required signals. In some cases two phases were measured and one was estimated based on the measured ones in order to from a 3 phase signal. The LEM sensors and input channels were distribute as follows:

- 3 for measuring the 3 phase voltage on the grid connected to the stator, one for each phase of the signal,
- 2 for the 3 phase voltage on the stator,
- 2 for the 3 phase currents in the stator,
- 3 for the 3 phase currents in the rotor,
- 1 for the DC-Link voltage,
- 2 for the 3 phase voltage on the grid connected to the filter,
- 3 for the 3 phase filter currents.

As it can be seen above, priority in measurement accuracy was given to the quantities that were used in control loops, such as rotor and grid filter currents.

Another aspect that can be seen in Figure 6.1 is that the stator connects to the grid through a relay activated by the DS2001 D/A board. It has to be noted that the DS2001 does not have enough output power to control a high power mechanical

relay. In order to surpass this, a driving circuit composed of EDR101A500 was used.

The choice of connecting the stator and the rotor to the grid by means of two transformers and two isolated grids was made having in mind that only aspects related to the rotor side converter control were going to be covered in the laboratory analysis of fault ride through operation and control. In this case, modifying the setup to a FRT-testing platform will only imply changing the connection of the stator from the grid to a voltage sag generator as it will be seen in the following section.

## 6.2 Fault operation test setup

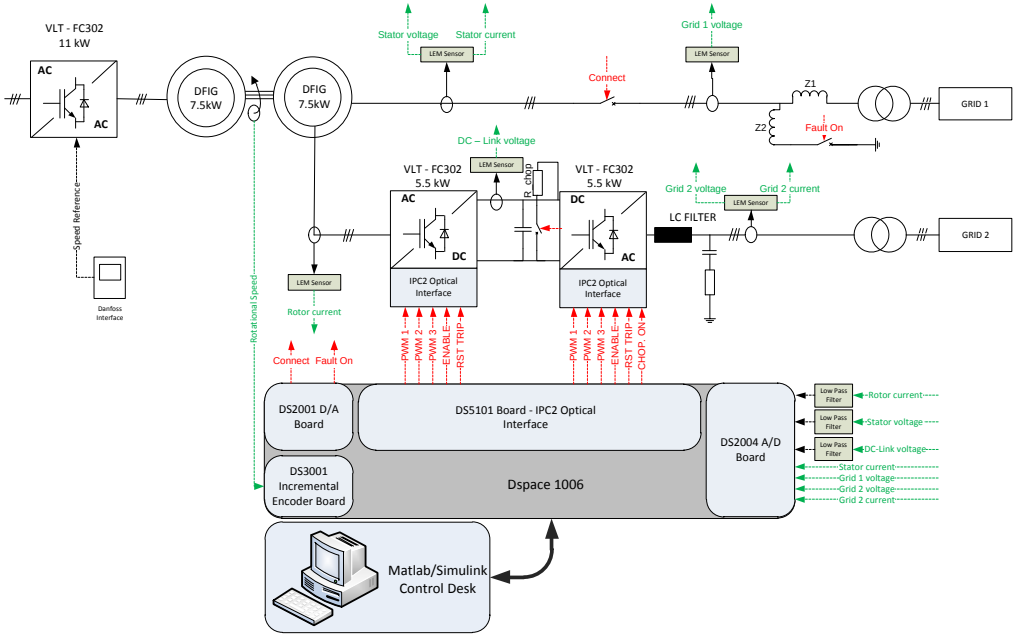


Figure 6.3: Laboratory setup used for testing the fault operation control of the DFIG

Figure 6.3 presents the modifications applied to the initial setup in order to adapt it for fault ride through tests. As it can be seen above, a simple voltage divider composed of two variable inductances has been added between the stator and the grid. The voltage divider is activated by the DS2001 using a high power mechanical relay and a EDR101A500 in the same manner that the stator is connected to the grid.

The values for the inductances used in the voltage divider were calculated in relation with the amplitude of the necessary voltage dip so that the currents flowing through the inductances don't surpass the rated value.

As protection mechanism, the DC-Chopper was connected to the DC-Brake input

of the grid side converter. An extra optical cable was set between the DS5001 and the grid side converter for controlling the activation of the DC-Chopper. The chopper was mounted on the grid side converter and not on the rotor side because the RSC could get disabled during the fault.

# Chapter 7

# Experimental results

Detailed simulation results from a full scale system were presented in the previous chapter. One of the identified limitations of the project was that experimental validation of the proposed strategies can only be provided by using a laboratory size experimental setup as presented in Chapter 6. The current chapter presents and analyzes the obtained experimental results.

## 7.1 Current control

The chapter is organized in such a manner that it follows the work flow applied when developing the control structure on the real-time system. Firstly the proper functionality of the current controllers for the rotor side converter is tested. Figure 7.1 shows the step response of the current controllers for the two axis. The first two graphs show the response of the d-axis controller when a 0.5 A step is applied as reference while the last two show the q-axis response when the same change is applied at the input.

It can be observed that even though the control signals in the d-q reference frame present high frequency noise the control structure is robust enough to handle them, and the reference is followed as requested. Several explanations can be found for the noise present in the d-q rotor current. The 2.5 kHz low-pass filter present on the measuring channel can introduce some sampling noise by delaying the input signal. Imperfections from the mechanical position reading and PLL errors can also be reflected as perturbations on the d-q axis signals.

Further improvements on the control signals in the d-q reference frame can be done by introducing filters and by fine-tuning of parameters. However this topic was not treated exhaustively and the results presented bellow were considered satisfactory for the conducted study.

After the current control of the rotor side converter was accomplished, the same methodology was applied for the grid side converter. After connecting a DC voltage source to ensure constant voltage in the DC-Link, the response of the two current

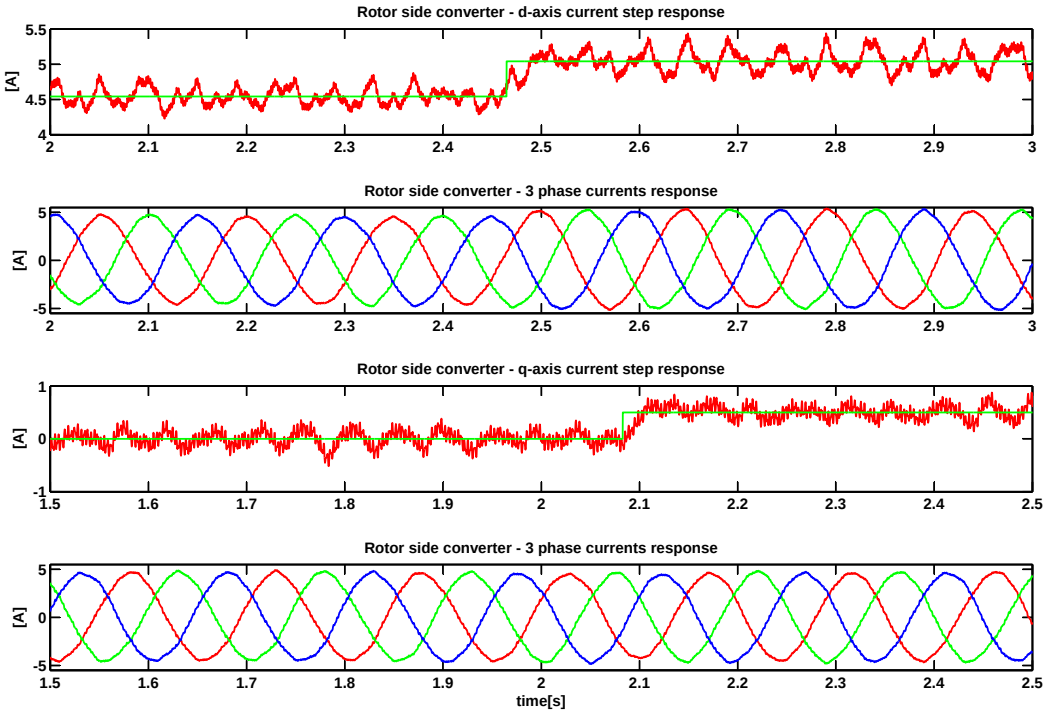


Figure 7.1: Rotor side converter - current step response. A detailed view of this graph can be observed in Figure F.18.

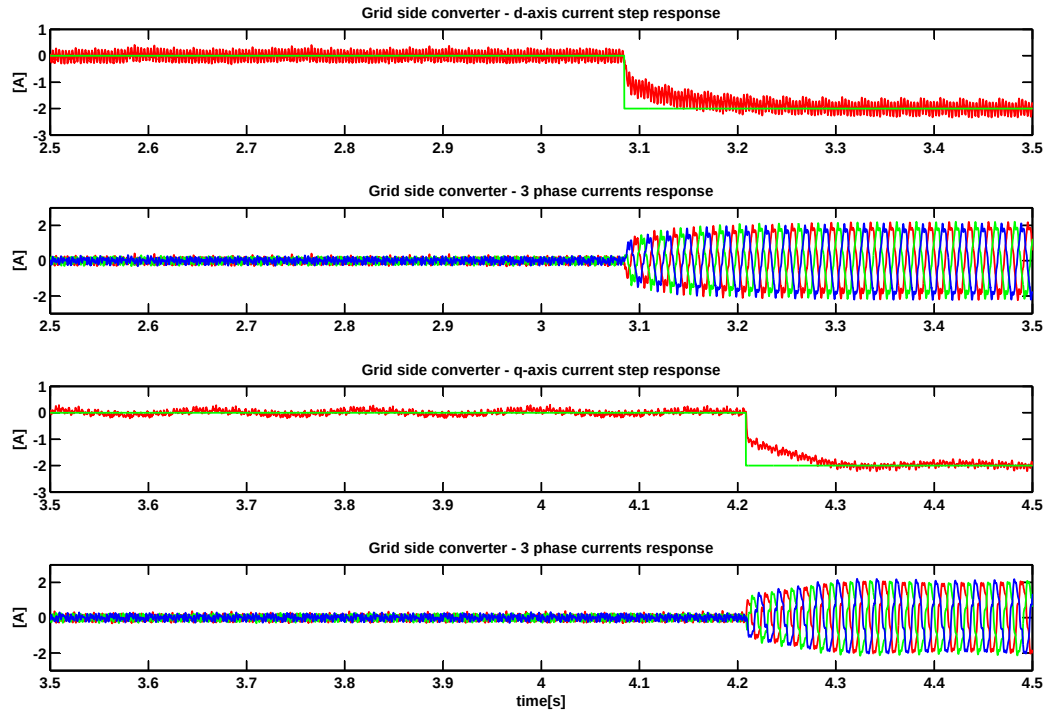


Figure 7.2: Grid side converter - current step response. A detailed view of this graph can be observed in Figure F.19.

controllers was tested by changing the reference from 0 to 2A. The results of this experiment are presented in Figure 7.2; the first two graphs show the response on the d-axis and the last two show the behavior of the q-axis.

Once again, high frequency noise, typical for real systems, can be observed on the d-q axis control signals. Also in this case, the controller is design with enough robustness so that it can manage such signals, and the reference is followed as prescribed.

It can be observed that the control signals in the natural reference frame are not sinusoidal, as expected. The existing current ripple is due to the improper design of the grid-side LCL filter. Components required for building a filter designed specifically for the laboratory setup were not available at the moment the experiment was performed.

## 7.2 DC-Link control

Having the inner current loop working, the grid side DC-Link controller was designed next. Figure 7.3 shows the stabilization of the DC-Link voltage when the controller is activated and how this influences the active current reference on the grid side converter.

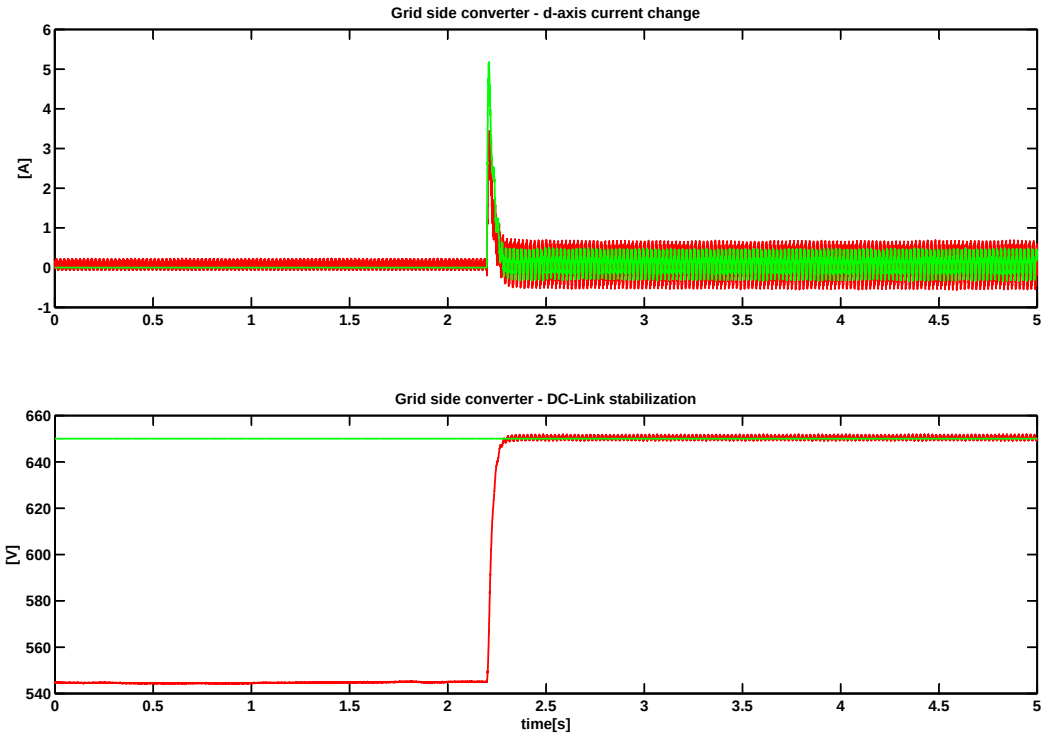


Figure 7.3: Grid side converter - DC-Link stabilization. A detailed view of this graph can be observed in Figure F.20

Noise reflected from the the DC-Link voltage into the d-axis current can be ob-

served. This DC-Link ripple contains the typical 300Hz component due to the diode rectifier, but also some other lower frequency components. One theory about the source of these lower frequency components can be formulated in the usage of a damped capacitor in the grid side filter. The partially filtered voltage acts like a perturbation, being injected into the system by the PLL.

## 7.3 Synchronization

After both the converters had the current controllers in place, and the DC-Link voltage was maintained stable by the DC-Link controller, the *Synchronization* operating mode was implemented. The response of the main quantities of interest when analyzing this operating mode are presented in Figure 7.4.

The first two graphs in Figure 7.4 show the response of the rotor current during the *Synchronization* stage both in the d-q and natural reference frames. Only the d-axis rotor is of interest in this, the q-axis being maintained to zero as displayed in Chapter 4, equation (4.6).

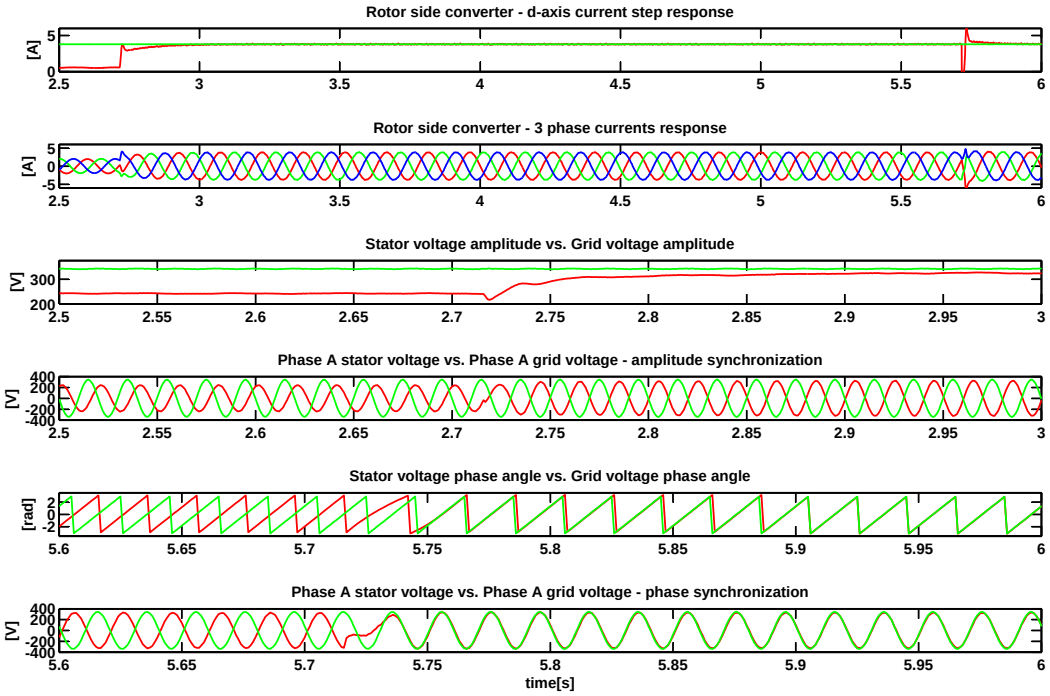


Figure 7.4: *Synchronization* operating mode. A detailed view of this graph can be observed in Figure F.21.

The control structure implemented for the laboratory system was modified so that the *Initial rotor position* operating mode is integrated with the *Synchronization* operating mode. This new operating mode is composed of two phases. In the first one the amplitude of the stator voltage is regulated to the one of the grid voltage,

while during the second the angle difference between the two voltages is identified and added as an offset to the value provided by the encoder.

On the graphs presented in Figure 7.4 the *Synchronization* operating mode was triggered after 2.7 seconds of running. The duration of this stage is controlled by the high level controller and it was set to 3 seconds, being influenced by the duration of the amplitude correction stage and the duration of the phase correction stage.

A detailed view of the amplitude correction stage can be observed in graph 3 and 4 of Figure 7.4, while graphs 5 and 6 present the phase synchronization stage.Everything being taken into account, at the end of this operating mode the initial rotor position is identified, the stator voltage is synchronized with the grid voltage in terms of phase and amplitude so the stator can be connected to the grid and the *Normal Operation* operating mode can commence.

## 7.4 Normal operation

Figure 7.5 presents the transition through the different operating modes of the rotor side converter controller.

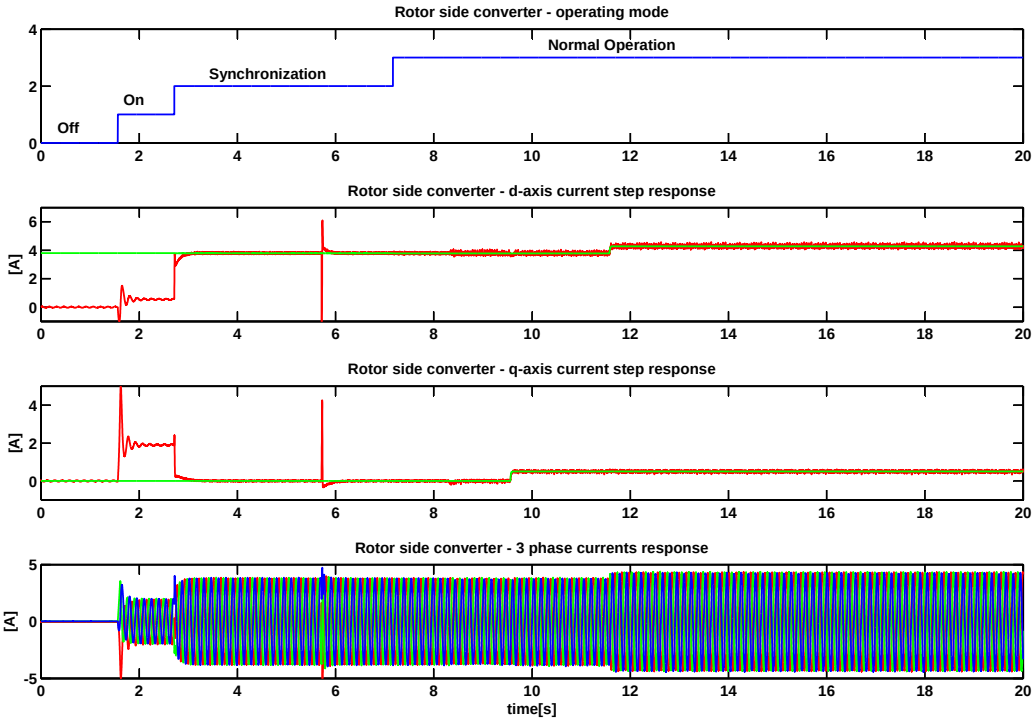


Figure 7.5: *Synchronization* operating mode followed by *Normal Operation*. A detailed view of this graph can be observed in Figure F.22.

Only the current loops have been implemented in the laboratory setup for the rotor side controller. Therefore the normal operation operating mode does not include

any new control structures that need to be validated. One aspect that has to be pointed out is that after the synchronization is reached the switch connecting the stator to the grid can be activated (in Figure 7.5 after 5.7 seconds of simulation time). After the connecting switch is on, the operating mode can be changed to *Normal Operation* (in Figure 7.5 after 7.1 seconds of simulation time).

While operating under normal conditions, with the stator connected to the grid, every change in the d-axis rotor current will imply change of reactive current between the stator and the grid, while the q-axis will generate active current flow.

## 7.5 Fault operation - Small voltage drop

After the normal operation of the laboratory setup has been validated, the setup was altered, as described in section 6.2, for fault operation tests. Only experiments involving small voltage drops were conducted due to reasons related to safety and available laboratory equipment. The results from such a study case, involving a 25% voltage sag is presented next.

Figure 7.6 displays the real flux, presented in the machine during the fault. The reduced laboratory scale DFIG presents a higher p.u. stator resistance than the full scale DFIG presented in simulations in Chapter 5. A higher stator resistance will provide better flux-damping. As it can be observed, almost no oscillations appear in the flux at the moment of fault clearing.

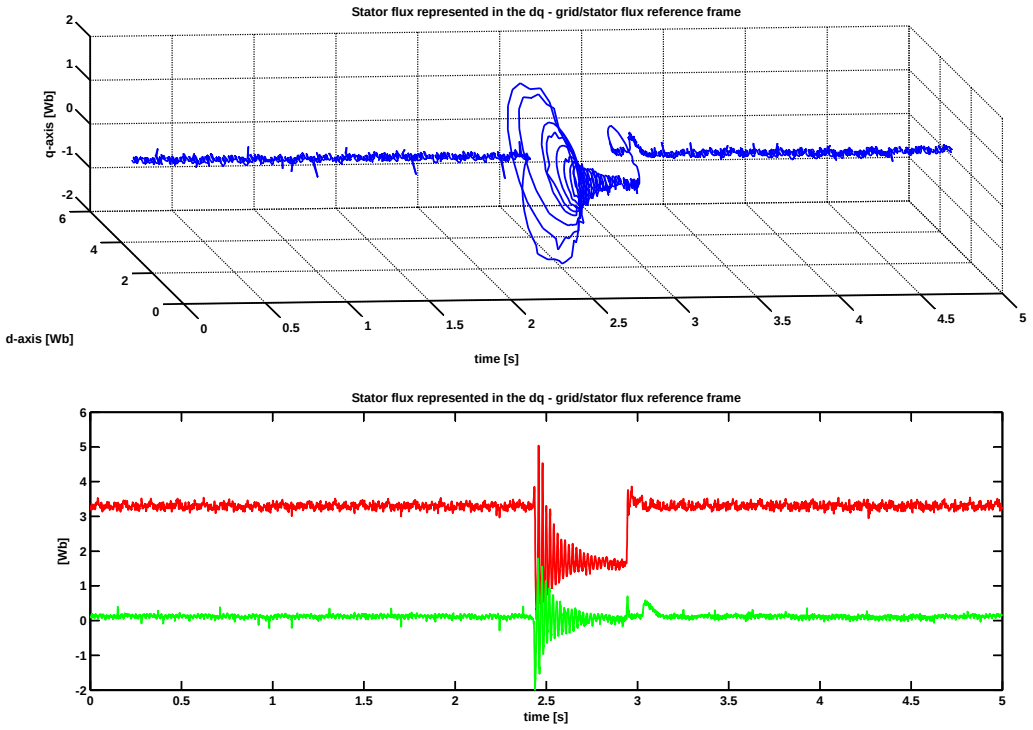


Figure 7.6: Stator flux oscillation during a 25% grid voltage drop. A detailed view of this graph can be observed in Figure F.23

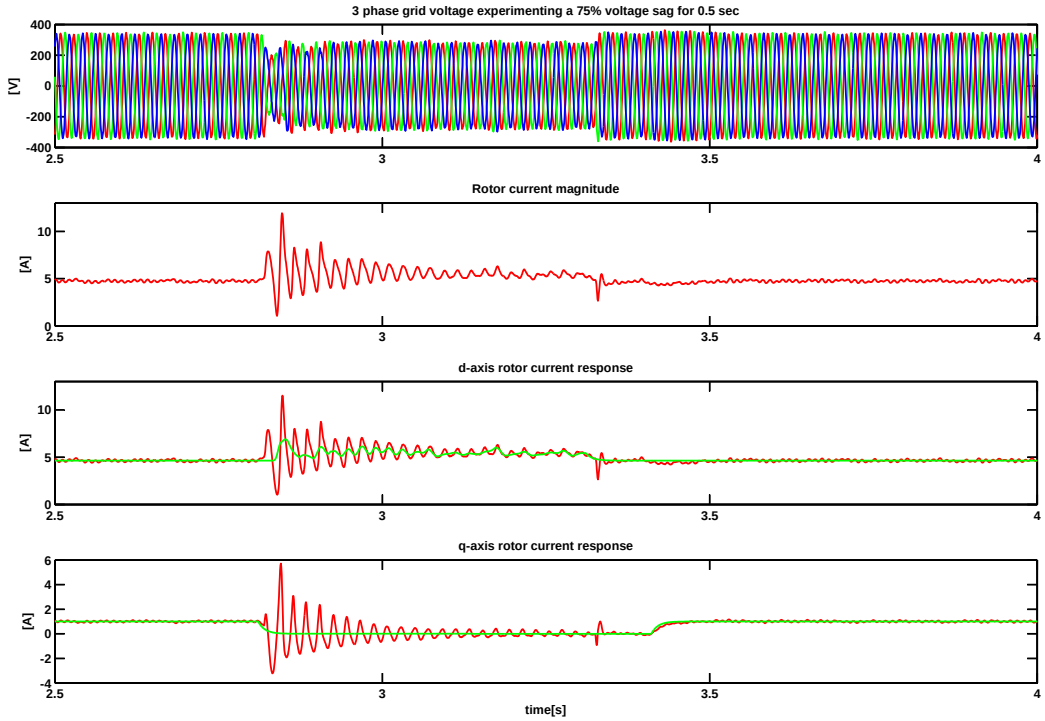


Figure 7.7: Rotor side converter - current controller behavior during a 25% grid voltage drop. A detailed view of this graph can be observed in Figure F.24

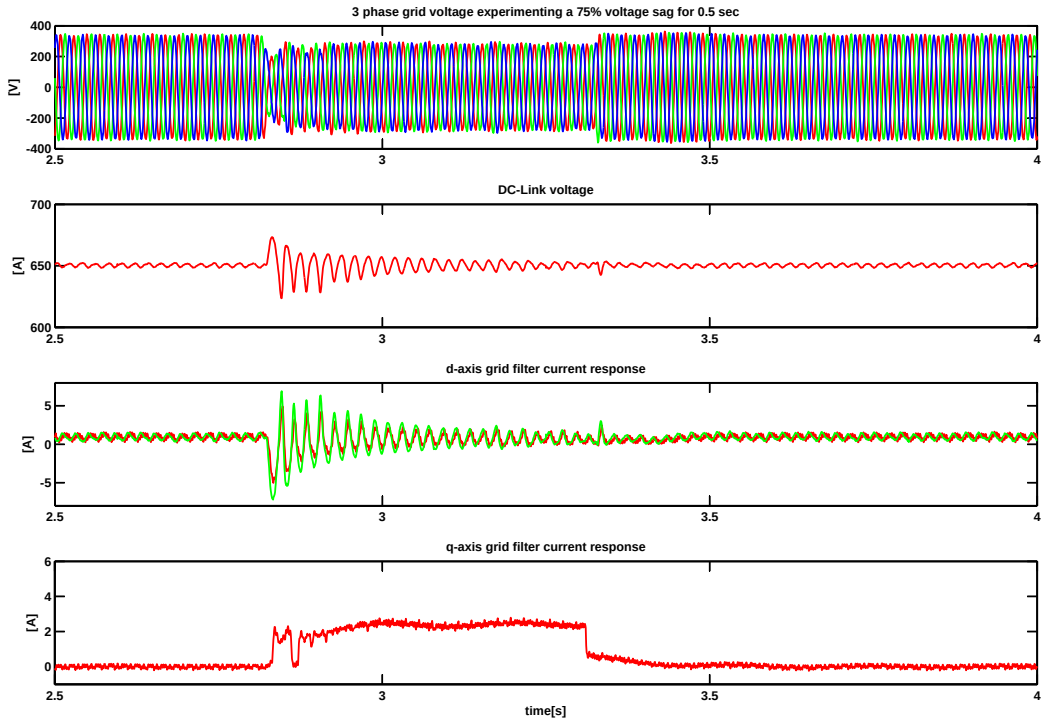


Figure 7.8: Grid side converter - current controller behavior during a 25% grid voltage drop. A detailed view of this graph can be observed in Figure F.25

Figure 7.7 and Figure 7.8 show the behavior of the rotor side and grid side current controllers.

On the rotor side, it can be seen that the active current is ramped to zero when the fault is detected and reactive current injection is started through the d-axis current. Perturbations can be observed in the reactive current reference. These are due to the fact that this reference is calculated based on the amplitude of the grid voltage. Since, as it can be seen on the first graph of Figure 7.7 and Figure 7.8, the grid voltage is unbalanced by the non symmetrical voltage sag generator the PLL coupled to the grid voltage signals will output a distorted value for the grid amplitude.

Large rotor over currents, as expected from the simulation results, can be observed at the beginning of the fault in Figure 7.7. However, their amplitude is below the tripping limits of the inverter so no disconnection occurs.

As presented in Chapter 6 the grid side converter is connected to a non faulted grid. Under these circumstances the DC-Link is perturbed only from the rotor side. As seen in Figure 7.8 the cascaded DC-Link controller rides through these perturbations maintaining the DC-Link stable while providing its share of reactive current to the grid.

The performed experiments serve as proof of concept for the developed control strategies. Nevertheless, the relevance of the presented results in conjunction with the simulations of the full scale system is limited. As previously mentioned a large DFIG will behave differently from a laboratory scale one in terms of oscillatory behavior due to the reduced stator resistance and the undamped stator flux.

# Chapter 8

# Conclusions and future work

Two methods for improving the control strategy of the rotor side converter controller were proposed, implemented and tested, namely the full disturbance compensation and the partial disturbance compensation with improved flux damping methods. Simulation results of these two strategies in conjunction with both rotor and stator crowbar full scale systems were presented in Chapter 5. Further more, experimental results from a laboratory scale system were presented and analyzed in Chapter 7.

The full disturbance compensation method implies the estimation of the disturbing terms resulting from both the rotor and stator flux induced back-e.m.f., and usage of these disturbances as feed-forward terms in the control structures. Based on the performed research and tested scenarios it can be said that this improved method of controlling the RSC provides good FRT capability. Riding through medium voltage drops without activating the crowbar and without coasting the RSC, while delivering reactive current support as requested by the grid codes, was achieved. As disadvantages for this method - the sustained oscillations in the stator flux, high rotor currents and large DC-Link fluctuations pose large mechanical and electrical stress on the WT.

The drawback of the full compensation method is that the large feed-forward terms saturate the rotor side converter and the controller can not isolate and damp the 50Hz component in the stator flux. On the other hand, the absence of the feed forward terms generates rotor over-currents that surpass the inverters safety limits at the inception of the fault. Having these two aspects in mind, the partial disturbance compensation with improved flux damping method was developed.

This control strategy tries to avoid the saturation of the rotor side converter by applying the full disturbance compensation terms only at the beginning of the fault and at the moment of fault clearing. Than the feed-forwarded terms are ramped down to zero by a decaying weighting factor. Even more, in order to focus the controller on the 50Hz component of the stator flux, notch filters are placed on the rotor current feedback loop and on the stator flux feed-forward terms. Under medium voltage drops, this strategy presented satisfactory results in terms of stress inflicted to the electric and mechanical components of the WT.

The shortcomings of this method rely on the fact that the notch filter delays the

reaction time of the current controller. As a result, the delivery of the reactive current injection is slowed down. The overall results regarding these aspects being nonetheless in the close vicinity of the limits imposed by the grid codes.

Low voltage ride through was not possible by just using improved control strategies. Crowbar triggering was necessary in both cases and the delivery of reactive current to the grid became even more challenging.

For rotor crowbar systems under low voltage drops the full disturbance compensation method provided acceptable results in terms of reactive current support, getting close to fulfilling the grid code requirements. Only one crowbar activation at the beginning of the fault was necessary in order to ride through a 80% voltage drop. The second current spike occurring at the end of the fault was avoided by just coasting the converter. The previously mentioned problems regarding the undamped stator flux, oscillatory DC-Link and rotor currents are amplified during a low voltage sag so the overall performance of the method is debatable.

The partial disturbance compensation maintains its advantages under low voltage drops. The stator flux is actively damped and the other signals have a less aggressive behavior than in the case of full disturbance compensation. But not only the advantages are preserved. The reactive current injection is delayed, in this case seriously over passing the limits imposed by the grid codes. Under low voltage conditions this method presents another major disadvantage. The RSC controller can not regain control after the fault clears without a second crowbar activation. Therefore at the moment of fault clearing the generator consumes reactive current which is not acceptable from a network stability perspective.

A stator crowbar system works on the idea of increasing the stator resistance during the fault, thus providing a passive damping of the stator flux and a better transient response of the system during faults. The major advantage of this topology is that during crowbar activation control of the rotor currents is maintained for a longer period, thus the RSC can assist the flux damping and provide reactive current to the grid. Furthermore the rotor winding is not short-circuited as in the rotor crowbar topology. Under these circumstances, the stator crowbar systems have a better chance of riding through low voltage drops and fulfilling the requirements of the grid codes.

The presented results show that the proposed control strategies also improve the fault ride through capability of the stator-crowbar systems. The reactive current support during fault is provided as requested, while the oscillations and the stress inflicted on the system are reduced.

As it can be inferred from the presented conclusions, neither one of the two proposed control strategies solve completely the problem of DFIG experiencing fault conditions. An improved solution, combining the effect of the two afore mentioned strategies has to be further investigated.

The introductory chapter defined the limitations considered for the current project. Extending these boundaries will raise new challenges to the proposed control strategies. Redesign of the control structures would be needed in order to ensure FRT for unsymmetrical faults. Also, aspects related to the control of the grid side converter under fault conditions have to be considered in the experimental

work performed in the future.

Furthermore, additional experimental validation of the presented concepts is needed. Improvements of the laboratory setup can be achieved by further filtering and processing the control signals. Also, a small scale generator with behavior similar to a full scale machine, and with less capacitive rotor windings should replace the actual machine. Another aspect of the experimental setup that needs to be polished is the used voltage sag generator. A proper grid-simulator should be used in order to emulate a realistic voltage drop.

# Bibliography


[1] Gabriele Michalke Anca D. Hansen. Fault ride-through capability of dfig wind turbines. *Renewable Energy*, 22, October 2006.

[2] The European Wind Energy Association. Wind energy - the facts. volume 1, December 2009. `http://www.ewea.org`.

[3] The European Wind Energy Association. Wind energy - the facts. volume 5, December 2009. `http://www.ewea.org`.

[4] The European Wind Energy Association. Gwec - table and statistics 2009, December 2010. `http://www.ewea.org`.

[5] F. Blaabjerg. Overview of Control and Grid Synchronization for Distributed Power Generation Systems. *IEEE Transactions on Industrial Electronics*, 15(5):1601–1409, October 2006.

[6] Andreas Dittrich and Alexander Stoev. Comparison of Fault Ride-Through Strategies for Wind Turbines with DFIM Generators. In *EPE 2005 Dresden*, pages 1–8, Dresden, 2005.

[7] I Erlich, H Wrede, and C Feltes. Dynamic Behavior of DFIG-Based Wind Turbines during Grid Faults. *Structure*, pages 1195–1200, 2007.

[8] Istvan Erlich, Senior Member, Jörg Kretschmann, Jens Fortmann, Stephan Mueller-engelhardt, and Holger Wrede. Modelling of Wind Turbines Based on Doubly-Fed Induction Generators for Power System Stability Studies. *Power*, 22(3):909–919, 2007.

[9] C Feltes, Student Member, S Engelhardt, J Kretschmann, J Fortmann, I Erlich, and Senior Member. Dynamic Performance Evaluation of DFIG- based Wind Turbines regarding new German Grid Code Requirements, 2010.

[10] Poul Sørensen Nicolaos Antonio Cutululis Florin Iov, Anca Daniela Hansen. Mapping of grid faults and grid codes. *Riso-R-1617(EN)*, January 2010.

[11] Mikel Telleria Gerardo Tapia, Giovanna Santamaria and Ana Susperregui. Methodology for smooth connection of doubly fed induction generators to the grid. *IEEE*, December 2009.

[12] Anca Hansen, Frede Blaabjerg, Poul Sorensen, and Florin Iov. Control of variable speed wind turbines with doubly-fed induction generators. *Wind Engineering*, 28(4):411–432, July 2009.

[13] B. Hopfensperger and R. A. Lakin. Stator-flux-oriented control of a doubly-fed induction machine with and without position encoder. *IEE Proceedings - Electric Power Applications*, 147(4):241–250, 2000.

[14] A. H. Kasem and M. A. A. Wahab. An improved fault ride-through strategy for doubly fed induction generator-based wind turbines. *IET Renewable Power Generation*, 2(4):201 – 214, 2008.

[15] Marian Kazmierkowski and Henryk Tunia. *Automatic control of converter-fed drives*. Elsevier, 1994.

[16] Francisco K A Lima, Alvaro Luna, Pedro Rodriguez, Edson H Watanabe, and Frede Blaabjerg. Rotor Voltage Dynamics in the Doubly Fed Induction Generator During Grid Faults. *IEEE Transactions on Power Electronics*, 25(1):118–130, 2010.

[17] M. Liserre, F. Blaabjerg, and S. Hansen. Design and Control of an LCL-Filter-Based Three-Phase Active Rectifier. *IEEE Transactions on Industry Applications*, 41(5):1281–1291, September 2005.

[18] A. Luna, A. Rolan, G. Medeiros, P. Rodriguez, and R. Teodorescu. Control Strategies for DFIG Wind Turbines Under Grid Fault Conditions, 2009.

[19] S. Muller and M. Deike. Doubly fed induction generator systems for wind turbines, 2002.

[20] J. Bergas I. Candela R. Burgos D. Boroyevich P. Rodriguez, J. Pou. Double synchronous reference frame pll for power converters control. *IEEE*, June 2005.

[21] R. Pena, J. C. Clare, and G.M. Asher. Doubly fed induction generator using back-to-back PWM converters and its application to variable-speed wind-energy generation. *IEE Proceedings - Electric Power Applications*, 143(3):231, 1996.

[22] Andreas Petersson. *Analysis , Modelling and Control of Doubly-Fed Induction Generators for Wind Turbines*. PhD thesis, Chalmers University of Technology, 2005.

[23] M. Rahimi and M. Paniani. Eficient control scheme of wind turbines with doubly fed induction generators for low-voltage ride-through capability enhancement. *IET Renewable Power Generation*, 4(3):242–252, 2010.

[24] M. Rashid. *Power Electronics Handbook*. Elsevier, second edition, 2007.

[25] Miguel Rodriguez, Gonzalo Abad, Izaskun Sarasola, and Alex Gilabert. Crowbar Control Algorithms for Doubly Fed Induction Generator During Voltage Dips. In *EPE 2005 Dresden*, pages 1–10, 2005.

[26] E Tremblay, S Atayde, A Chandra, and Senior Member. Comparative study of control strategies for the Doubly Fed Induction Generator in Wind Energy Conversion Systems : a DSP-based implementation approach . *IEEE*, pages 1–13, 2011.

[27] Christian Wessels and Friedrich W Fuchs. Fault Ride Through of DFIG Wind Turbines during symmetrical voltage dip with Crowbar or Stator Current Feedback Solution. *Wind Energy*, pages 2771–2777, 2010.

[28] Erlich M. Wilch and C. Feltes. Reactive power generation by DFIG based wind farms with AC grid connection. *European Conference on Power Electronics and Applications*, pages 1–10, 2007.

[29] Lie Xu. Dynamic Modelling and Control of DFIG-Based Wind Turbines Under Unbalanced Network Conditions. *IEEE Transactions on Power Systems*, 140(1):299–323, February 2007.

# Appendix A

# Simulation plant - Parameters

## A.1 Complete plant schematic

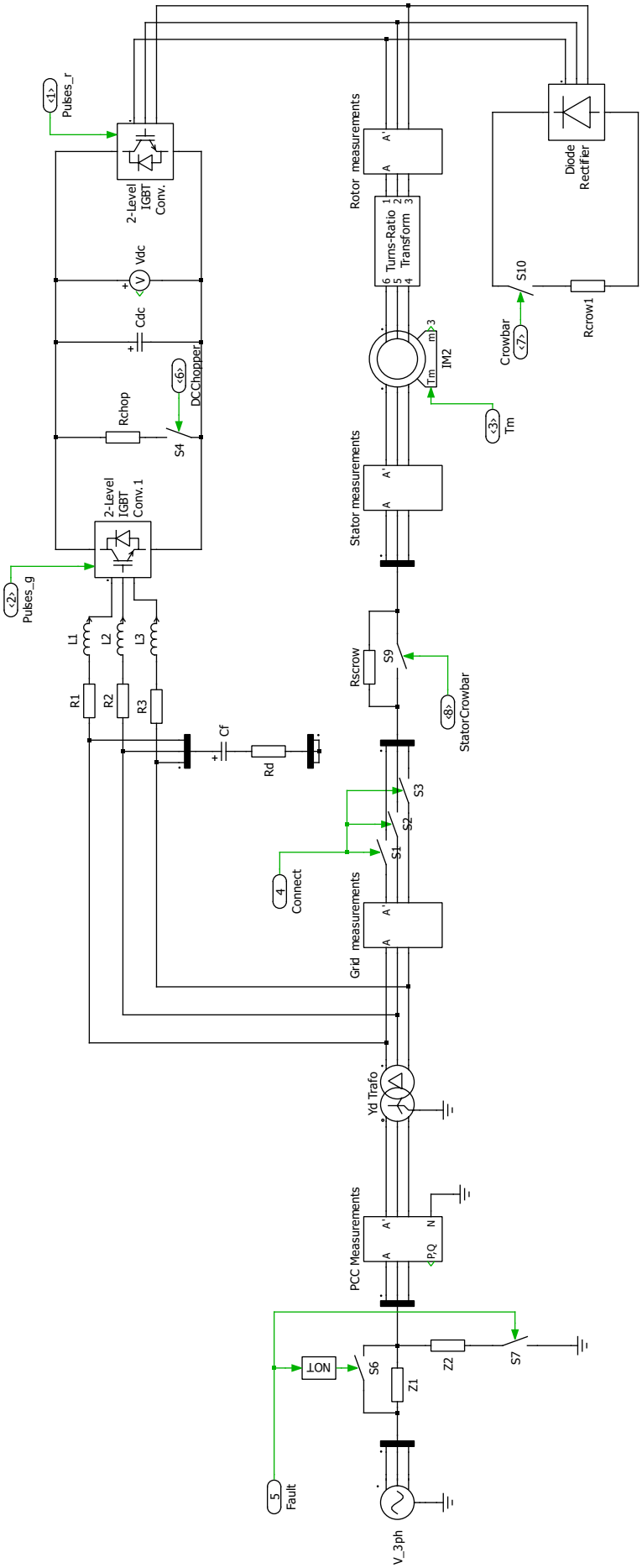


Figure A.1: Complete PLECS schematic of the plant.

## A.2 Grid transformer

Transformer rating = 2.5 MVA;
Transformer leakage inductance = 36.3 $\mu$H;
Transformer resistance = 0.0019 $\Omega$

## A.3 Doubly fed induction generator

Rated power = 2 MW;
Rated R.M.S. line-to-line voltage = 690 V;
Number of pole pairs = 2;
Stator resistance = 0.006 p.u.;
Stator leakage inductance = 0.125 p.u.;
Rotor resistance = 0.006 p.u.;
Rotor leakage inductance = 0.125 p.u.;
Magnetizing inductance = 4 p.u.;
Stator-to-rotor transfer ratio = 0.357

## A.4 Grid filter

Filter series inductance = 500 $\mu$H;
Filter parallel capacitance = 668.58 $\mu$F;
Filter parallel resistance = 0.1 $\Omega$;

## A.5 DC Link

Nominal DC Link voltage = 1100 V;
DC Link capacitor = 8 mF;

## A.6 Protection devices

DC-Chopper resistance = 1.8034 $\Omega$;
Rotor crowbar resistance = 0.9017 $\Omega$;
Stator crowbar resistance = 0.1120 $\Omega$;

# Appendix B

# Simulation controller - Parameters

Switching frequency = 5 kHz;
Sampling frequency = 5 kHz;

Table B.1: Full scale system controller parameters

| Controller | Ki | Kp |
|---|---|---|
| Synchronization | 53.77 | 3.65 |
| Rotor current | 2.21 | 0.15 |
| Stator power | 0.0713 | 3.7e-4 |
| Grid filter current | 12.91 | 0.63 |
| DC Link voltage | 0.013 | 2.3e-3 |

# Appendix C

# Experimental plant - Parameters

## C.1 Grid transformer

Transformer (stator) rating = 10 kVA;
Transformer leakage inductance = 1.5 mH;

Transformer (grid filter) rating = 5 kVA;
Transformer leakage inductance = 3.7 mH;

## C.2 Doubly fed induction machine - generator

Rated power = 7.5 kW;
Number of pole pairs = 2;
Stator resistance = 0.0261 p.u.;
Stator leakage inductance = 0.0578 p.u.;
Rotor resistance = 0.0349 p.u.;
Rotor leakage inductance = 0.0578 p.u.;
Magnetizing inductance = 1.6161 p.u.;
Stator-to-rotor transfer ratio = 0.347

## C.3 Doubly fed induction machine - motor

Rated power = 7.5 kVA;
Rated R.M.S. line-to-line voltage = 380 V;
Number of pole pairs = 3;
Stator resistance = 0.0219 p.u.;
Stator leakage inductance = 0.0932 p.u.;
Rotor resistance = 0.0366 p.u.;
Rotor leakage inductance = 0.0932 p.u.;
Magnetizing inductance = 1.5697 p.u.;
Stator-to-rotor transfer ratio = 1.31

## C.4 Grid filter

Filter series inductance = 6.3 mH;
Filter series resistance = 0.3 Ω;
Filter parallel capacitance = 4.4 $\mu$F;
Filter parallel resistance = 3.3 Ω;

## C.5 DC Link

Nominal DC Link voltage = 650 V;
DC Link capacitor = 600 $\mu$F;

## C.6 Protection devices

DC-Chopper resistance = 100 Ω;

# Appendix D

# Experimental controller - Parameters

Switching frequency = 5 kHz;
Sampling frequency = 5 kHz;

Table D.1: Laboratory system controller parameters

| Controller | Ki | Kp |
|---|---|---|
| Synchronization | 1.227e3 | 114.36 |
| Rotor current | 833.65 | 6.67 |
| Stator power | 0.0894 | 2.41e-4 |
| Grid filter current | 1.99e3 | 7.76 |
| DC Link voltage | 0.016 | 1.75e-4 |

# Appendix E

# Rotor current controller - Code listing

```
   /*  File    : RotorCurrentController_v4a.c
 *  Abstract:
 *  Rotor current controller implemented in stator flux reference
 *  using PI controllers and decoupling
 *  OP_MODE:
 *  0 - Offline
 *  1 - Initial rotor position estimation stage
 *  2 - Synchronization stage
 *  3 - Normal operation stage
 *  4 - Normal operation under fault stage
 *  5 - Fault operation stage
 */

#define S_FUNCTION_NAME RotorCurrentController_v4a
#define S_FUNCTION_LEVEL 2

//INPUTS
#define ID_E_R_REF(S) ssGetInputPortSignal(S,0)
#define ID_E_R(S) ssGetInputPortSignal(S,1)
#define IQ_E_R_REF(S) ssGetInputPortSignal(S,2)
#define IQ_E_R(S) ssGetInputPortSignal(S,3)
#define OMG_SLIP(S) ssGetInputPortSignal(S,4)
#define FLUX_D(S) ssGetInputPortSignal(S,5)
#define FLUX_Q(S) ssGetInputPortSignal(S,6)
#define DFLUX_D_DT(S) ssGetInputPortSignal(S,7)
#define DFLUX_Q_DT(S) ssGetInputPortSignal(S,8)
#define FLUX_MAG(S) ssGetInputPortSignal(S,9)
#define OP_MODE(S) ssGetInputPortSignal(S,10)

//PARAMETERS
#define P(S) ssGetSFcnParam(S,0)
#define I(S) ssGetSFcnParam(S,1)
```

```
#define Ts(S) ssGetSFcnParam(S,2)
#define LS(S) ssGetSFcnParam(S,3)
#define LR(S) ssGetSFcnParam(S,4)
#define LM(S) ssGetSFcnParam(S,5)

#include "simstruc.h"
#include <math.h>


enum EOP_MODES
{
    OFFLINE,
    INITIAL_POSITION,
    SYNCHRONIZATION,
    NORMAL_OPERATION,
    NORMAL_OPERATION_UNDER_FAULT,
    FAULT_OPERATION
};

const real_T Ud=0;
const real_T Uq=100;
const real_T COMP_MAX = 1;
const real_T COMP_DURATION = 0.2;
const real_T K_DAMP = 0;

static real_T comp_weight = 1;
static enum EOP_MODES previous_state = OFFLINE;

#define MDL_CHECK_PARAMETERS
#if defined(MDL_CHECK_PARAMETERS) && defined(MATLAB_MEX_FILE)

  static void mdlCheckParameters(SimStruct *S)
  {
      {
          if (*mxGetPr(Ts(S)) <= 0.0) {
              ssSetErrorStatus(S,"The block sample rate "
                               "must be greater than zero");
              return;
          }
      }
  }
#endif /* MDL_CHECK_PARAMETERS */

static void mdlInitializeSizes(SimStruct *S)
{
    int_T  i;

    //PARAMETERS
```

```
    ssSetNumSFcnParams(S, 6);  /* Number of expected parameters */
    #if defined(MATLAB_MEX_FILE)
    if (ssGetNumSFcnParams(S) == ssGetSFcnParamsCount(S)) {
        mdlCheckParameters(S);
        if (ssGetErrorStatus(S) != NULL) {
            return;
        }
    } else {
        return; /* Parameter mismatch will be reported by Simulink */
    }
    #endif

    //STATES
    ssSetNumContStates(S, 0);
    ssSetNumDiscStates(S, 2);

    //INPUT PORTS
    if (!ssSetNumInputPorts(S, 11)) return;

    for (i=0;i<11;i++)
    {
            ssSetInputPortWidth(S, i, 1);
            ssSetInputPortRequiredContiguous(S, i, true);
            ssSetInputPortDirectFeedThrough(S, i, 1);
    }

    // Set OP_MODE port type UINT32
    ssSetInputPortDataType(S, 10, SS_UINT32);

    //OUTPUT PORTS
    if (!ssSetNumOutputPorts(S, 4)) return;
    ssSetOutputPortWidth(S, 0, 1);
    ssSetOutputPortWidth(S, 1, 1);
    ssSetOutputPortWidth(S, 2, 1);
    ssSetOutputPortWidth(S, 3, 1);

    //OTHERS
    ssSetNumSampleTimes(S, 1);
    ssSetNumRWork(S, 0);
    ssSetNumIWork(S, 0);
    ssSetNumPWork(S, 0);
    ssSetNumModes(S, 0);
    ssSetNumNonsampledZCs(S, 0);
    ssSetSimStateCompliance(S, USE_DEFAULT_SIM_STATE);
}

static void mdlInitializeSampleTimes(SimStruct *S)
{
```

```
#ifdef  MATLAB_MEX_FILE    /* Is this file being compiled as a MEX-file? */
        ssSetSampleTime(S, 0, *mxGetPr(Ts(S)));
#else
        ssSetSampleTime(S, 0, INHERITED_SAMPLE_TIME);
#endif

}

#define MDL_INITIALIZE_CONDITIONS
static void mdlInitializeConditions(SimStruct *S)
{
    real_T *x0 = ssGetRealDiscStates(S);
    int_T  lp;

    for (lp=0;lp<2;lp++) {
        *x0++=0;
    }
}

#define MDL_START
static void mdlStart(SimStruct *S)
{
}

static void mdlOutputs(SimStruct *S, int_T tid)
{
    real_T            *vd_e_r    = ssGetOutputPortRealSignal(S,0);
    real_T            *vq_e_r    = ssGetOutputPortRealSignal(S,1);
    real_T            *x    = ssGetRealDiscStates(S);
    real_T            *x1    = ssGetOutputPortRealSignal(S,2);
    real_T            *x2    = ssGetOutputPortRealSignal(S,3);


    const real_T id_e_r_ref = *(const real_T*) ID_E_R_REF(S);
    const real_T id_e_r = *(const real_T*) ID_E_R(S);
    const real_T iq_e_r_ref = *(const real_T*) IQ_E_R_REF(S);
    const real_T iq_e_r = *(const real_T*) IQ_E_R(S);
    const real_T omg_slip = *(const real_T*) OMG_SLIP(S);
    const real_T flux_d = *(const real_T*) FLUX_D(S);
    const real_T flux_q = *(const real_T*) FLUX_Q(S);
    const real_T flux_mag = *(const real_T*) FLUX_MAG(S);
    const real_T dfid_dt = *(const real_T*) DFLUX_D_DT(S);
    const real_T dfiq_dt = *(const real_T*) DFLUX_Q_DT(S);
    const enum EOP_MODES op_mode = *(const enum EOP_MODES*) OP_MODE(S);

    const real_T *P =  (mxGetPr(P(S)));
    const real_T Ls =  *(mxGetPr(LS(S)));
```

```
    const real_T Lr =  *(mxGetPr(LR(S)));
    const real_T Lm =  *(mxGetPr(LM(S)));
    const real_T sigma =  1 - Lm*Lm/Ls/Lr;

    const real_T Ts = *mxGetPr(Ts(S));


    real_T id_error, iq_error, vd_comp, vq_comp;
    int_T controller_idx, slope = 10;
    time_T t = 0;

    real_T flux_comp=0;

    x2[0] = 0;
    switch (op_mode)
    {
        case OFFLINE:
        {
            vd_e_r[0]= 0;
            vq_e_r[0]= 0;
        }; break;
        case INITIAL_POSITION:
        {
            t = ssGetT(S);
            vd_e_r[0] = Ud;
            vq_e_r[0] = t*100<Uq?t*100:Uq;

        }; break;
        case SYNCHRONIZATION:
        {
            comp_weight = 0;
#ifdef  MATLAB_MEX_FILE    /* Is this file being compiled as a MEX-file? */
            id_error = flux_mag/Lm - id_e_r;
#else
            id_error = id_e_r_ref - id_e_r;
#endif
            iq_error = 0 - iq_e_r;

            vd_comp = -iq_e_r*omg_slip*Lr;
            vq_comp = omg_slip*id_e_r*Lr;

            //Bumpless transition
            controller_idx = 0;
            vd_e_r[0]= P[controller_idx]*id_error + x[0] + vd_comp;
            vq_e_r[0]= P[controller_idx]*iq_error + x[1] + vq_comp;
        }; break;
        case NORMAL_OPERATION:
        {
```

```
            id_error = id_e_r_ref - id_e_r;
            iq_error = iq_e_r_ref - iq_e_r;

            comp_weight -= Ts*COMP_MAX/COMP_DURATION;

            if (comp_weight <= 0)
                    comp_weight = 0;

            vd_comp = -iq_e_r*omg_slip*sigma*Lr  + comp_weight * Lm/Ls*dfid_dt
                    - omg_slip*Lm/Ls*flux_q;
            vq_comp = omg_slip*(flux_d*Lm/Ls + id_e_r*sigma*Lr)
                    + comp_weight * Lm/Ls*dfiq_dt;


            controller_idx = 1;
            vd_e_r[0]= P[controller_idx]*id_error + x[0] + vd_comp;
            vq_e_r[0]= P[controller_idx]*iq_error + x[1] + vq_comp;

        }; break;
        case NORMAL_OPERATION_UNDER_FAULT:
        {
            flux_comp = sqrt(flux_d * flux_d + flux_q * flux_q) - flux_mag;

            id_error = id_e_r_ref - id_e_r - K_DAMP*flux_comp;
            iq_error = iq_e_r_ref - iq_e_r - K_DAMP*flux_comp;

            comp_weight = 1;
            vd_comp = -iq_e_r*omg_slip*sigma*Lr - omg_slip*Lm/Ls*flux_q
                    + comp_weight * Lm/Ls*dfid_dt;
            vq_comp = omg_slip*(flux_d*Lm/Ls + id_e_r*sigma*Lr)
                    + comp_weight * Lm/Ls*dfiq_dt;


            controller_idx = 1;
            vd_e_r[0]= P[controller_idx]*id_error + x[0] + vd_comp;
            vq_e_r[0]= P[controller_idx]*iq_error + x[1] + vq_comp;
        }; break;
        case FAULT_OPERATION:
        {
            comp_weight = COMP_MAX;
            vd_e_r[0]= 0;
            vq_e_r[0]= 0;
        }; break;
        default:{};
    }
```

```
    UNUSED_ARG(tid); /* not used in single tasking mode */
}

#define MDL_UPDATE
static void mdlUpdate(SimStruct *S, int_T tid)
{
    real_T            *x       = ssGetRealDiscStates(S);
    const real_T id_e_r_ref = *(const real_T*) ID_E_R_REF(S);
    const real_T id_e_r = *(const real_T*) ID_E_R(S);
    const real_T iq_e_r_ref = *(const real_T*) IQ_E_R_REF(S);
    const real_T iq_e_r = *(const real_T*) IQ_E_R(S);
    const real_T omg_slip = *(const real_T*) OMG_SLIP(S);
    const real_T flux_d = *(const real_T*) FLUX_D(S);
    const real_T flux_q = *(const real_T*) FLUX_Q(S);
    const real_T flux_mag = *(const real_T*) FLUX_MAG(S);
    const enum EOP_MODES op_mode = *(const enum EOP_MODES*) OP_MODE(S);
    const real_T Ls =  *(mxGetPr(LS(S)));
    const real_T Lr =  *(mxGetPr(LR(S)));
    const real_T Lm =  *(mxGetPr(LM(S)));
    const real_T sigma =  1 - Lm*Lm/Ls/Lr;
    const real_T *I = mxGetPr(I(S));
    const real_T *P = mxGetPr(P(S));
    const real_T Ts = *mxGetPr(Ts(S));
    int_T controller_idx;

    real_T id_error, iq_error;
    real_T flux_comp;

     switch (op_mode)
    {
        case OFFLINE:
        {
            id_error = 0;
            iq_error = 0;
            x[0] = 0;
            x[1] = 0;
        }; break;
        case INITIAL_POSITION:
        {
            id_error = 0;
            iq_error = 0;
            x[0] = 0;
            x[1] = 0;
        }; break;
        case SYNCHRONIZATION:
        {
#ifdef  MATLAB_MEX_FILE    /* Is this file being compiled as a MEX-file? */
```

```
            id_error = flux_mag/Lm - id_e_r;
#else
            id_error = id_e_r_ref - id_e_r;
#endif
            iq_error = 0 - iq_e_r;

            controller_idx = 0;

            x[0]= I[controller_idx] * Ts * id_error + x[0];
            x[1]= I[controller_idx] * Ts * iq_error + x[1];
        }; break;
        case NORMAL_OPERATION:
        {
            id_error = id_e_r_ref - id_e_r;
            iq_error = iq_e_r_ref - iq_e_r;
            controller_idx = 1;

            x[0]= I[controller_idx] * Ts * id_error + x[0];
            x[1]= I[controller_idx] * Ts * iq_error + x[1];
        }; break;
        case NORMAL_OPERATION_UNDER_FAULT:
        {
            if (previous_state == NORMAL_OPERATION)
            {
                x[0]= 0;
                x[1]= 0;
            }

            flux_comp = sqrt(flux_d * flux_d + flux_q * flux_q) - flux_mag;

            id_error = id_e_r_ref - id_e_r - K_DAMP*flux_comp;
            iq_error = iq_e_r_ref - iq_e_r - K_DAMP*flux_comp;

            controller_idx = 1;
            x[0]= I[controller_idx] * Ts * id_error + x[0];
            x[1]= I[controller_idx] * Ts * iq_error + x[1];
        }; break;
        case FAULT_OPERATION:
        {
            x[0]= 0;
            x[1]= 0;

        }; break;
        default:{};
        previous_state = op_mode;
    }
    UNUSED_ARG(tid); /* not used in single tasking mode */
}
```

```
/* Function: mdlTerminate =====================================================
 * Abstract:
 *    No termination needed, but we are required to have this routine.
 */
static void mdlTerminate(SimStruct *S)
{
    UNUSED_ARG(S); /* unused input argument */
}

#ifdef  MATLAB_MEX_FILE    /* Is this file being compiled as a MEX-file? */
#include "simulink.c"      /* MEX-file interface mechanism */
#else
#include "cg_sfun.h"       /* Code generation registration function */
#endif
```

# Appendix F

# Detailed graphs and figures

## F.1 Simulation results

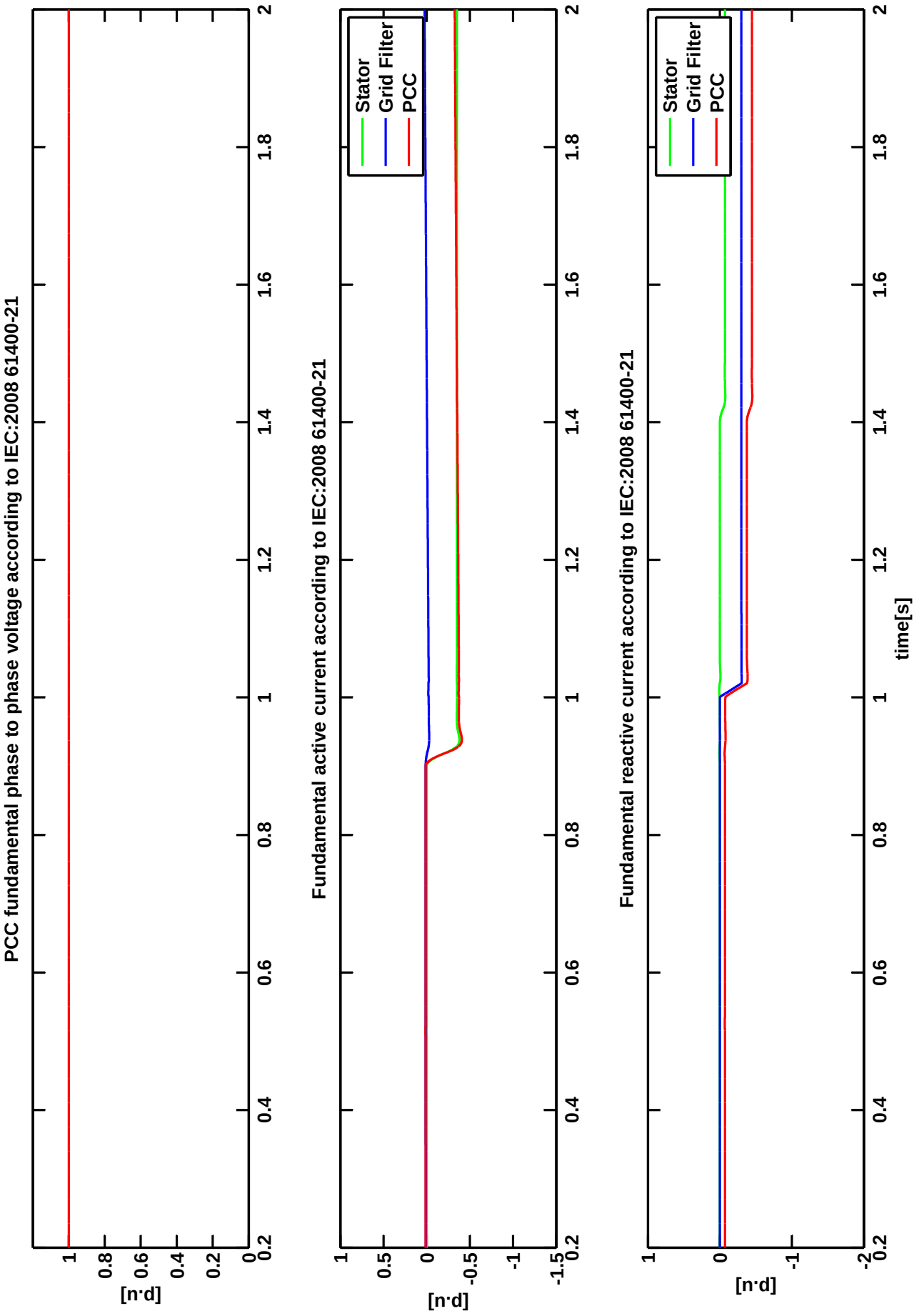


Figure F.1: Fundamental quantities according to IEC:2008 61400-21 for DFIG under normal operation.

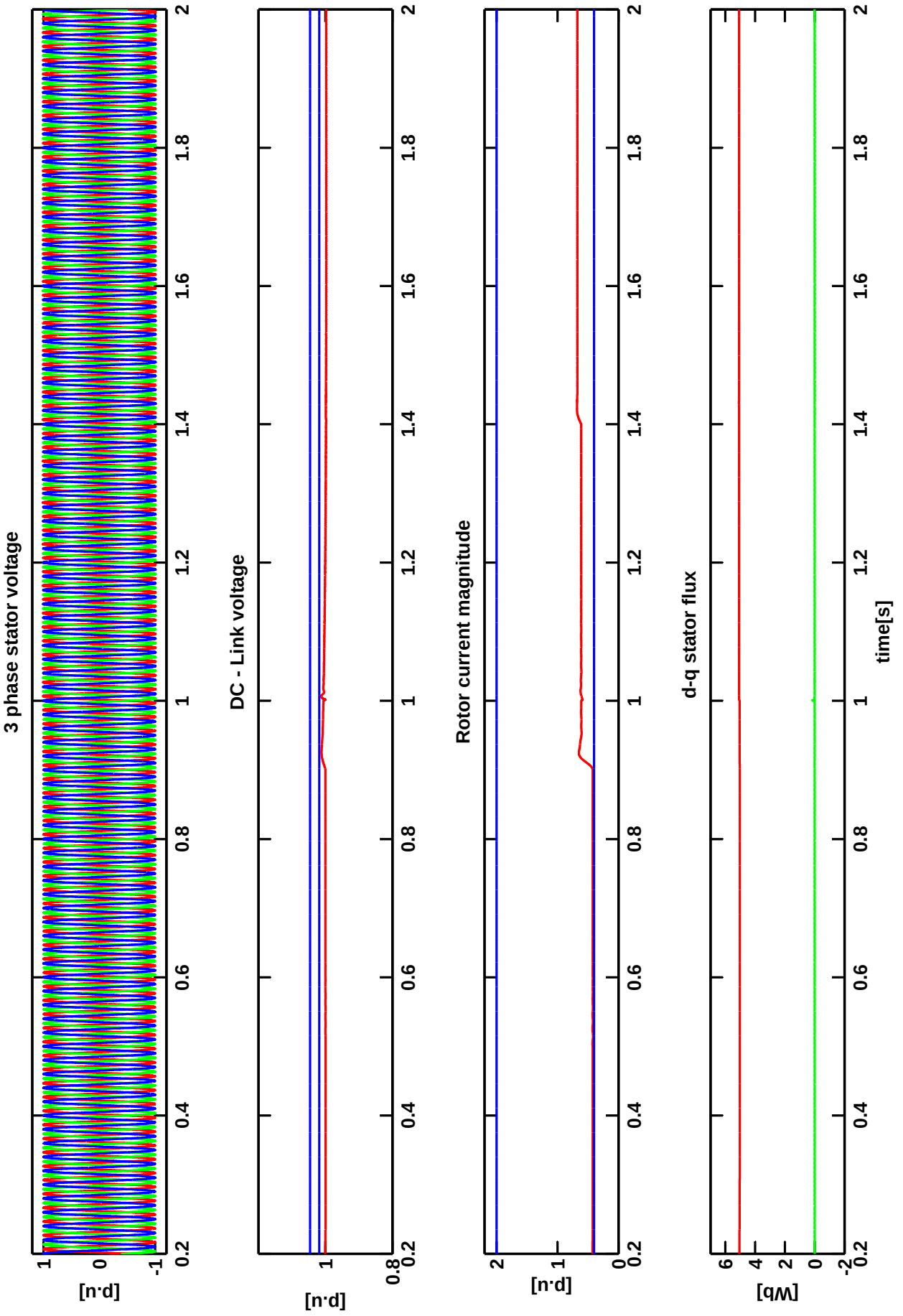


Figure F.2: Stator voltage, DC-Link voltage and limits, rotor current magnitude and limits, d-q stator flux for DFIG under normal operation.

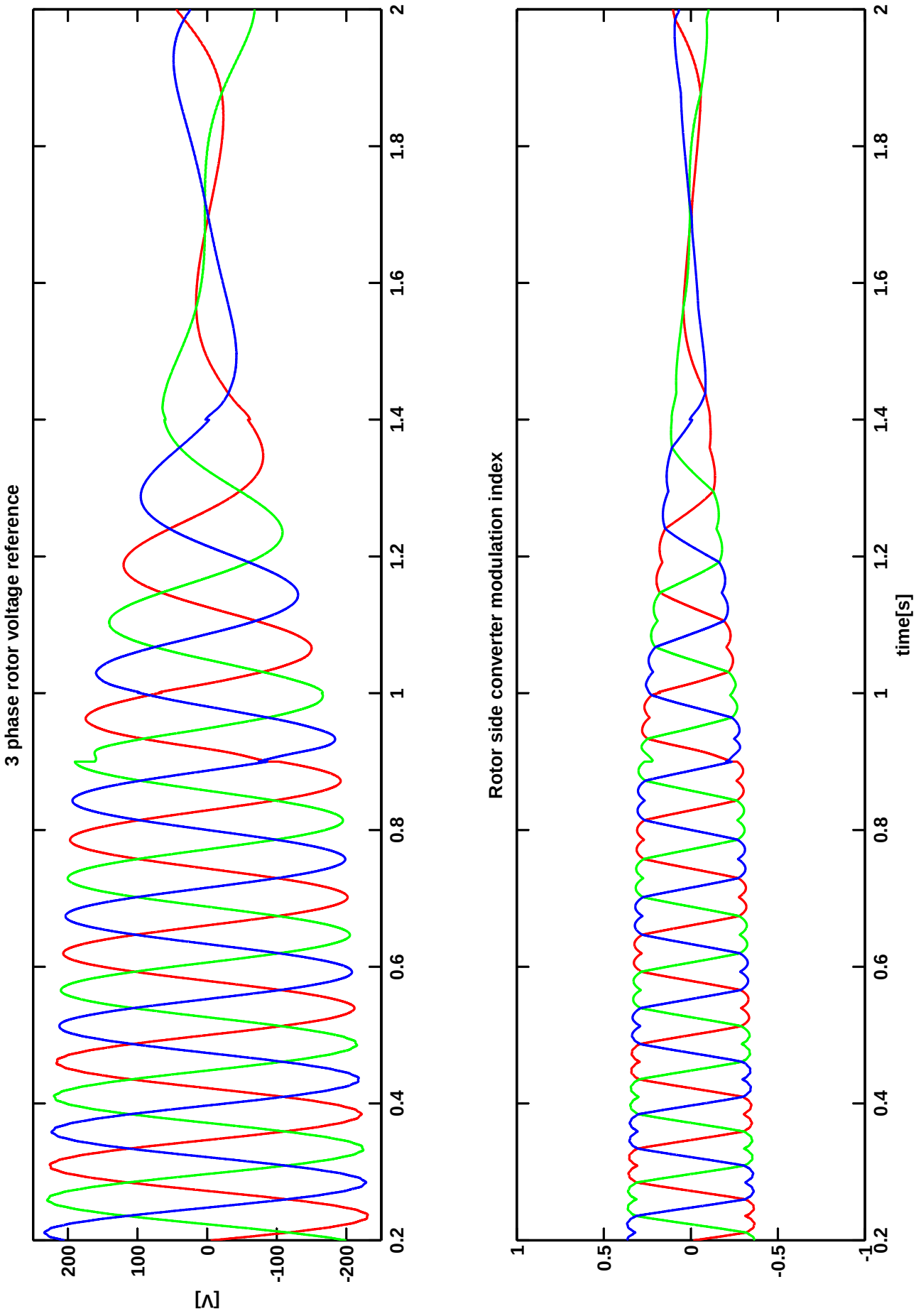


Figure F.3: 3 phase rotor voltage reference, rotor side converter modulation index for DFIG under normal operation.

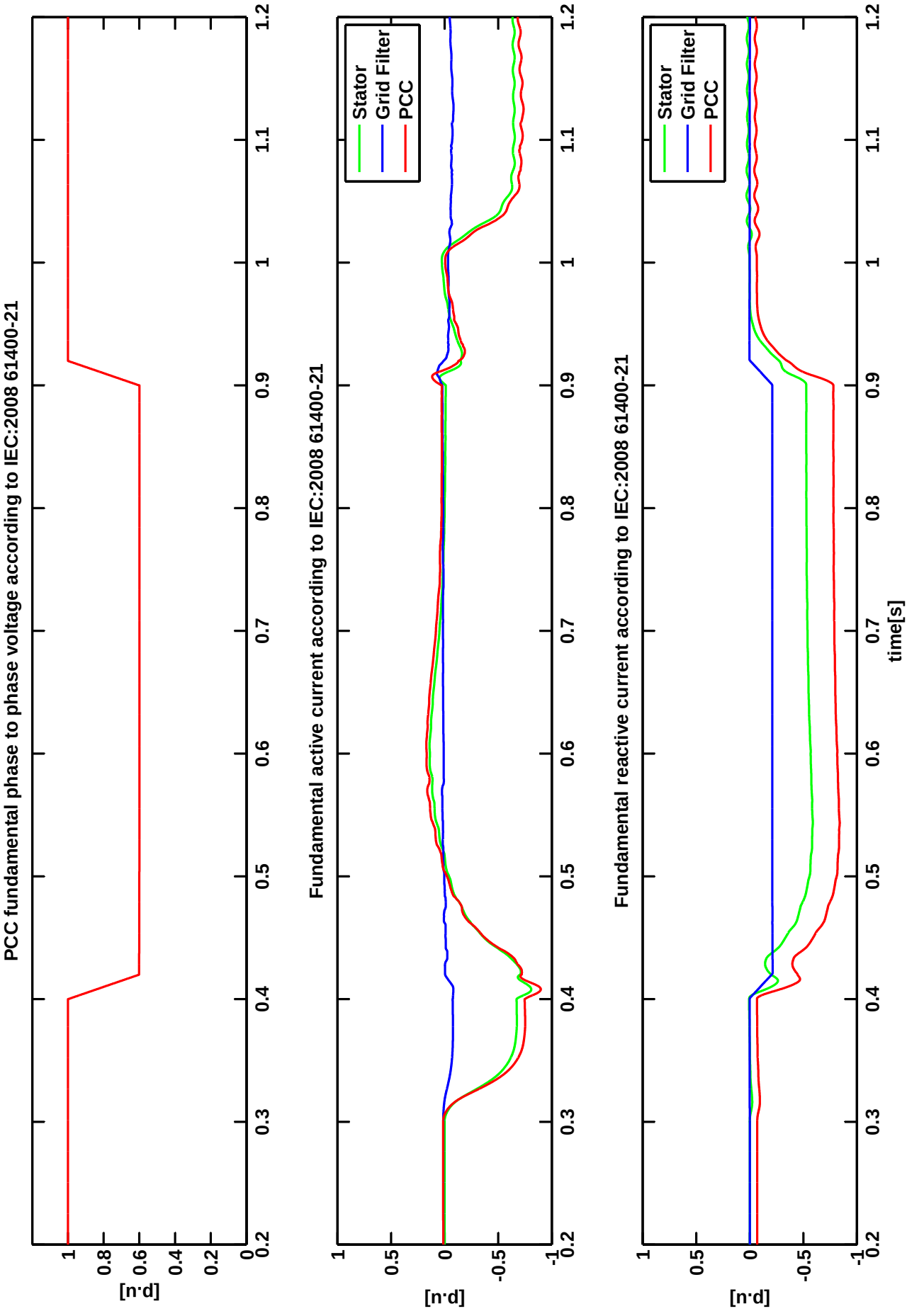


Figure F.4: Fundamental quantities according to IEC:2008 61400-21 for DFIG experiencing a 40% voltage sag. Full disturbance compensation method.

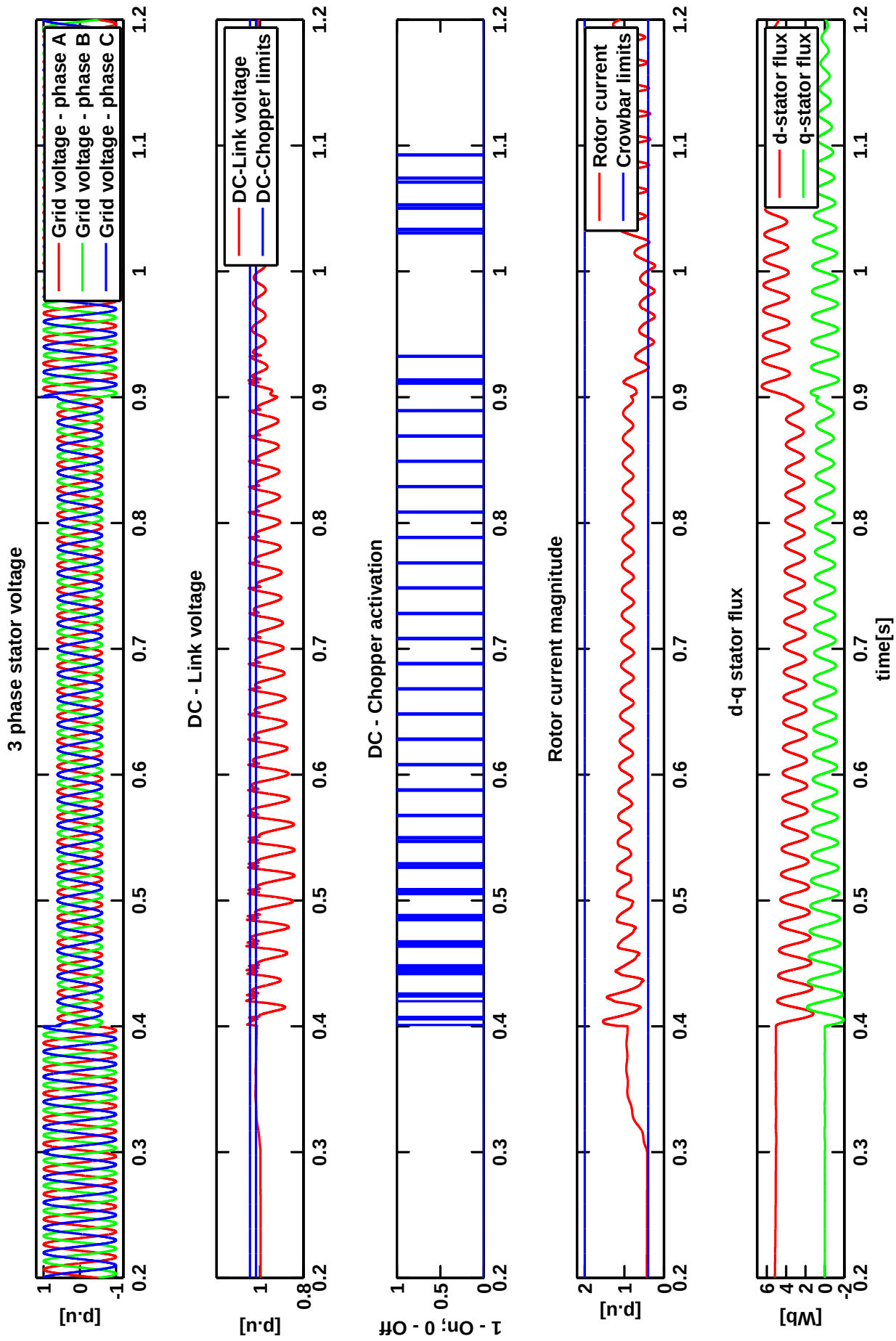


Figure F.5: Stator voltage, DC-Link voltage and limits, DC-Chopper activation, Rotor current magnitude and limits, d-q stator flux for DFIG experiencing a 40% voltage sag. Full disturbance compensation method.

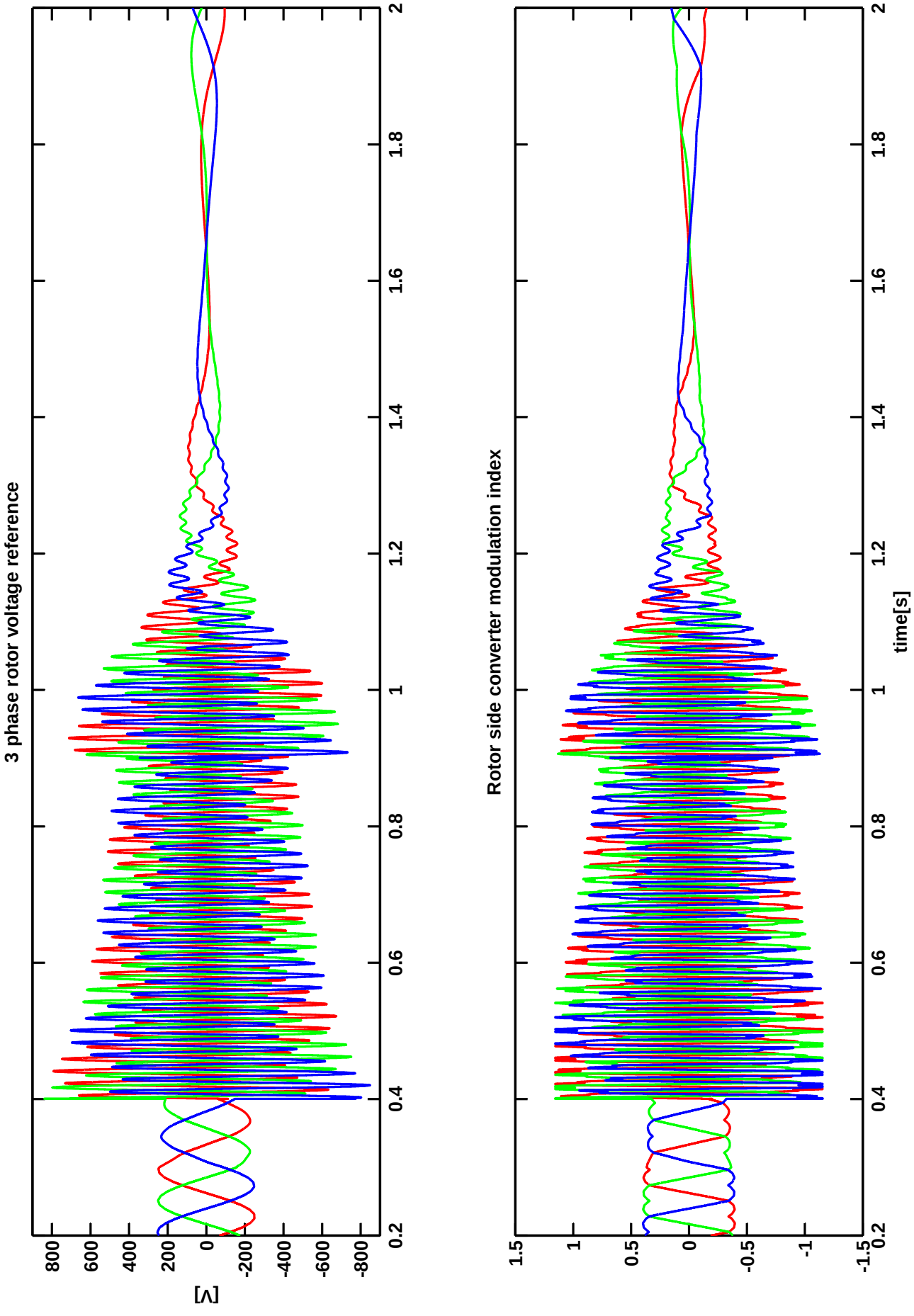


Figure F.6: 3 phase rotor voltage reference, rotor side converter modulation index for DFIG experiencing a 40% voltage sag. Full disturbance compensation method.

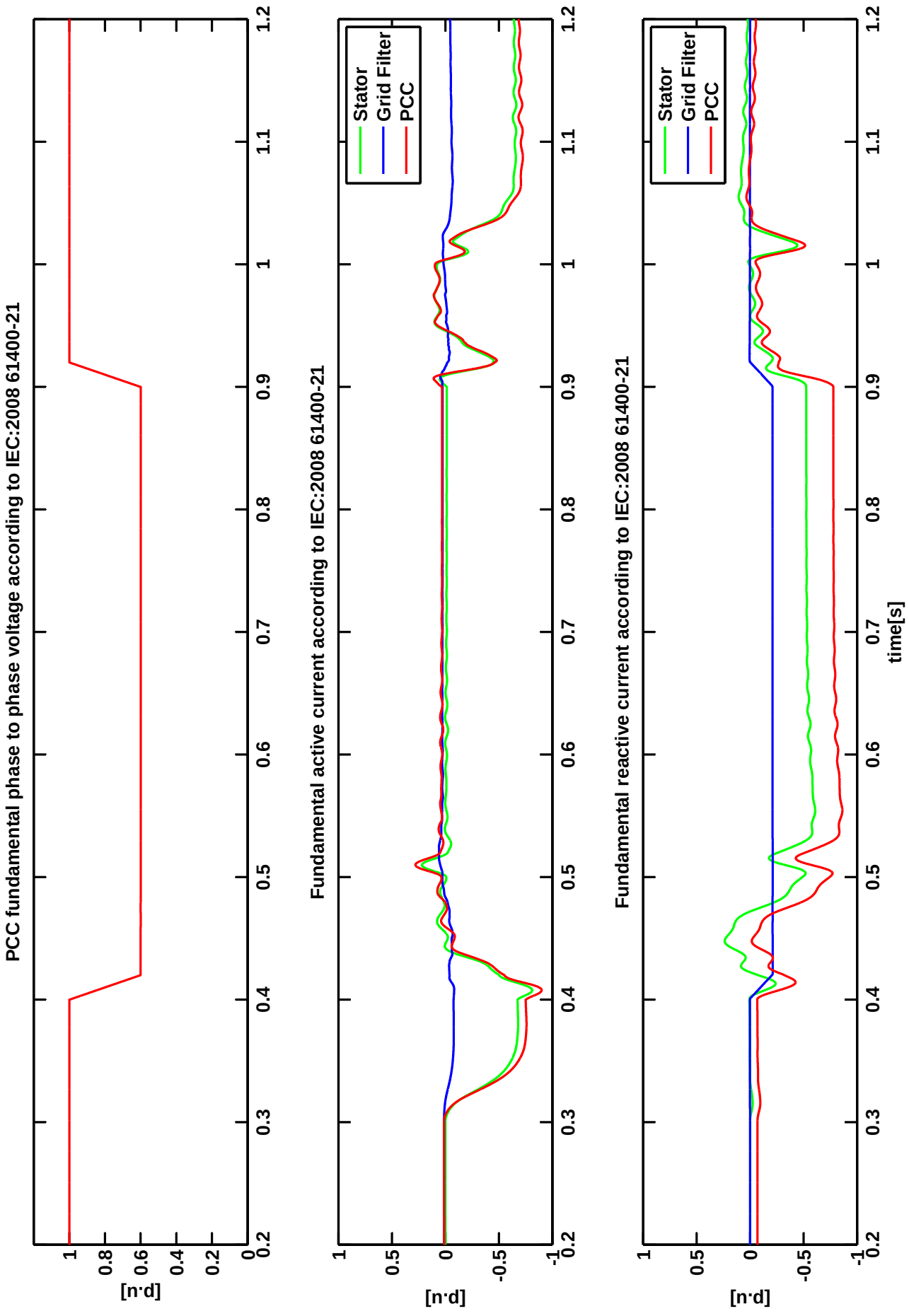


Figure F.7: Fundamental quantities according to IEC:2008 61400-21 for DFIG experiencing a 40% voltage sag. Partial disturbance compensation with improved flux damping method.

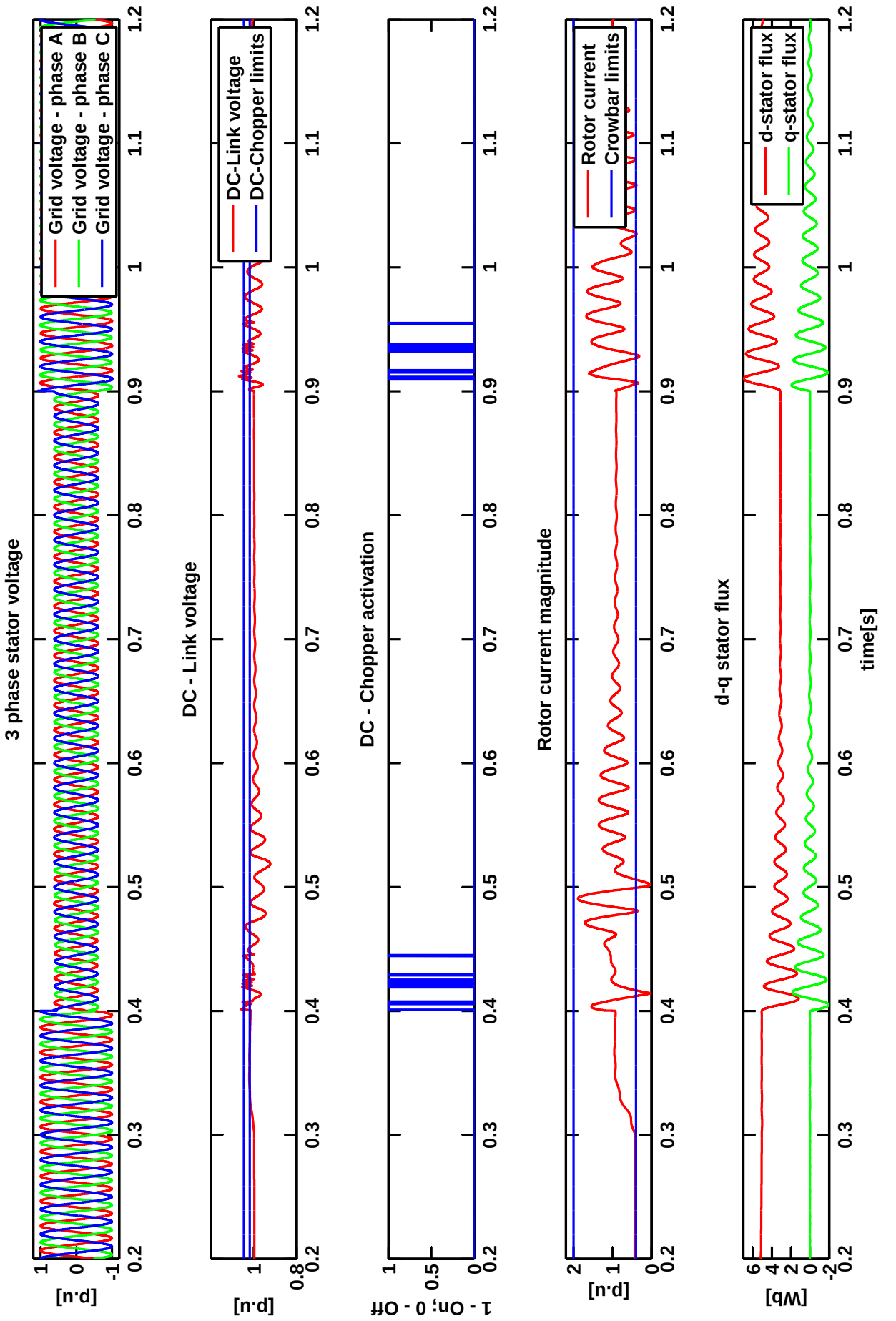


Figure F.8: Stator voltage, DC-Link Voltage and limits, DC-Chopper activation, Rotor current magnitude and limits, d-q stator flux for DFIG experiencing a 40% voltage sag. Partial disturbance compensation with improved flux damping method.

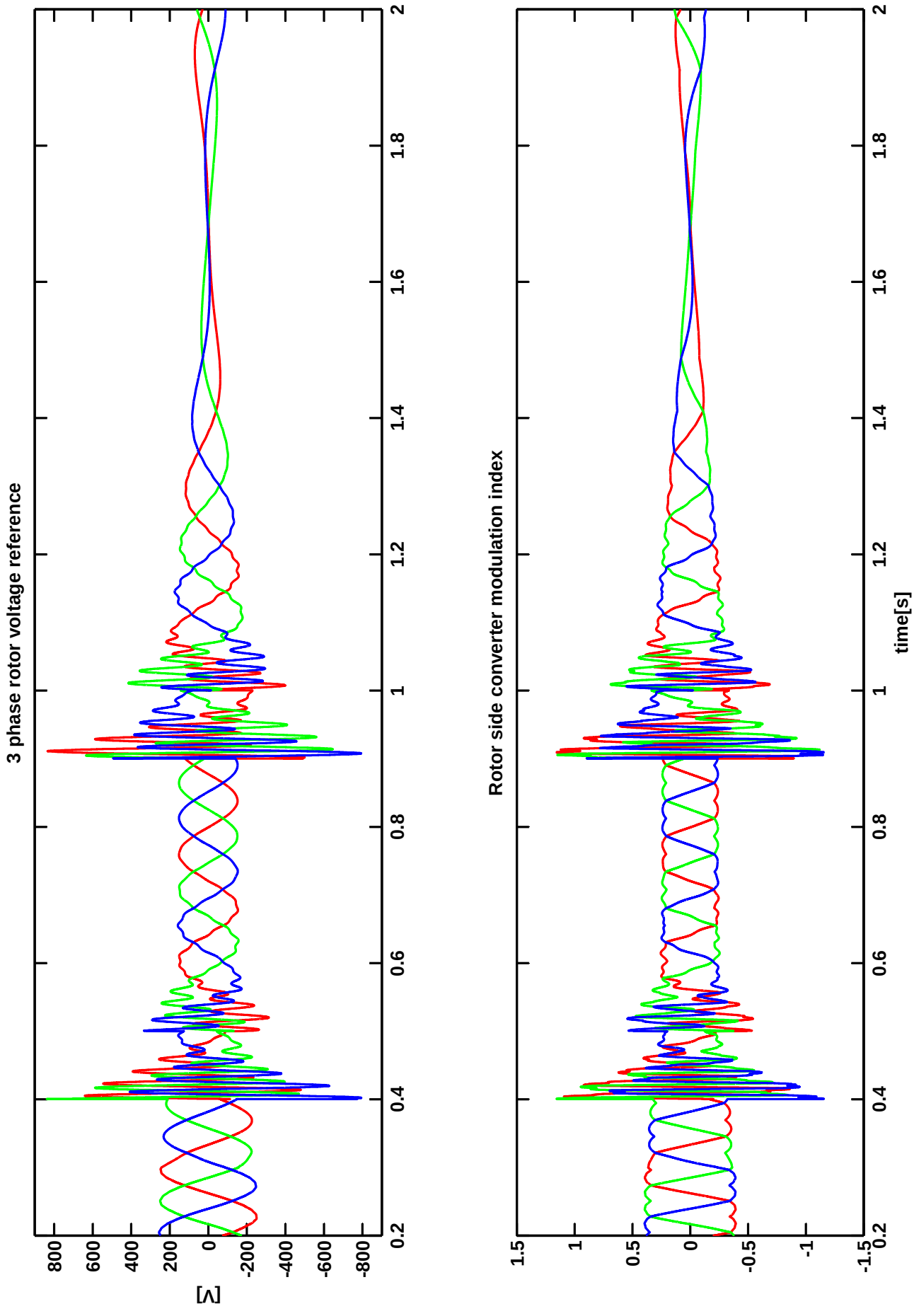


Figure F.9: 3 phase rotor voltage reference, rotor side converter modulation index for DFIG experiencing a 40% voltage sag. Partial disturbance compensation with improved flux damping method.

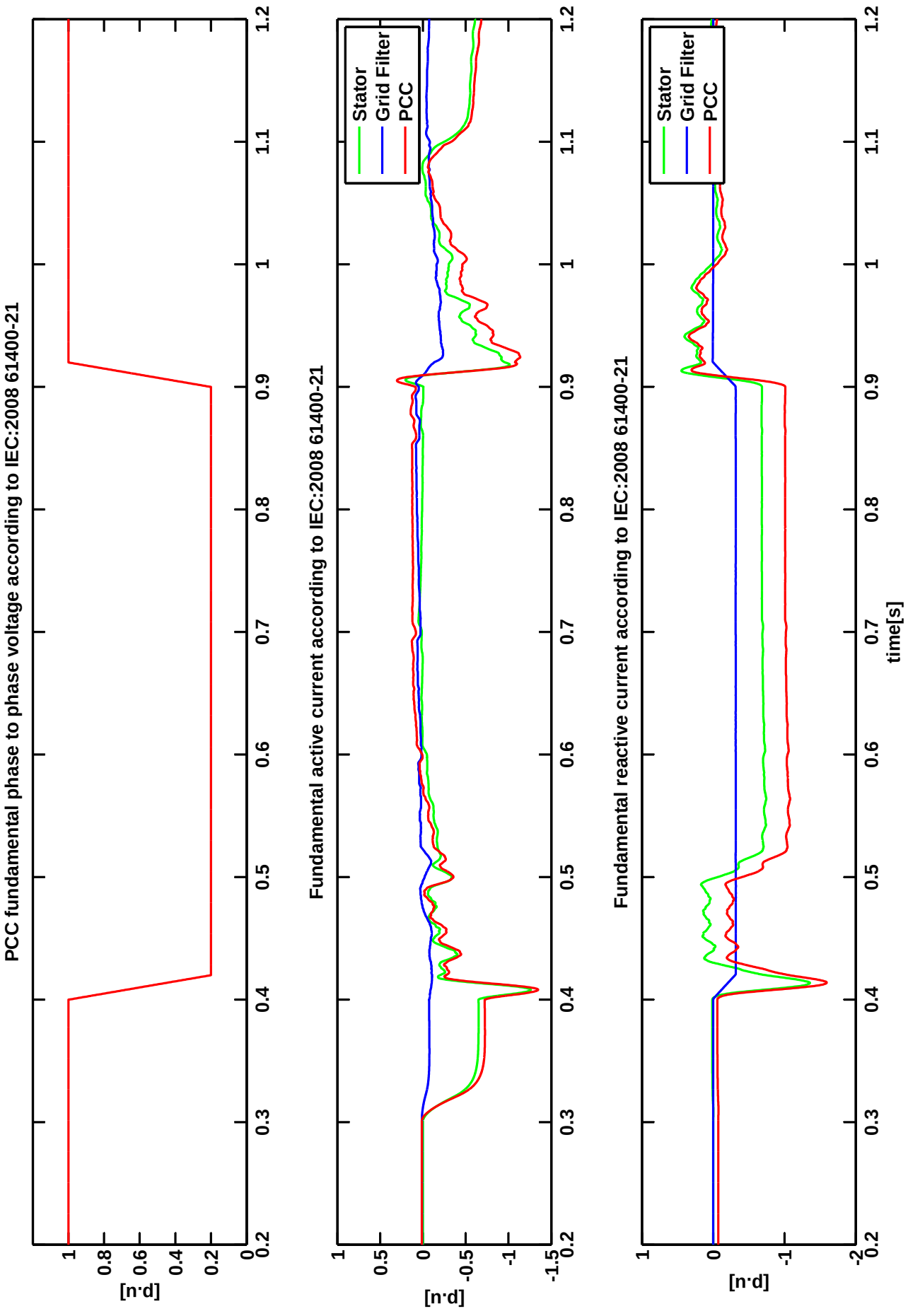


Figure F.10: Fundamental quantities according to IEC:2008 61400-21 for DFIG experiencing a 80% voltage sag. Rotor Crowbar. Full disturbance compensation method.

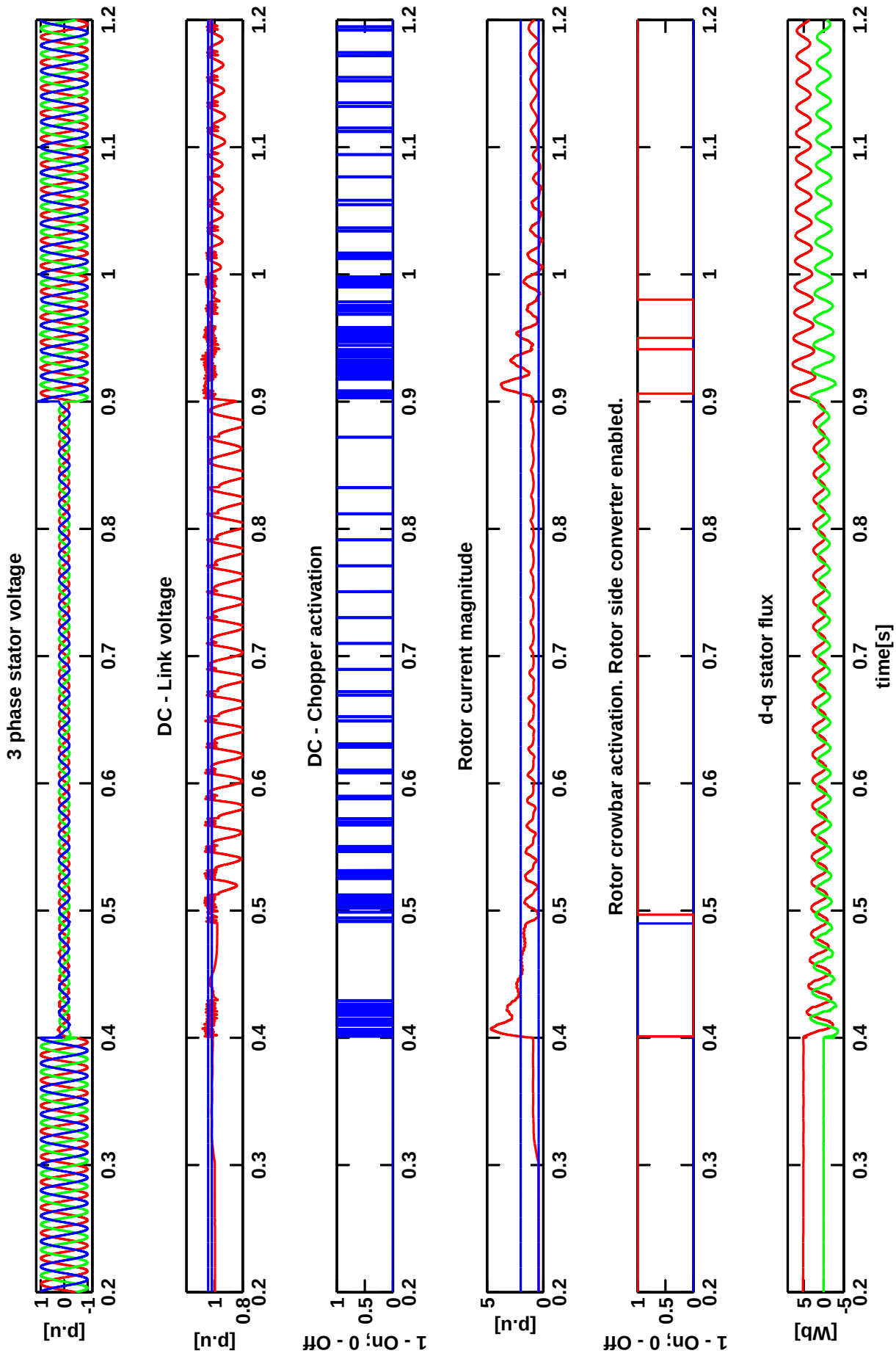


Figure F.11: Stator voltage, DC-Link voltage and limits, DC-Chopper activation, rotor current magnitude and limits, rotor crowbar activation, d-q stator flux for DFIG experiencing a 80% voltage sag. Rotor Crowbar. Full disturbance compensation method.

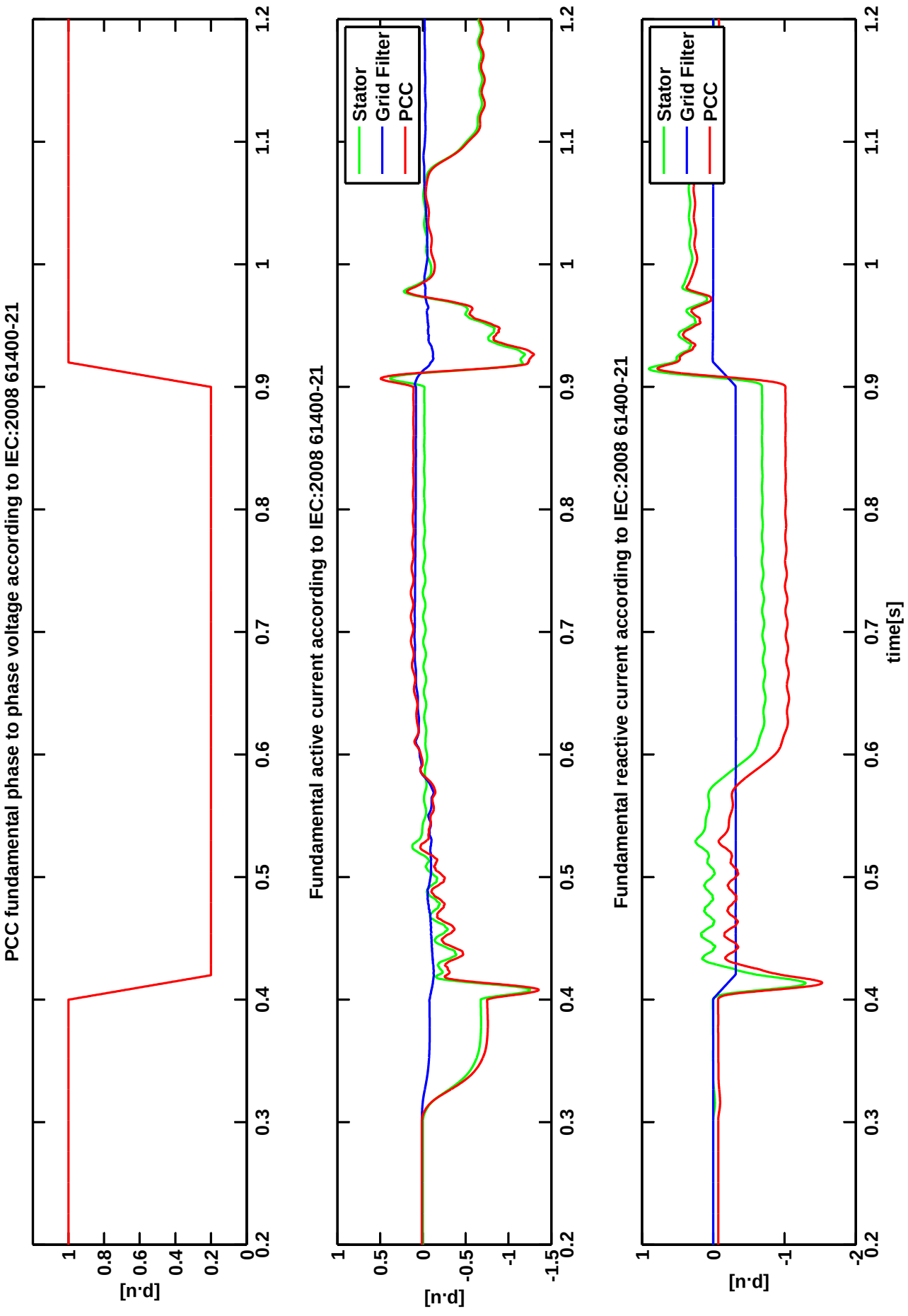


Figure F.12: Fundamental quantities according to IEC:2008 61400-21 for DFIG experiencing a 80% voltage sag. Rotor Crowbar. Partial disturbance compensation with improved flux damping method.

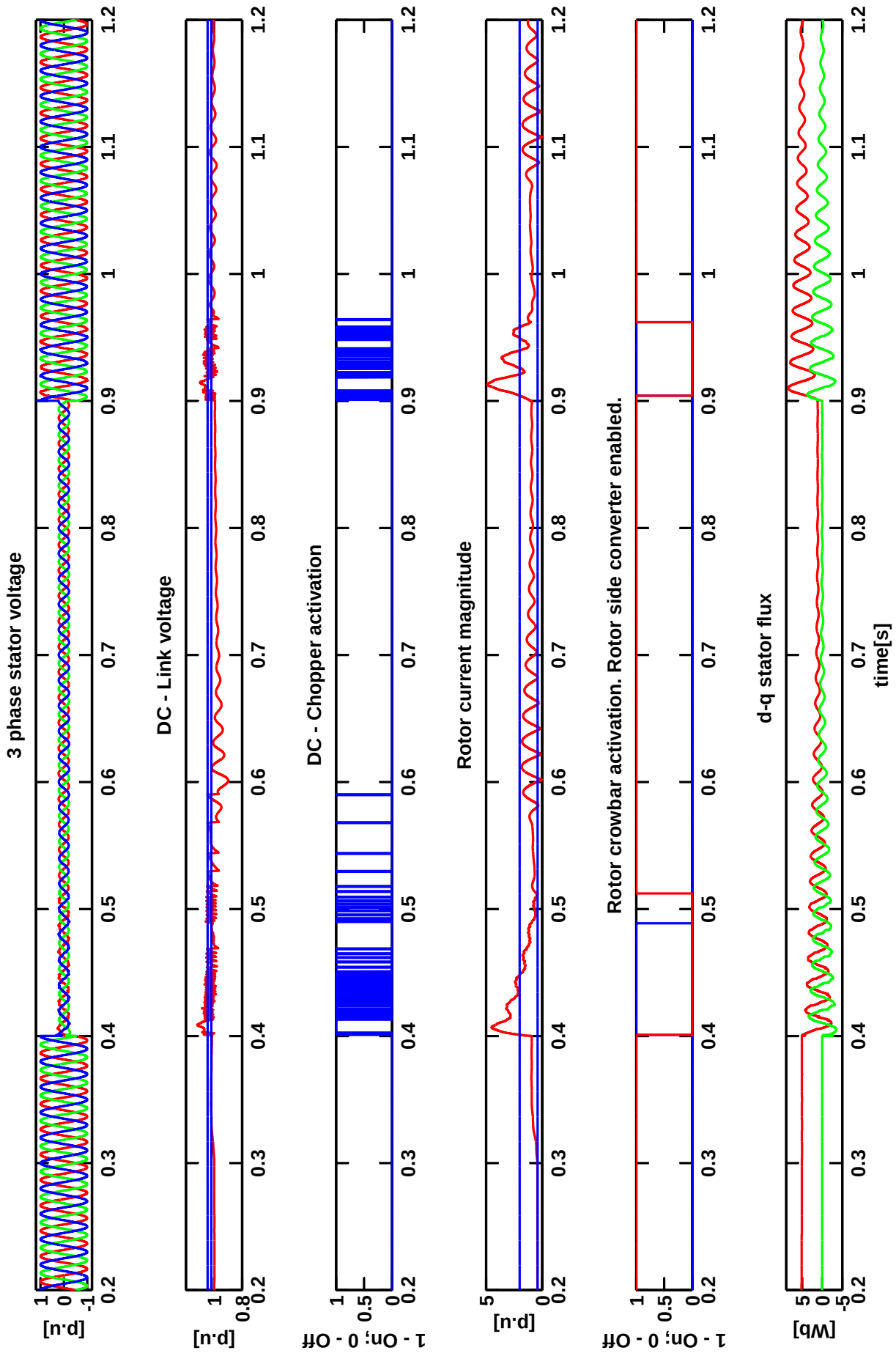


Figure F.13: Stator voltage, DC-Link voltage and limits, DC-Chopper activation, rotor current magnitude and limits, rotor crowbar activation, d-q stator flux for DFIG experiencing a 80% voltage sag. Rotor Crowbar. Partial disturbance compensation with improved flux damping method.

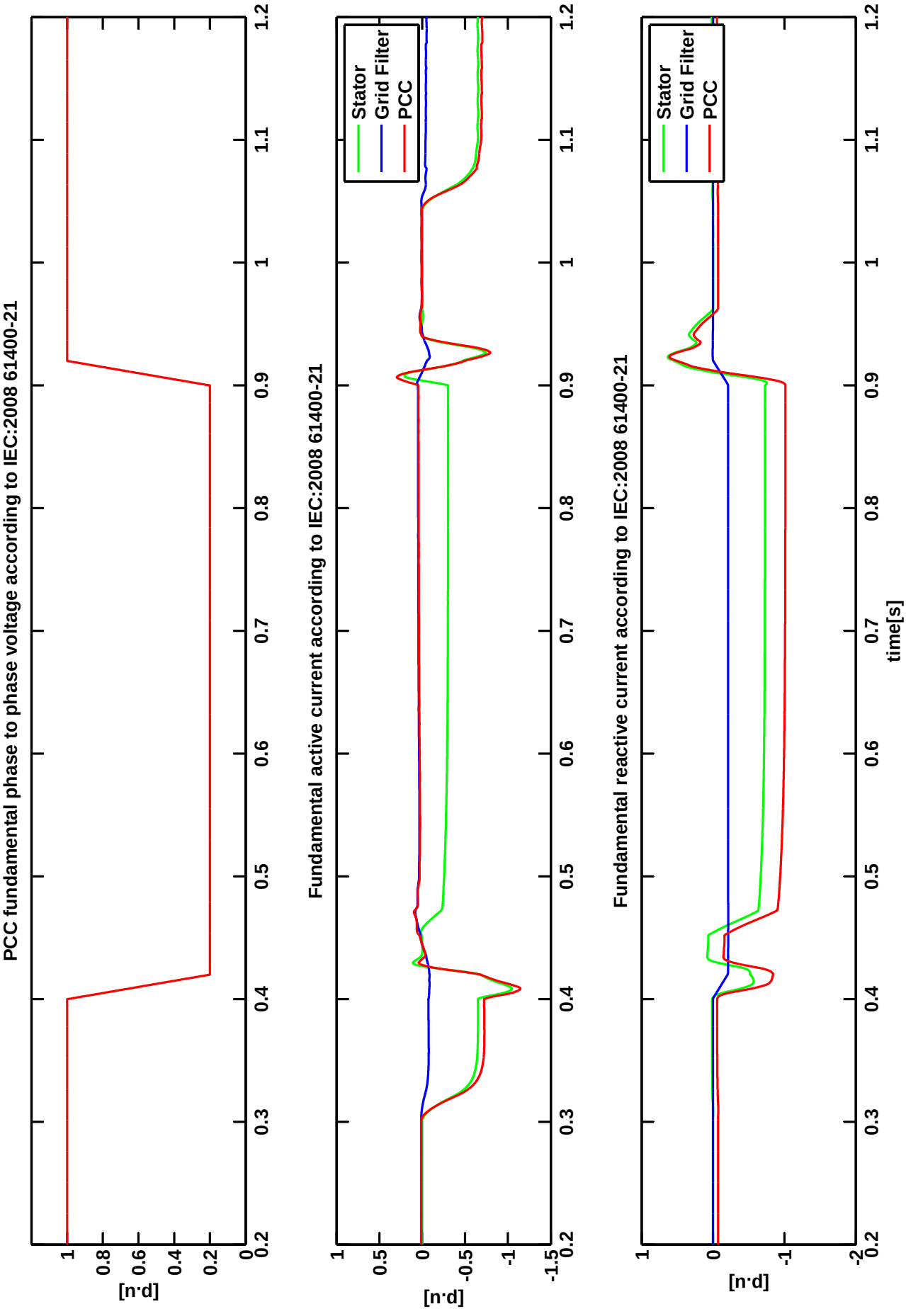


Figure F.14: Fundamental quantities according to IEC:2008 61400-21 for DFIG experiencing a 80% voltage sag. Stator Crowbar. Full disturbance compensation method.

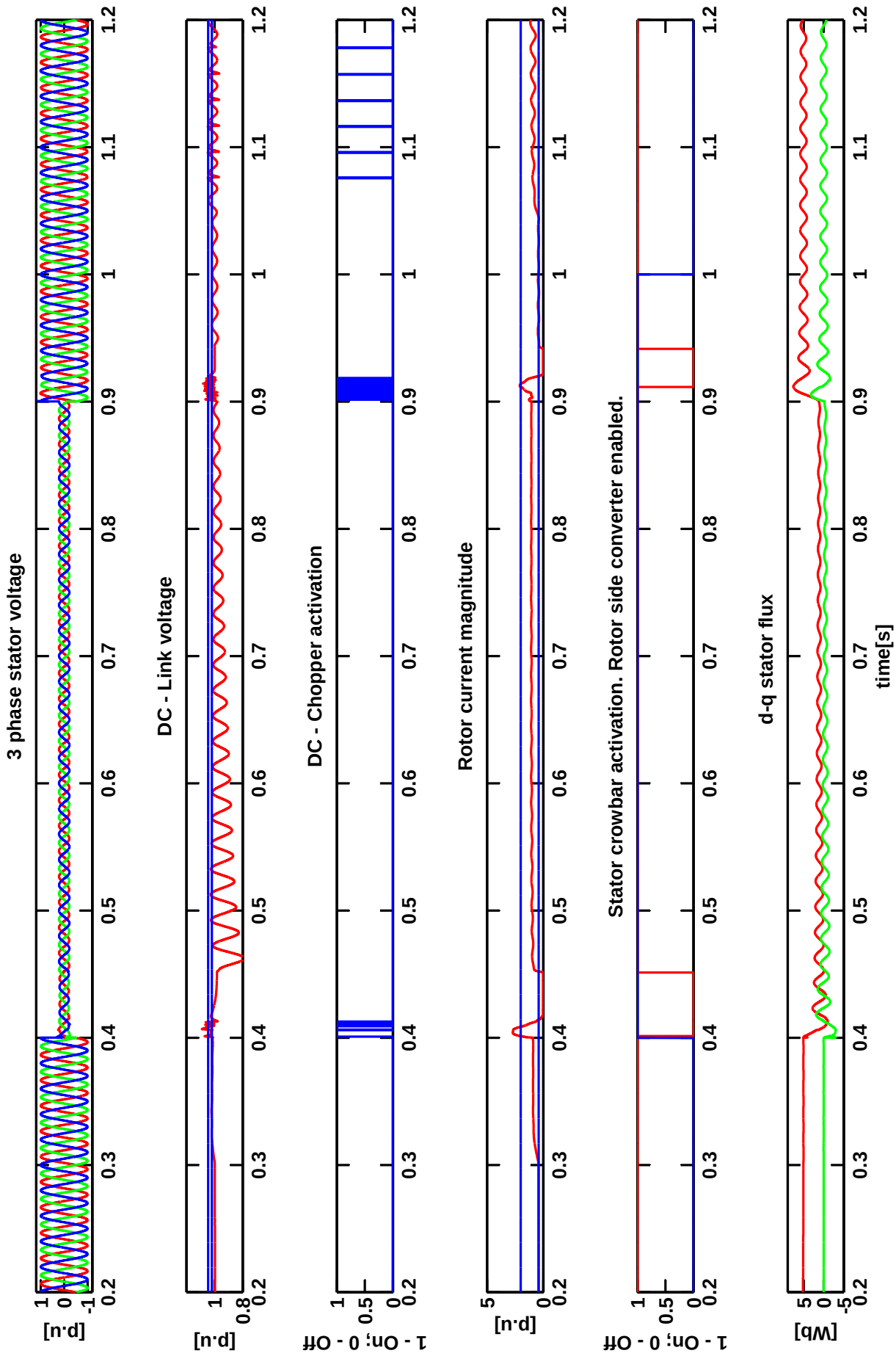


Figure F.15: Stator voltage, DC-Link voltage and limits, DC-Chopper activation, rotor current magnitude and limits, stator crowbar activation, d-q stator flux for DFIG experiencing a 80% voltage sag. Stator Crowbar. Full disturbance compensation method.

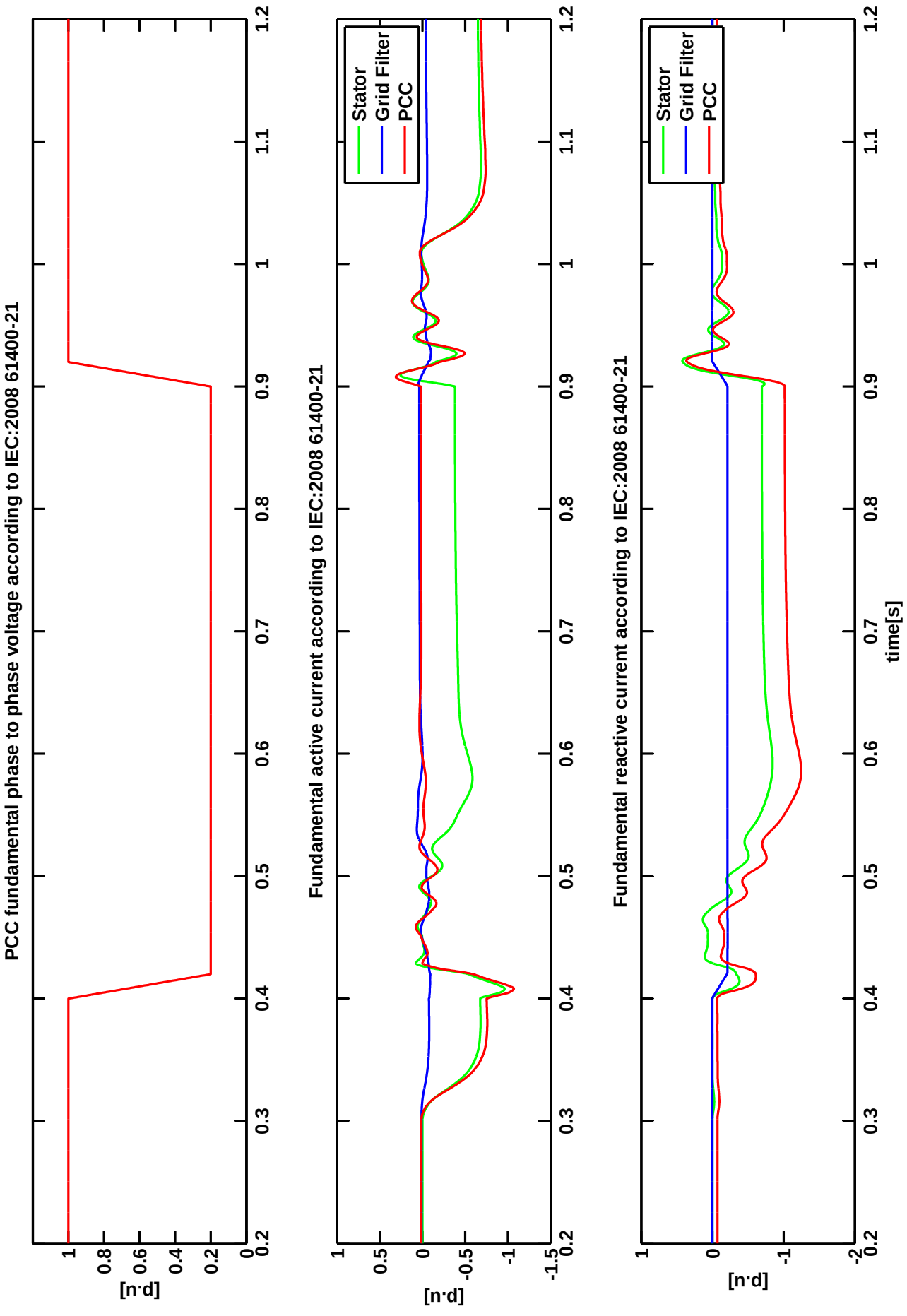


Figure F.16: Fundamental quantities according to IEC:2008 61400-21 for DFIG experiencing a 80% voltage sag. Stator Crowbar. Partial disturbance compensation with improved flux damping method.

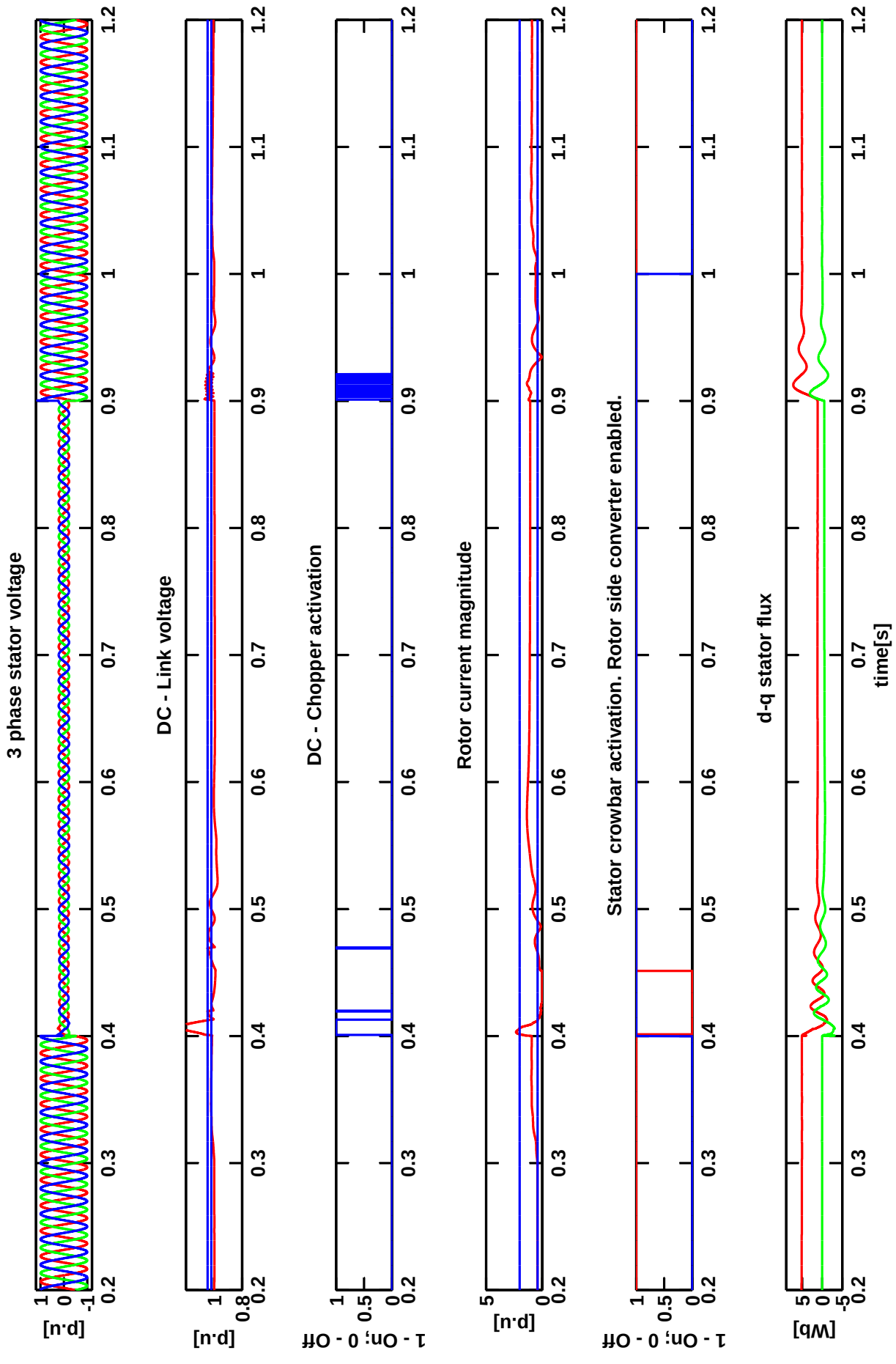


Figure F.17: Stator voltage, DC-Link Voltage and limits, DC-Chopper activation, Rotor current magnitude and limits, Stator crowbar activation, d-q stator flux for DFIG experiencing a 80% voltage sag. Stator Crowbar. Partial disturbance compensation with improved flux damping method.

## F.2 Experimental results

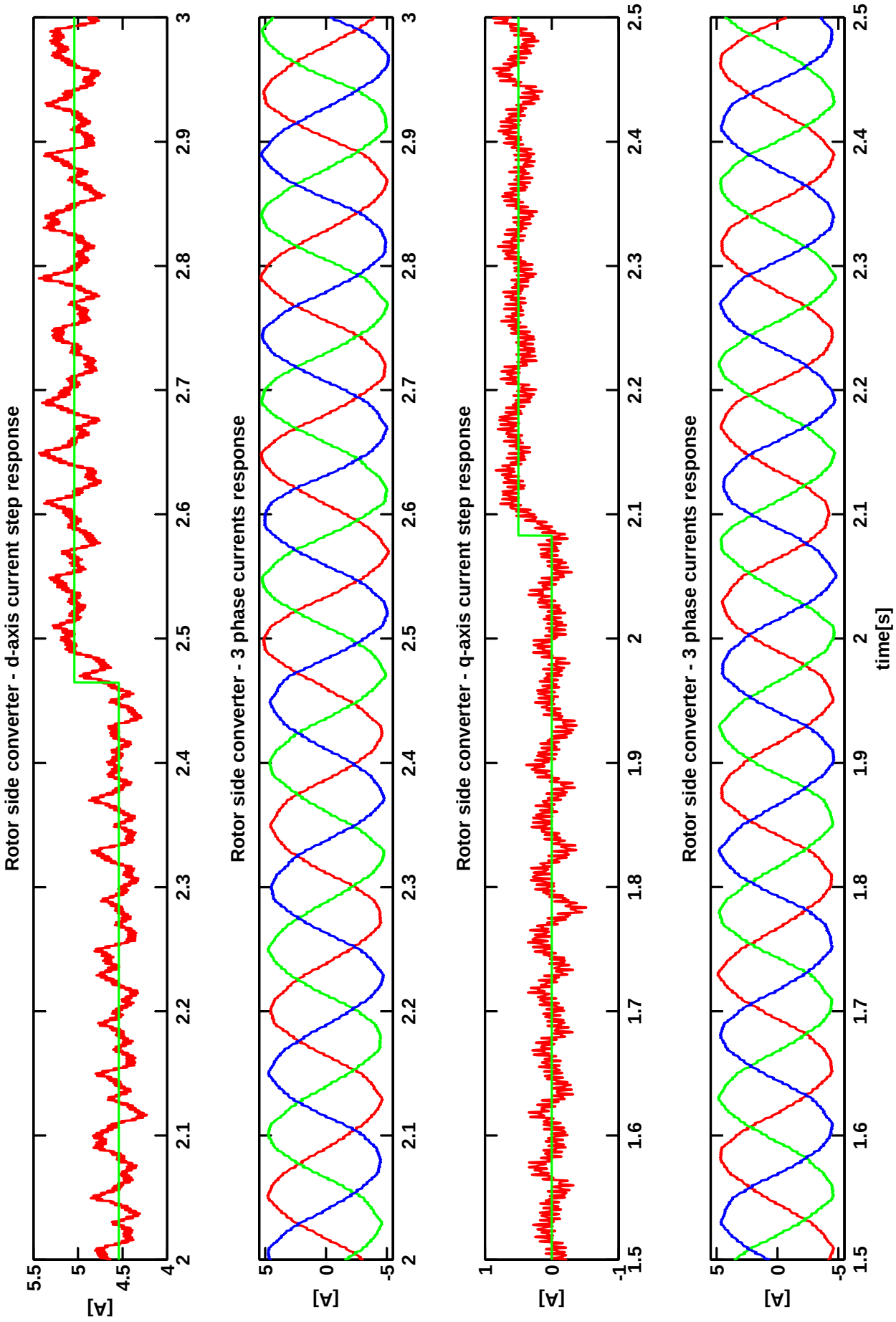


Figure F.18: Rotor side converter - current step response.

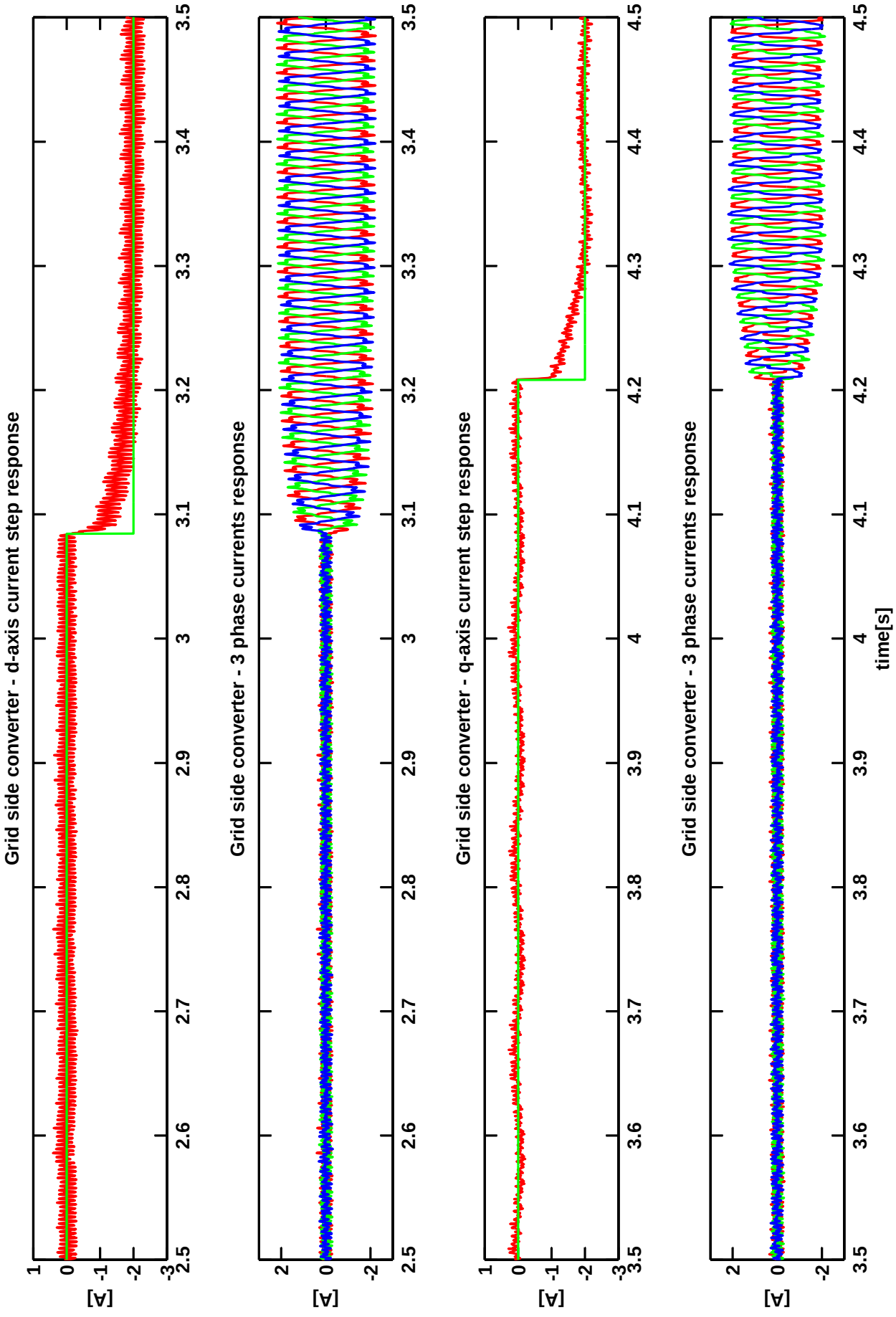


Figure F.19: Grid side converter - current step response.

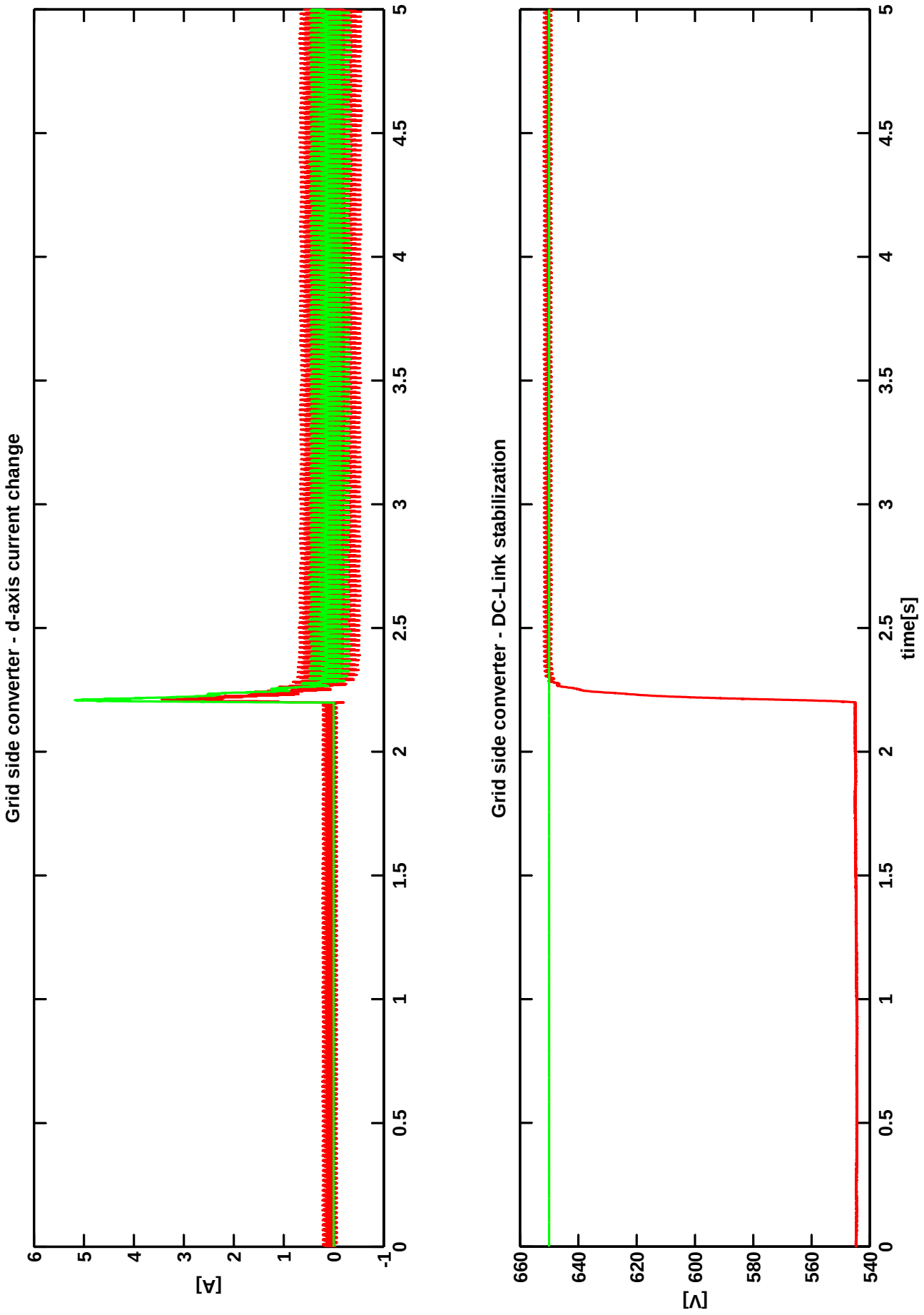


Figure F.20: Grid side converter - DC-Link stabilization.

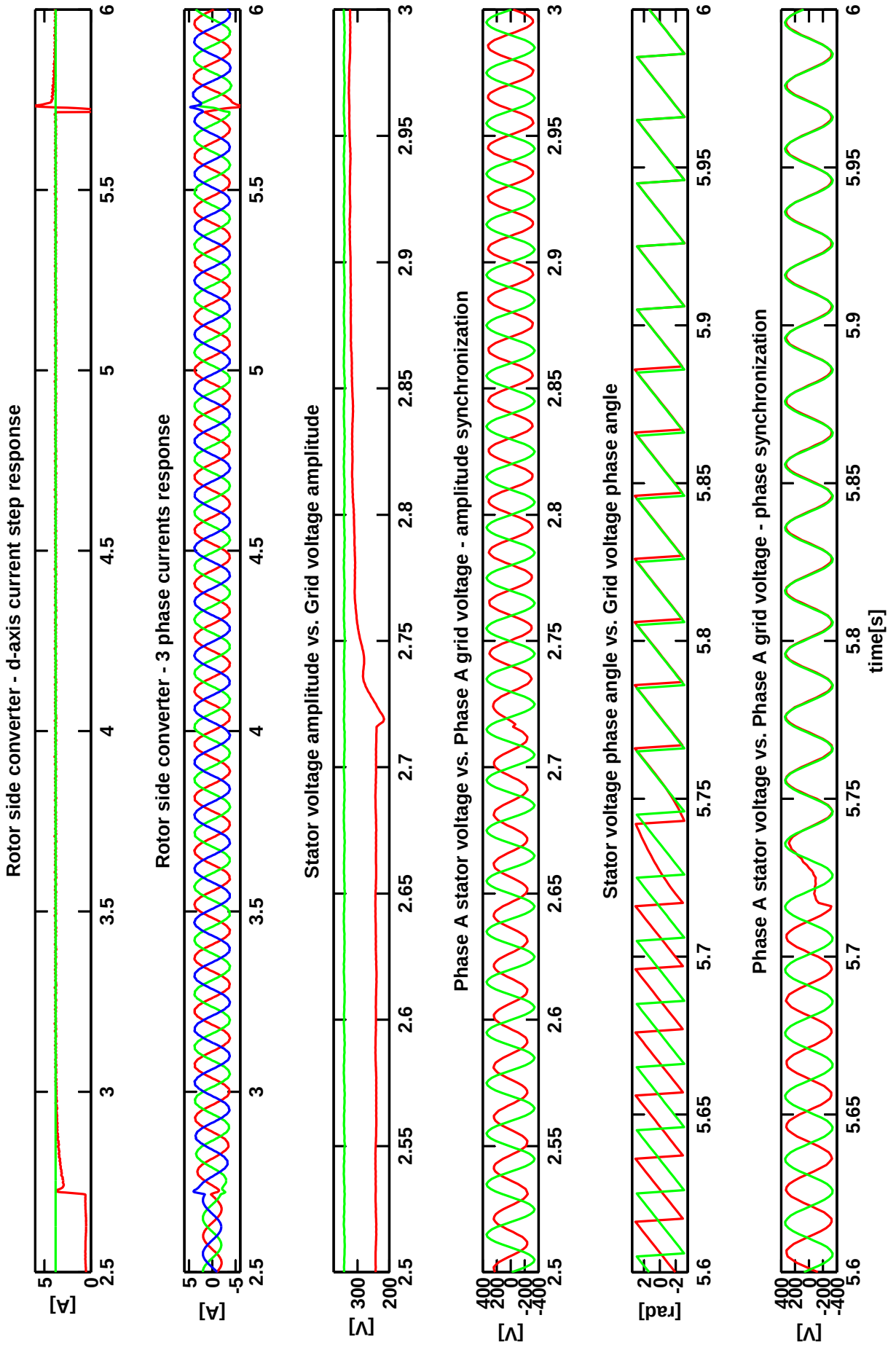


Figure F.21: *Synchronization* operating mode.

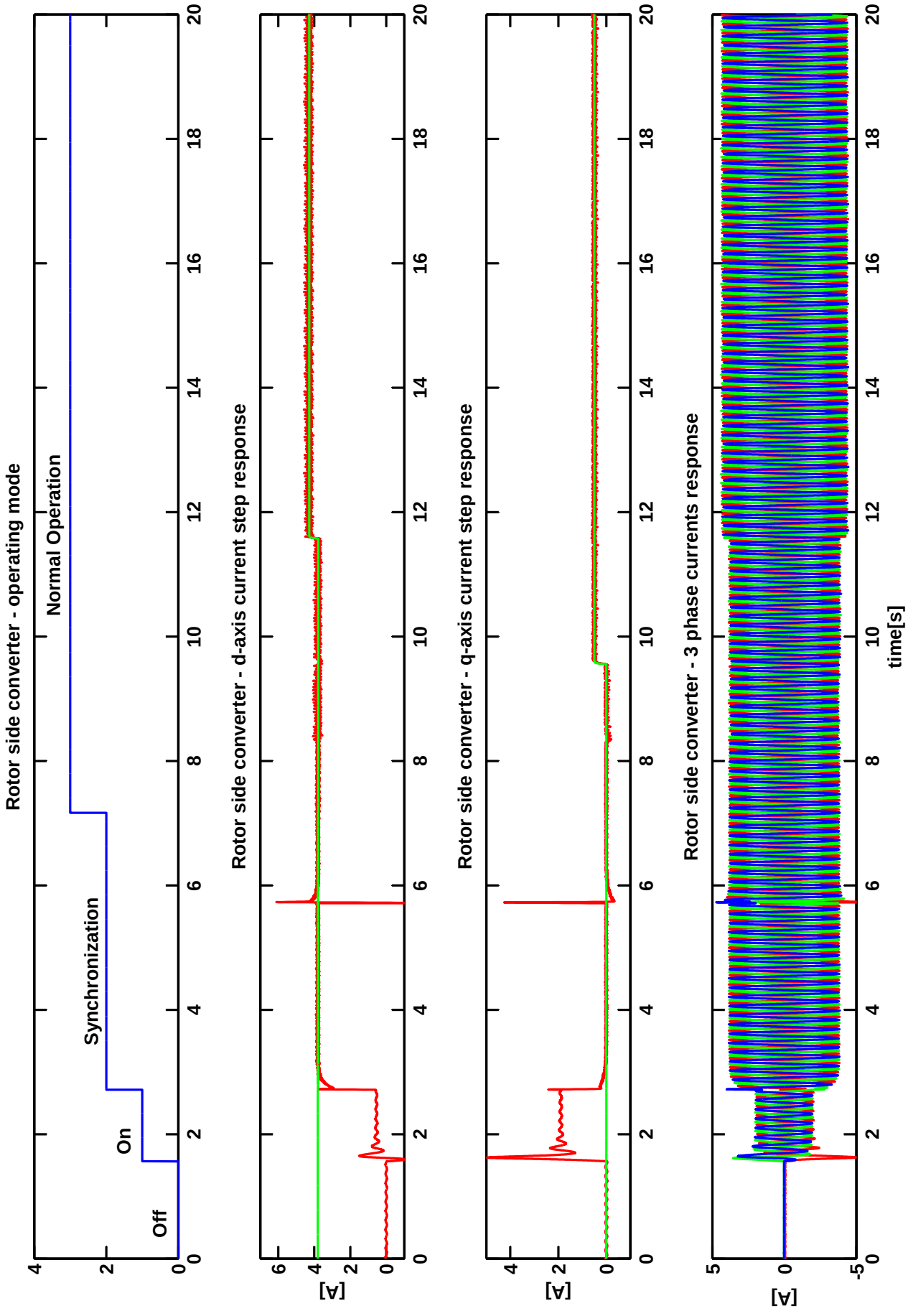


Figure F.22: *Synchronization* operating mode followed by *Normal Operation*.

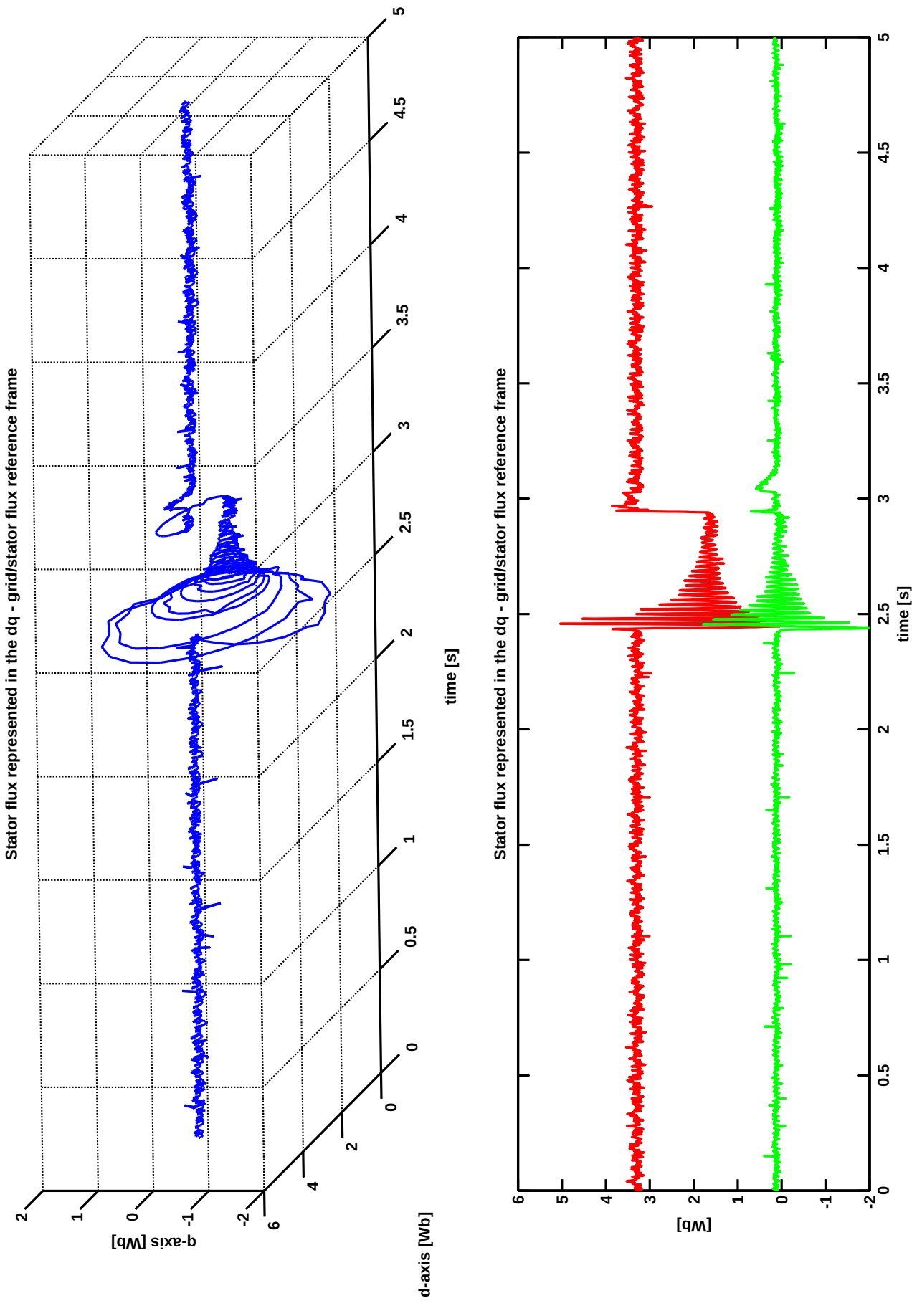


Figure F.23: Stator flux oscillation during a 25% grid voltage drop.

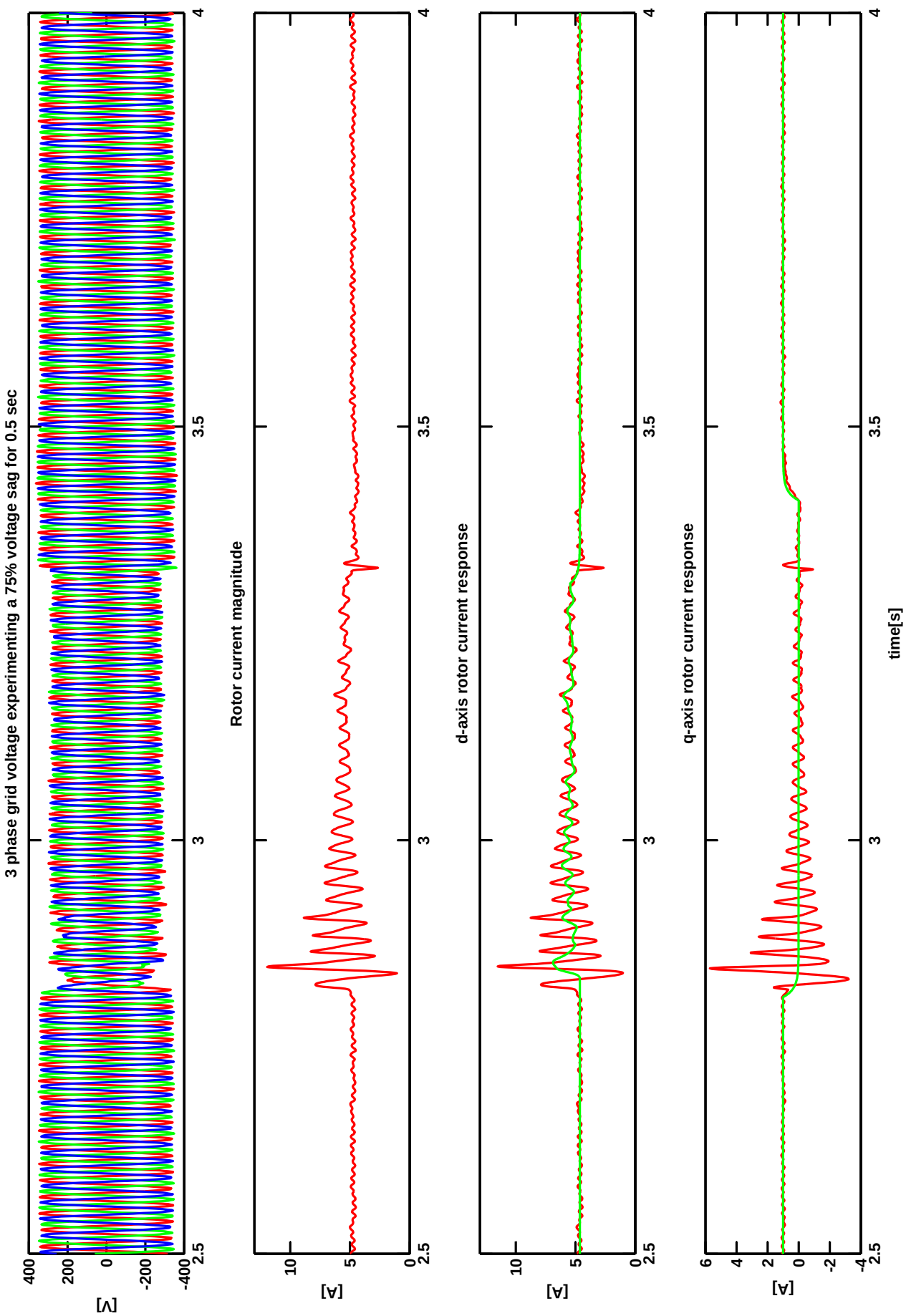


Figure F.24: Rotor side converter - current controller behavior during a 25% grid voltage drop.

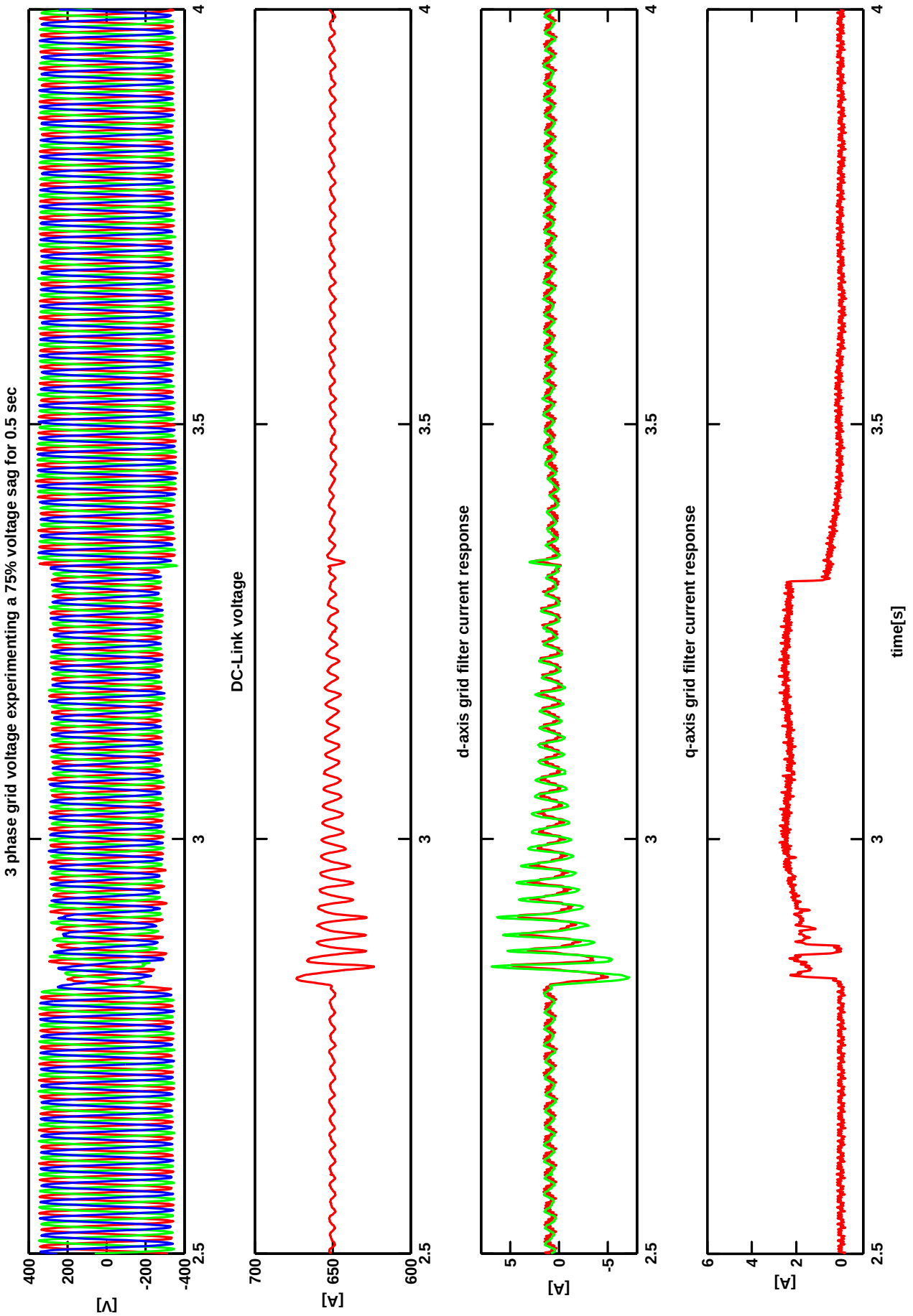


Figure F.25: Grid side converter - current controller behavior during a 25% grid voltage drop.